THERMAL INFRARED ANALYSIS OF VOLCANIC PROCESSES

by

Kevin Andrew Reath

B.S. Geology, University of Pittsburgh, 2006

M.S. Volcanology, University of Pittsburgh, 2011

Submitted to the Graduate Faculty of the

Kenneth P. Dietrich School of Arts and Sciences in partial fulfilment

of the requirements for the degree of

Doctor of Philosophy

University of Pittsburgh

2016

UNIVERSITY OF PITTSBURGH

KENNETH P. DEITRICH SCHOOL OF ARTS AND SCIENCES

This dissertation was presented

by

Kevin Andrew Reath

It was defended on

November 23, 2015

and approved by

Michael S. Ramsey (Primary Advisor), Professor, University of Pittsburgh

Robert Wright, Associate Researcher, University of Hawaii at Manoa (External Examiner)

Mark Abbott, Professor, University of Pittsburgh

Nadine McQuarrie, Associate Professor, University of Pittsburgh

Brian Stewart, Associate Professor

THERMAL INFRARED ANALYSIS OF VOLCANIC PROCESSES

Kevin Andrew Reath, PhD

University of Pittsburgh, 2016

Due to the dangerous and remote nature of many volcanoes, field-based data collection of active processes and precursory activity is problematic. Spaceborne remote sensing instruments enable these data to be recorded, monitored, and studied. The Advanced Spaceborne Thermal Emission and Reflection Radiometer (ASTER) is one such sensor that currently collects data in the visible near infrared (VNIR) and thermal infrared (TIR) wavelength regions and has an archive with the highest spatial resolution TIR data (90 m) currently available to the scientific community. ASTER is capable of recording precursory volcanic activity that is unidentifiable with other sensors. By combining ASTER data with those gathered from the Advanced Very High Resolution Radiometer (AVHRR) and the Moderate Resolution Imaging Spectroradiometer (MODIS), temporal resolution is improved and processes such as the cooling rate of pyroclastic flows and subtle precursory activity are able to be quantified. Rigorous modeling of these datasets further allows results such as estimation of pyroclastic flow volume, the specific eruption mechanisms and the onset of a future eruption. The work outlined in this dissertation demonstrates how data collected from the ASTER sensor greatly improves current monitoring capabilities. New methods for processing these high spatial resolution data allow scientists to understand and better evaluate the risks associated with specific volcanoes and their common eruption styles.

TABLE OF CONTENTS

LIST OF FIGURES

PREFACE

First, I would like to thank Michael Ramsey, for advising and supporting me for years in my undergraduate, masters, and now doctoral degrees and for giving the opportunity to challenge and better myself by working on this project. It's been a long road.

I would also like to thank:

The NASA Science of Terra and Aqua Research Program (NNX11AL29G) and the ASTER Science Team, who funded this research and experimental PhD program, without whom none of this work would have been possible.

My external adviser Robert Wright, for flying out from Hawaii on short notice to attend my defense, advising me at my time in Hawaii, and for always having ideas that push me to make my work better.

My committee members: Mark Abbott, Nadine McQuarrie, and Brian Stewart, who put their skill and time into helping me with my research.

My adviser at University of Bristol, Matt Watson, for bringing me to Guatemala and sending me to Sicily, and for helping me understand the fundamentals of SO_2 flux.

My adviser at University of Alaska Fairbanks, John Dehn, for getting me interested in volcanic precursors and for participating in my comprehensive exams and overview.

Vince Realmuto, for helping me to get the PlumeTracker program running and taking time out of his busy schedule for me to visit JPL to better understand the program.

Rainer Johnsen in the Department of Physics and Astronomy at the University of Pittsburgh, who helped me understand the physics associated with cooling rates.

My parents, Harvey and Evelyn, who had the daunting task of visiting me in Alaska, Hawaii, and England and were always available to help.

My sister and brother-in-law Shannon and Andrew Reichert, who provided me with a place to live and help me to not take life too seriously.

James Gardiner and Daniel Williams, who helped to edit portions of this dissertation and are always good friends.

Rob Rossi, who always has some way to take my mind off work, even when I'm trying to get work done.

All the friends I made in Alaska, Hawaii, and England, who added spice to life and made my travels worthwhile.

Finally, I'd like all the past and present member of the IVIS science lab: Christopher Hughes, Rachel Lee, Shelly Rose, Stephen Schiedt, Adam Carter, Alison Graettinger , Daniel Williams, Janine Krippner, and Christine Simurda. I can't imagine finishing the PhD program without the assistance I've received from each and every one of you.

1. INTRODUCTION

The Advanced Spaceborne Thermal Emission and Reflection Radiometer (ASTER) has been used as the primary instrument for many volcano-related studies since its launch in December 1999 (e.g. Wright et al., 1999; Ramsey and Fink, 1999; Ramsey and Dehn, 2004; Pieri and Abrams, 2004; Stevens et al., 2004; Carter et al, 2008; Huggel et al 2008). Generally, ASTER data have been used as a retrospective tool to analyze volcanic events because of its low temporal resolution and the long time initially required to process data (Yamaguchi, 1998). Instruments like the Advanced Very High Resolution Radiometer (AVHRR) and Moderate Resolution Imaging Spectroradiometer (MODIS) conversely have a much high temporal resolution and have been in the forefront of near real-time monitoring of volcanic eruptions (Dehn et al., 2000; Wright et al., 2004, Ramsey, 2015). With the development of the ASTER Urgent Request Protocol (URP) (Duda et al, 2009; Ramsey, 2015) in late 2006, the overall number of ASTER scenes and the time required to process those scenes greatly improved and the use of ASTER as a monitoring tool has become a possibility. Details related to eruption dynamics and precursory activity that are impossible to observe with the AVHRR and MODIS sensors can be analyzed with ASTER, due primarily to its greater radiometric accuracy and higher spatial resolution (Yamaguchi, 1998; Henney & Watson, 2006). One such example includes modeling of pyroclastic flow cooling rates in order to derive their volume, which can be compared to the dome growth rate (also measurable with ASTER) to estimate the probability of the next pyroclastic flow occurrence. Another example is using ASTER data to measure the thermal flux over time at a volcano during a pre-eruptive period. Changes in

the thermal flux can be indicative of both the approximate intensity of the next eruption as well and as the time until its onset. Finally, the thermal infrared (TIR) data are also sensitive to detect passive SO_2 emissions indicative of eruption potential. The strength of the 8.65µm (band 11) TIR absorption band can be compared to the surface spectra and then modeled with the PlumeTracker software to produce quantitative SO_2 degassing rates. These measurements are sensitive enough to detect SO_2 flux during the precursory period, which is not possible with other spaceborne instruments, thus providing a possible indicator of an upcoming eruption. By integrating the ASTER data into the existing volcano monitoring programs that rely on the low spatial/high temporal resolution data, the accuracy of forecasting the onset time and risks associated with eruptions greatly improve.

The first chapter of this dissertation uses TIR data to model the cooling rate of a recently-emplaced pyroclastic flow on Shiveluch Volcano, Russia. From this, an emplacement time is predicted, which corresponds to the seismic data. The results are then expanded to calculate the depth and volume of the flow, presenting two different stratigraphic models that fit the results. Finally, subtracting this volume (lost during the pyroclastic flow) from dome extrusion rates, an accurate growth rate of the lava dome is established. This allows a prediction of the next pyroclastic flow occurrence to be made.

The second chapter focuses on another Russian volcano (the 2005, 2007, and 2009 eruptions of Kluichevskoi) using TIR data to calculate the thermal flux during the precursory periods before each eruption. Analysis of these data revealed unique variations in thermal flux before both the 2007 and 2009 eruptions. These are interpreted to represent three distinct, yet similar, precursory phases. Finally, because these three phases are based on quantitative changes

in thermal flux, the classifications are proposed as improvements to the existing classifications used in volcanic monitoring networks, which are currently based on qualitative assessments.

Finally, the third chapter uses newly-developed software by V. Realmuto and the NASA Jet Propulsion Laboratory called PlumeTracker to model ASTER TIR data and estimate the flux of SO_2 during the precursory and eruptive phases of Mt. Etna (Italy), Kilauea (Hawaii), and Kluichevskoi. Whereas the limited temporal resolution of ASTER was a challenge, data acquired during precursory periods of Mt. Etna enabled SO_2 data to be directly compared results from the higher temporal/lower spatial resolution Ozone Monitoring Instrument (OMI) and the Ozone Mapping Profiler Suite (OMPS). These sensors captured data on the same day as ASTER and they form the core of the current SO_2 spaceborne monitoring network. ASTER data from June 2, 2015 produced a modeled SO_2 plume whereas both the OMI and OMPS showed little to no SO_2 emissions. This suggests that ASTER TIR data are more sensitive to small-scale/lower flux rate SO_2 emissions than either OMI or OMPS and therefore should be able to detect the subtle precursory variations in SO_2, which would be critical for monitoring. Additionally, ASTER-derived SO_2 concentration data from Kilauea were compared to ground measurements to determine the accuracy of PlumeTracker-derived SO_2 concentrations. This modeling analysis at three different volcanoes (two of which have well-established degassing rates) with different eruptive styles, different latitudes and different elevations allowed the sources of modeling error to be recognized and discussed. The results were finally compared to the thermal precursors described in the previous chapter as a way to use a well-established precursory indicator such as SO_2 flux to provide additional insight into the future eruptive potential.

2. SYNERGISTIC USE OF HIGH AND LOW SPATIAL RESOLUTION SATELLITE DATA TO DETERMINE PYROCLASTIC FLOW COOLING RATES

Reath, K.A.[1], Wright, R.[2], Ramsey, M.S.[1]

[1] Department of Geology and Planetary Science, University of Pittsburgh, 4107 O'Hara Street, Pittsburgh, PA 15260

[2] Hawaii Institute of Geophysics and Planetology, University of Hawaii at Manoa, 1680 East-West Rd., Honolulu, HI 96822

2.1. Introduction

Pyroclastic flows are a high velocity, devastating, and common hazard associated with many lava dome forming composite volcanoes such as Unzen Volcano in Japan (Nakada and Fujii, 1993), Merapi Volcano in Indonesia (Schwarzkopf et al., 2005), Colima Volcano in Mexico (Saucedo et al., 2004) and Soufriere Hills Volcano on the island of Montserrat (Sparks and Young, 2002), as well as volcanoes with large column-producing explosive eruptions such as Vesuvius Volcano in Italy (Todesco et al., 2002). This hazard can occur as a result of column collapse during an eruption (Sparks et al., 1978; Fisher, 1979; Clarke, 2002) or as a result of gravitational collapse (Voight and Sousa, 1994; Belousov, 1995; Cole et al., 1998; Harris et al., 2002) and explosive disruption of lava domes (Belousov et al., 1999; Calder et al., 1999; Calder et al., 2002). The unpredictability of these pyroclastic flows makes them dangerous and impractical to study in situ during an ongoing eruption. However, waiting until a volcano has become inactive means many of these flows will become buried or modified. Observing and analyzing flows using remote

sensing negates the danger and can provide information soon after emplacement and before later modification or burial. This study is designed to use TIR orbital remote sensing to calculate the flow cooling rate and derive relevant quantitative information on the timing and volume of pyroclastic flows. This approach also allows the dome growth rate to be estimated, and therefore enables the possibility of predicting the likelihood of another collapse-related pyroclastic flow.

2.1.1. Remote Sensing Data

This study uses thermal infrared (TIR) remote sensing data from two sensors: the Advanced Spaceborne Thermal Emission and Reflection Radiometer (ASTER) and the Advanced Very High Resolution Radiometer (AVHRR) to analyze and model pyroclastic flows. The ASTER sensor was launched as one of the five instruments on the Terra satellite in December 1999 and first went into operation in early 2000. ASTER has 15m spatial resolution in the Visible Near Infrared (VNIR) and 90m spatial resolution in the TIR region. With a 60km swath width, ASTER's temporal resolution is limited to 1-7 days at the poles and 16 days at the equator (Yamaguchi et al., 1998; Ramsey and Dehn, 2004). ASTER is a scheduled system instrument, meaning all ground targets are scheduled on a daily basis. This schedule is created by individual user requests, global mapping campaigns, and emergency requests for acquisitions (Yamaguchi et al., 1998). In late 2006 the ASTER Urgent Request Protocol (URP) was implemented, which allows automated scheduling of specific volcanoes (Duda et al., 2009; Ramsey, 2015). Whereas the URP system does not provide real-time data, it does greatly improve the ASTER scheduling/acquisition/processing pathway, thus providing ASTER data as quickly as 1-3 days from scheduling (Carter et al., 2008;

Ramsey, 2015). The AVHRR instruments have a TIR spatial resolution of 1 km (IGBP, 1992) and are currently flown on National Oceanic and Atmospheric Administration (NOAA) satellites (Justice et al., 1985). The multiple AVHRR instruments provide a temporal resolution between 15 minutes to 4 hours and have a TIR spatial resolution of 1 km (IGBP, 1992). Combining both of these sensors allows for both high spatial (ASTER) and temporal (AVHRR) resolution data to be applied to the study of volcanic activity such as pyroclastic flow cooling rates and dome growth. Shiveluch volcano, Russia, was chosen as the subject of this study due to its activity state since 1999, which has produced multiple pyroclastic flows. Shiveluch is also at higher latitudes, ensuring that many data acquisitions are possible as a result of the overlap of adjacent imaging swaths approaching the poles, and hence, an increase in the number of cloud-free data are available.

2.1.2. Shiveluch Background

Shiveluch volcano is located at 56.65°N, 161.36°E on the Kamchatka peninsula of Russia and is the northernmost of the 29 potentially active volcanoes in the Kurile-Kamchatka arc. It is considered the one of the most active volcanoes in Kamchatka, averaging several eruptions per year (Fedotov and Maserenkov, 1991). The volcanic complex at Shiveluch is divided into the older, inactive edifice known as Stary Shiveluch (Old Shiveluch) and a younger, active edifice Molody Shiveluch (Young Shiveluch) which is adjacent to Old Shiveluch at a lower elevation (Ramsey et. al., 2012) (Figure 2-1A). Multiple basaltic andesite domes and lava flows make up the composition of Young Shiveluch (Dirksen et al., 2006; Carter and Ramsey, 2010). At least 60 large

explosive eruptions have occurred at this location in the past 10,000 years (Ponomareva et al., 1998); however, the current activity is dominated by the creation of basaltic andesite lava domes growing at a rate of 1.03×10^5 m^3/day to 6.40×10^5 m^3/day and block and ash flows resulting from the collapse of lava domes (Dirksen et al., 2006; Ramsey et al., 2012). This prevalence of flow emplacement makes Shiveluch an ideal natural laboratory for this study (Belousov, 1995; Ponomareva et al., 1998; Girishin, 2009; Carter and Ramsey, 2010; Girishin, 2012).

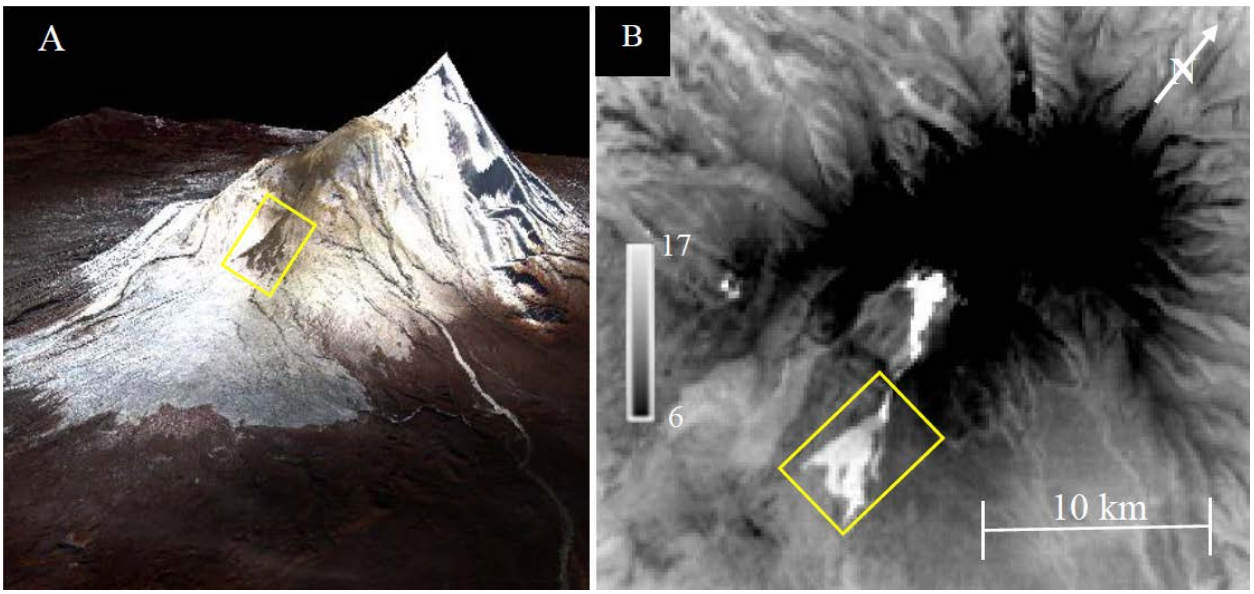

Figure 2-1:Shiveluch Volcano (A) highlighting the southern slope using an ASTER-derived DEM with a vertical exaggeration of 3 overlain by the ASTER VNIR data with band 3, 2, and 1 in RGB. The image was acquired on October 24, 2009 00:38 UTC. (B) ASTER TIR brightness temperature data in degrees Celsius acquired on July 30, 2009 10:50 UTC. Yellow boxes indicate black and ash flow of interest.

On April 25, 2009 an eruptive cycle began at Shiveluch, producing multiple pyroclastic flows including one on June 25-26 that remained exposed until September 11 when it was buried by a new flow (Smithsonian Global Volcanism Program, 2013). The June 25-26 pyroclastic flow (Figure 2-1) was the result of explosive activity that started on June 25, causing the lava dome at the summit to collapse. The Kamchatka Volcanic Emergency Response Team (KVERT) reported

seismic activity on June 25 from 11:04 to 13:06 UTC, which may be the result of the emplacement of this pyroclastic flow (KVERT, 2009). The satellite monitoring system of the Alaska Volcano Observatory (AVO) (e.g., Schnieder et al, 2000) showed a cloud-free image of the volcano acquired on June 25 at 10:18 UTC. Thermally elevated pixels are evident at the summit, but no pyroclastic flow is apparent. The thermal signature of this pyroclastic flow was first observed by the AVO monitoring system on June 25 at 14:56 UTC, supporting KVERT's analysis that the flow was emplaced sometime between 11:04 and 13:06 UTC on the June 25. This flow was deposited with a divide between the area of the upper and a lower flow units (Smithsonian Global Volcanism Program, 2009). This separation is caused by a flow constriction in an incised channel that directed the initial flow further downslope leaving the less energetic material higher up on the slope. This upper portion is continually heated by rock falls from the small, newly-growing dome. Therefore, we assume that the lower portion of the flow unit is thermally-isolated and for this reason this unit is the subject of this study.

2.1.3. Importance of Cooling Rates

Pyroclastic and block and ash flows are emplaced at temperatures higher than the surrounding ambient temperatures (e.g. Sparks et al., 1978; Voight and Sousa, 1994; Sparks and Young, 2002). With time, if left undisturbed, these flows will lose energy and naturally cool back to these ambient temperatures. In accordance with Newton's law of cooling, the time it takes for any material to cool can be directly related to its volume. In this case, the cooling rate of a flow is directly related to its volume (and depth). This cooling rate can be determined using satellite

sensors to track flow temperatures over time. From these data the amount of time needed for a flow to cool to ambient temperatures, as well as the manner in which it cools, are modeled and used to make volume estimates.

2.1.4. Balancing Dome Growth

High viscosity, degassed magma emplaced at a slow rate commonly forms a dome (Huppert et al., 1982). The dome will grow exogenously or endogenously with the continued discharge of lava from the conduit. At some point, the dome becomes too large and gravitationally unstable, causing a dome collapse which commonly results in a block and ash flow (Rodriguez-Elizarras et al., 1991; Cole et al., 2002). In order to calculate an accurate growth rate of a volcanic dome over a period of time, the volume of material lost to block and ash flows must be balanced against the volume of material gained during lava extrusion (Figure 2-2).

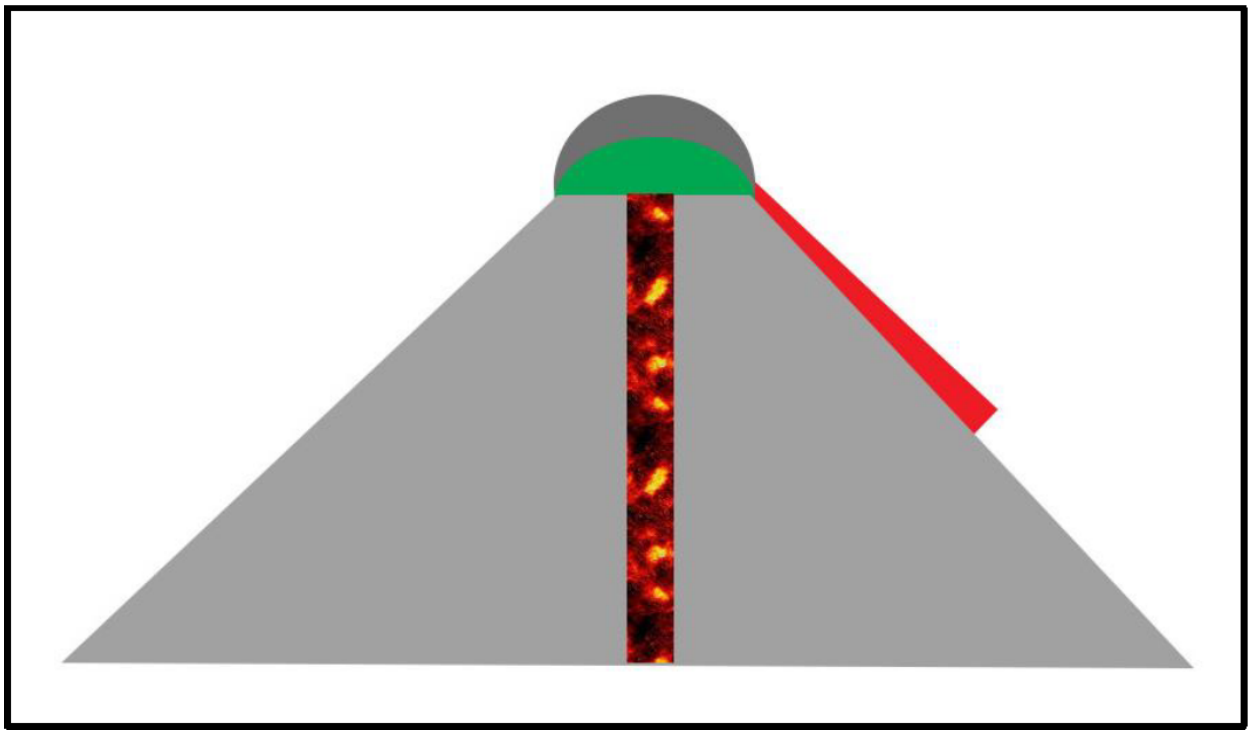

Figure 2-2: Schematic representation of lava dome growth. New material (green) extrudes from the crater adding to the volume of the existing dome (gray). When this growth leads to dome failure, a block and ash flow (red) is produced, removing material from the dome.

The extrusion rates of volcanic domes have been calculated by many methods including physical surveying, optical DEM generation from aerial photography, Interferometric Synthetic Aperture Radar (InSAR) data, as well as TIR satellite data (Sparks, 2003; Dzurisin et al., 2008; Piña-Gauthier et al., 2013; Vaughn et al, 2005; Schneider et al, 2008; Ramsey et al., 2012; Berstein et al, 2013). Surveying and aerial photography require close proximity to the volcano and InSAR data may not be possible at all volcanoes due to limited data availability and decorrelation of the data over the dome during the time period of dome growth. In these cases, TIR data is advantageous because these data have been acquired for all terrestrial dome-forming volcanoes with varying spatial and temporal resolutions. This allows the extrusion rates to be determined, particularly if data from multiple sensors are used together. However, in order to calculate the growth of a lava

dome both the extrusion rate and the total volume of material lost to pyroclastic flows are required(i.e. both the positive and negative growth terms).

Dome growth studies have been performed at Shiveluch. Over a similar period of time in 2005 two methods were used to calculate extrusion rates of the lava dome. Zharinov and Denychuk (2008) used geodetic data as well as long-distance ground photography to calculate the extrusion rate. Zharinov and Demyanchuk (2008) determined the growth rate in 2005 to be 0.64×10^6 m^3 per day. Ramsey et al. (2012) produced calculations of extrusion rates from spaceborne and airborne TIR data over a similar timeframe by tracking the movement of thermally-elevated pixels and calculated the growth rate to be 0.103×10^6 m^3 per day. The authors noted that this growth rate was likely diminished due the removal of material during the observation period from pyroclastic activity.

This new work uses an approach by which the total volume of material lost from the volcanic dome due to block and ash flows can be quantitatively estimated. With this knowledge, an estimate of the likelihood of dome collapse as a function of dome growth can be made.

2.2. Methods

2.2.1. Data Processing

All TIR data for this study are free of clouds over the pyroclastic flow of interest. ASTER data are examined using the US Geological Survey (USGS) Global visualizer viewer (GloVis), and AVHRR data are analyzed using the University of Alaska Fairbanks (UAF) Volcanic Ash Detection,

Avoidance, and Preparedness for Transportation (V-ADAPT) program. The raw data are calibrated to top-of-the-atmosphere spectral radiance (typically in units of W/m^2 sr μm). ASTER data are atmospherically corrected to at-surface radiance in post-processing (Level 2, AST_09T product) (Thome et al., 1998b; Abrams, 2000). In order to determine a cooling rate for the surface materials, the ASTER at-surface radiance data must be separated into emissivity (i.e. the efficiency with which the surface can radiate energy) and brightness temperature. This is accomplished using the emissivity normalization approach (Gillespie, 1985; Realmuto, 1990; Reath and Ramsey, 2013). The result is a unique emissivity image for each of the five ASTER TIR channels and one brightness temperature image. AVHRR data are converted directly into brightness temperature and albedo in near real time for every satellite pass using the Okmok algorithm (Dean et al., 1998; Dehn et al., 2000; Bailey et al., 2010); these data are used here.

Two regions of interest (ROIs) are created in the ASTER images (Figure 2-3). The first ROI represents the pixels corresponding to the recently active lower pyroclastic flow unit, which had a surface area of 3.0 km^2. The second ROI is used to estimate background conditions by focusing on the radiance/temperature/emissivity characteristics of old, inactive pyroclastic flows. It is chosen spatially adjacent to the first ROI at a similar elevation and assumed surface mineralogy (Ramsey and Dehn, 2004; Carter and Ramsey, 2009). The background ROI has an area of 11×11 TIR pixels (9.8×10^3 m^2) to approximately match the size of one AVHRR pixel. Both ROIs are created from the first ASTER scene acquired 35 days after the emplacement of the flow. The average temperatures associated with each ROI are assigned as the representative temperatures of both the flow and the background in each scene. Each subsequent ASTER scene is geo-registered to the first to ensure pixel-for-pixel correspondence, which assured the same area on

the ground is sampled in each ROI. Pyroclastic flow temperatures for the flow under investigation are then normalized to the average background temperature to compensate for any diurnal, seasonal, or weather artifacts.

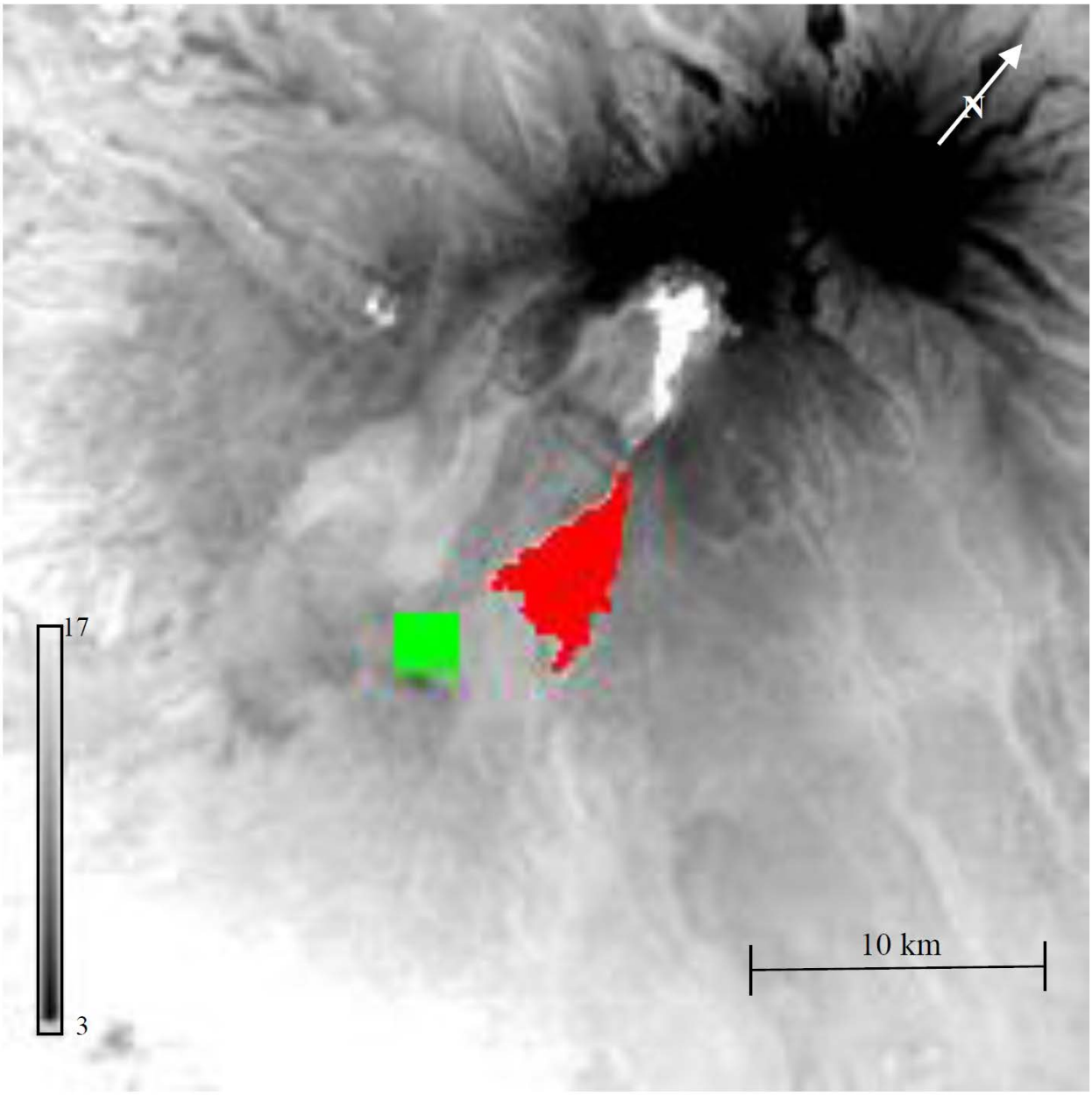

Figure 2-3: ASTER TIR scene acquired over Shiveluch on July 30, 2009 10:50 UTC, temperatures in degrees Celsius. Red ROI denotes area classified as the lower pyroclastic flow, green ROI denotes the area classified as background.

2.2.2. Data Hybridization

Although ASTER data can be acquired quite frequently at high latitudes, the amount of data available for this analysis is increased by including high temporal resolution AVHRR data. These data require further processing to be used with the ASTER data. The 1km^2 pixel size of AVHRR TIR data means that each pixel containing a portion of the "hot" pyroclastic flow also contains a portion of the "cool" background. Therefore, all temperatures for these thermally-mixed pixels will be inaccurate (Rothery et al., 1988). Equation (1) is used to calculate the temperature of the pyroclastic flow, by accounting for this mixing.

$$T_{pixel} = T_{hot}\left(\frac{A_{hot}}{A_{pixel}}\right) + T_{cold}\left(\frac{A_{pixel} - A_{hot}}{A_{pixel}}\right) \quad (1)$$

In this equation: T_{pixel} = observed (mixed) pixel(s) temperature, T_{hot} = temperature of the hot pyroclastic flow surface, T_{cold} = temperature of the background surface temperature, A_{hot} = area of the hot temperature component, and A_{pixel} = total area sampled by all pixels with elevated thermal emissions from the pyroclastic flow. With the background surface temperature known, the equation is solved for T_{hot}. The higher spatial resolution ASTER data also helps to constrain the area of the pyroclastic flow or A_{hot} by overlaying the ASTER data on the AVHRR data (Figure 2-4A). The pixels affected by the lower pyroclastic flow are shown and included in the analysis. It is important to note that no AVHRR pixels sampled both the upper and lower pyroclastic flow units, which allows each flow to be differentiated. The total area and average temperature of the mixed pixels are recorded (A_{pixel} and T_{pixel}). After applying equation 1 to all available clear AVHRR scenes, the extracted temperatures of the pyroclastic flow unit are also normalized to the average background temperatures.

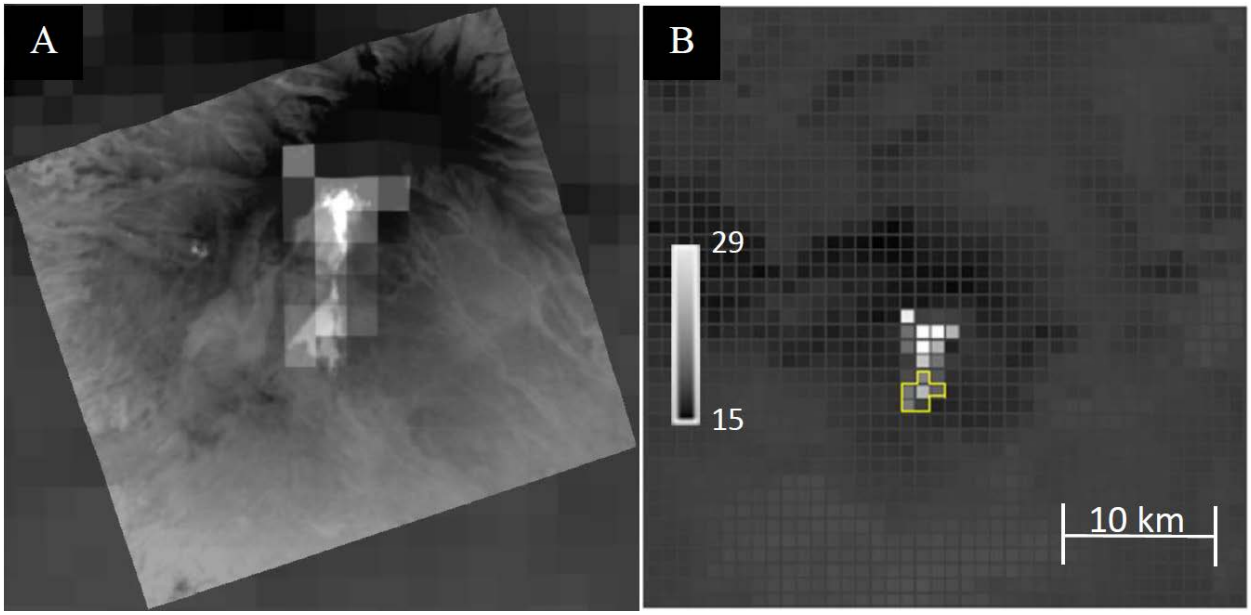

Figure 2-4: AVHRR thermal IR temperature data of Shiveluch Volcano collected on 25 June 2009, 15:21 UTC with (A) an overlay of the ASTER scene (Figure 2-3) and (B) pixels outline in yellow are those that are thermally-elevated and included in analysis.

2.2.3. Estimating the cooling rate of a pyroclastic flow from space

The temperature (above background) of the pyroclastic flow surface in each image is estimated and interpolated to the times of the other images using simple curve fitting. A power law was determined to have the best fit. However, because such a curve becomes asymptotic, the time period under study is modeled to begin 6 hours before the first data point collected by AVHRR.

By establishing a representative equation to model the cooling rate, the approximate time where the basaltic andesite dome collapsed and the pyroclastic flow was emplaced can be determined. However, the temperature of emplacement must first be established in order to determine the time of emplacement. Brightness temperatures associated with the basaltic andesite dome are recorded in the first clear ASTER image. As the dome grows, portions of new,

hot material becomes exposed to the surface. Therefore, the hottest pixel collected over the dome would correspond with the area containing the most recently erupted material. At the time of emplacement of the pyroclastic flow, a majority of the material will be composed of newly exposed basaltic andesite dome material. Therefore, the temperature of the hottest pixel over the dome of Shiveluch, acquired by ASTER on July 30 at 10:50 UTC is considered the representative emplacement temperature of the pyroclastic flow and used to determine the time of emplacement.

The time where the pyroclastic flow reaches ambient temperatures can also be determined from the data and the model fit. The radiometric accuracy for the ASTER brightness temperatures using the emissivity normalization method is ± 1-2°C (Thome et al., 1998a), and ± 2.5°C for AVHRR (Goita and Royer, 1997). Therefore, anything less than 2°C warmer than background temperature is considered noise, and this threshold is chosen as the ambient temperature.

Harris et al., 1998 also used remotely sensed cooling rates to calculate lava effusion rates by taking the change in time and temperature values from a cooling rate and applying them to heat loss equations to find the total heat produced by the material. The mass-heat balance approach is used to estimate the total mass (assuming a density and volume) of material needed to yield the amount of heat measured by the satellite. To determine the heat produced by a flow, the cooling rate must be converted to an estimate of the energy flux from the flow boundary over time. In order to make this conversion the energy lost to convection, radiation, and the cooling effects of rain are considered. Conduction also accounts for a small amount of the heat lost. However, the equation for conductive cooling is related to the depth of the material and

therefore cannot be calculated without first knowing the volume of material. Furthermore, as demonstrated in Head and Wilson (1986), when the surface temperature falls to below 700°C, convective energy dominates the total energy lost. Therefore, conductive cooling is assumed negligible.

Two approaches are used to find the total heat lost from convective cooling. The first relates the amount of energy lost to free convection. Free convection occurs when the wind velocity is zero and the convection of heat from a surface to the air occurs freely without any forcing from wind currents. Head and Wilson (1986) describe the amount of heat lost due to free convection as:

$$Q_{conv}=0.14\ A_{flow\ air}\ [g\ \alpha_{air}\ \rho_{air}/\mu_{air}\ \beta_{air}]^{1/3}\ (\Delta T_{flow}^{4/3}/\Delta t) \quad (2)$$

where A_{flow} represents the area of the flow, g is the gravitational acceleration, and κ_{air}, α_{air}, ρ_{air} μ_{air}, and β_{air} correspond to the thermal conductivity, thermal diffusivity, density, dynamic viscosity, and the expansion coefficient of stagnant air at a temperature of $(T_{flow}-T_{air}/2)$, respectively (Head and Wilson, 1986; Oppenheimer, 1991; Harris et al., 1997b). When wind is present convective cooling shifts to forced convection and as demonstrated in Arya (1988), the equation for heat lost is:

$$Q_{wind}= A_{flow}\ C_H\ U\ \rho_{air}\ cp_{air}\ (\Delta T_{flow}/\Delta t) \quad (3)$$

Here, U is the wind velocity, cp_{air} is the specific heat capacity of air, and C_H is $(U^*/U)^2$. The term U* relates to the frictional wind speed, which is unknown for this specific lava field. However, (U*/U) has been measured for the Amboy lava field by Greeley and Iversen (1987) to have a value of ~0.06. The wind velocity (U) over this flow for the period of study is also unknown, therefore

wind velocities ranging from 0 to 5 m/s will be used to demonstrate the range of convective energy loss at different velocities.

Radiative cooling can be estimated using the computed flow surface temperature and the well-known Stefan-Boltzmann Law:

$$Q_{rad}=\sigma A_{flow} T_{flow}^4 \quad (4)$$

where σ is the Stefan Boltzmann constant (5.67×10^{-8} W/m^2 K^4). Additionally, the heat lost from the presence of rain is calculated from the equation:

$$Q_{rain}= (\Delta R/\Delta t) A_{flow} \rho_{H2O} L_{H2O}^+ \quad (5)$$

where $\Delta R/\Delta t$ relates to the rate of rainfall and L_{H20}^+ is the latent heat of vaporization plus the heat needed to warm the water to 100°C. No distinct value for average rainfall on Shiveluch was recorded for this period, so values ranging from 0 to 3 mm/day are included in the study.

By applying ΔT values recorded in the pyroclastic flow cooling rate curve over the time period from flow emplacement (t_o) to cooling to ambient temperatures (t_f), a cooling curve of the pyroclastic flow is created. The total energy lost (Q_{tot}) from the pyroclastic flow is then calculated by integrating the cooling curve equation from t_o to t_f. This value is entered in the mass-heat balance equation:

$$Q_{tot}=V_{flow} \rho_{flow} cp_{flow} \Delta T_f \quad (6)$$

where V_{flow} is the total volume of the pyroclastic flow and ΔT_f is the total change in temperature from T_o to T_f. By solving for V_{flow} and dividing by A_{flow}, the average flow depth is calculated. We determined that the low surface temperature would mean that convective cooling dominates

the energy loss budget. As this is sensitive to wind velocity, which is unknown, the method described provides limited insight into the actual rate at which the pyroclastic flow lost heat, and hence, provides an inaccurate basis on which to estimate its volume. This necessitated adopting a new approach.

In this new approach, volume is calculated based on the shape of the cooling rate, which is modeled independent of wind velocity. The cooling rate of the pyroclastic flow can be related to the volume of the flow via Newton's law of cooling, which states isothermal cooling of any one material should occur at a rate of exponential decay:

$$T_f = T_o \, e^{\frac{-t}{t'}} \tag{7}$$

where T_f = final temperature, T_o= initial temperature, t= total amount of time (t_f-t_o), and t'= exponential decay time. By using the times and temperatures calculated from the analysis of the satellite data, for the point of emplacement (t_o,T_o) and the point where temperatures reach the ambient range (t_f, T_f), the equation can be solved for t'. The exponential decay time for cooling of a material from a constant initial temperature can be calculated by the equation:

$$t' = \frac{d^2 \, t}{\kappa} \tag{8}$$

where d= depth and t= dimensionless time relating to the manner in which cooling occurs in the material, in the case of cooling from one side this value is $t=\frac{2}{\pi^2}$. Finally, κ= thermal diffusivity, which can be calculated by using:

$$\kappa = \frac{k}{\rho \, cp} \tag{9}$$

where k=thermal conductivity, ρ=density, and cp=specific heat capacity. The values used in this study are based on the average values for basaltic andesite pyroclastic flows. Charbonnier and Gertisser (2008) determined an average density of basaltic andesite pyroclastic flows of 2.2 g/cm^3, which is a combination of basaltic andesite (2.66 g/cm^3) and air (1.25×10^{-3} g/cm^3). With a bulk composition of 82.7% andesite and 17.3% air, a density of 2.2 g/cm^3 is determined. In order to calculate values for the thermal conductivity and specific heat capacity of the same flow, k and cp values for air and basaltic andesite (Wohletz and Heiken, 1992; Waples and Waples, 2004) are combined in the same percentages.

With the value of t' from equation (7), equation (8) can then be solved for depth and converted into an estimate of the pyroclastic flow volume using the surface area measured in the ASTER data (Figure 2-5). An advantage of this approach over that of Harris et al. (1998), is that the model prediction of a cooling rate can be directly compared to the satellite data to determine the correlation between modeled and observed cooling rates.

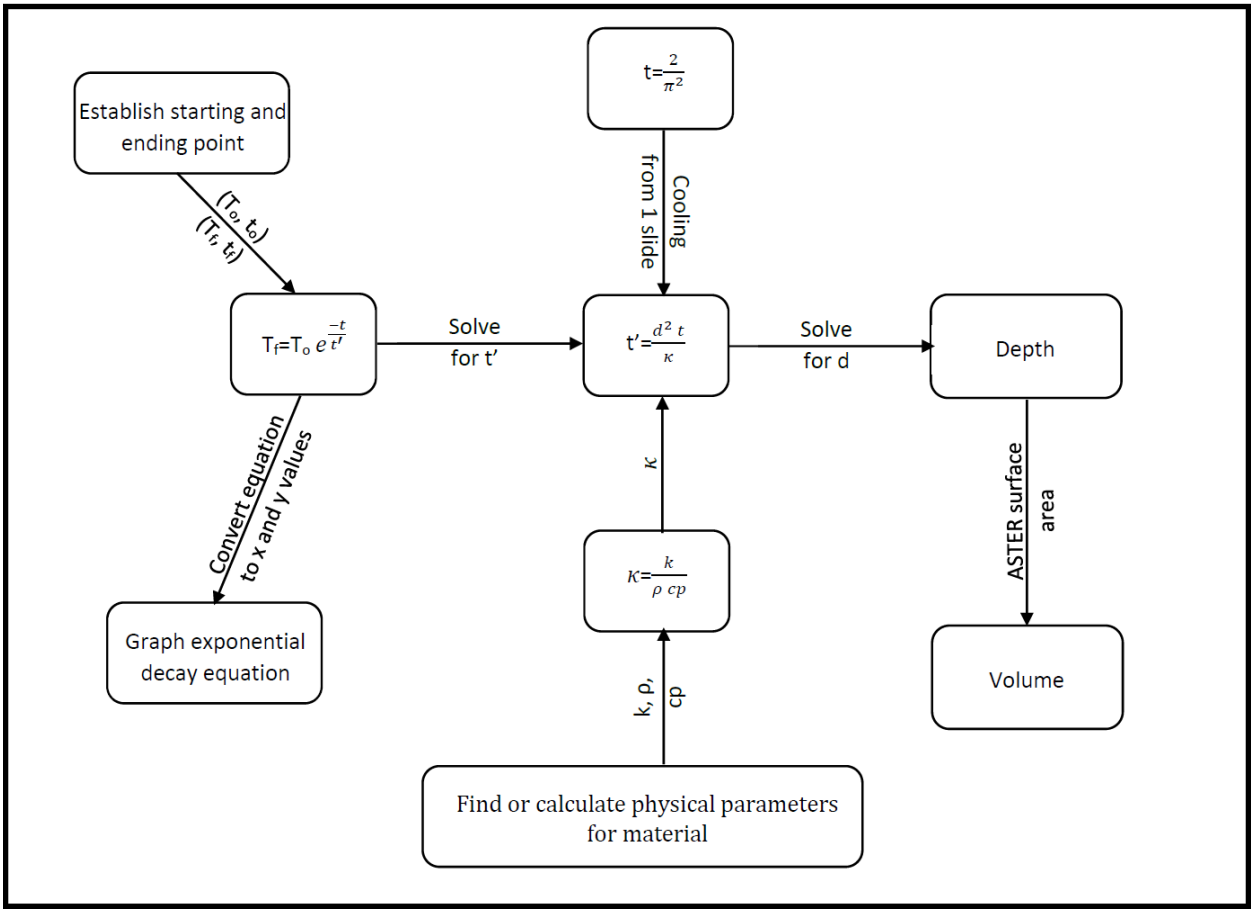

Figure 2-5: Flow chart of first-degree polynomial exponential decay methods and calculations

In some cases, this exponential cooling rate will not correlate with the original data due to more than one isothermal material being present in the sample area. In these cases increasing the degree of polynomial fit from a first order exponential decay equation to a second order may also increase the correlation between the modeled and observed equations. The first step in this process is to identify the transition point where the cooling rate changes from being dominated by the cooling of the first material to that of a second. Thin layers of material with a high thermal diffusivity cool more quickly, resulting in the initial stages of cooling rates being dominated by these materials. Conversely, thick or low thermal diffusivity layers cool more slowly, causing them

to dominate the later stage of cooling rates. A second order exponential decay equation representing this cooling rate can be written as:

$$y= (\frac{a}{100}) A_o e^{\frac{-t}{t'_1}} + (1-\frac{a}{100}) A_o e^{\frac{-t}{t'_2}} \quad (10)$$

The position of the transition point can then be used to find a value for the variable "a" in equation 10, based on the percentage of cooling above and below this point. Additionally, these percentages are indicative of the amount of material found in the flow (i.e., 60% of the cooling occurs above the transition point, the flow is composed of 60% material 1). Also, in this equation t'_1 as well as t'_2 need to be recalculated for the section of the cooling rate curve which they represent. These values are calculated from the equations:

$$T_1=T_o e^{\frac{-t_1-t_o}{t'_1}}, Tf=T_1 e^{\frac{-t_f-t_1}{t'_2}} \quad (11)$$

Both t'_1 and t'_2 are calculated by substituting new values based on the transition point (t_1,T_1) into equation (6). To calculate a value for t'_1, T_1 must be substituted for the final temperature and t_1-t_o for the total time; whereas for t'_2, T_1 must be substituted for the initial temperature and t_f-t_1 for the total time.

Based on seismic readings from KVERT and prior research performed on Shiveluch (e.g., Ponomereva et al, 1998; Belousov, 1999; KVERT, 2009), this deposit was identified as a block and ash flow. Thus, the thermal diffusivity (κ) of these equations are based on the physical parameters for basaltic andesite pyroclastic ash and basaltic andesite. In this model, the block and ash layers represent two separate, isothermally cooling units of material, basaltic andesite pyroclastic ash and blocks (Figure 2-6A) each comprising a certain percentage of the flow. The

ash would have cooled quickly and dominated the early cooling, and the denser block would cool slowly, dominating the later cooling. With these values, the second order exponential decay equation can be calculated and plotted to demonstrate its fit to the given data points. The t'_1 and t'_2 values from equation (11) can then be entered into equation (8) and used to calculate depth for these two materials. The volume of the flow is calculated based on the depths and percentages of these materials over the surface area of the flow, as determined using the ASTER sensor. The second degree polynomial method is described by the Figure 2-7 flow chart.

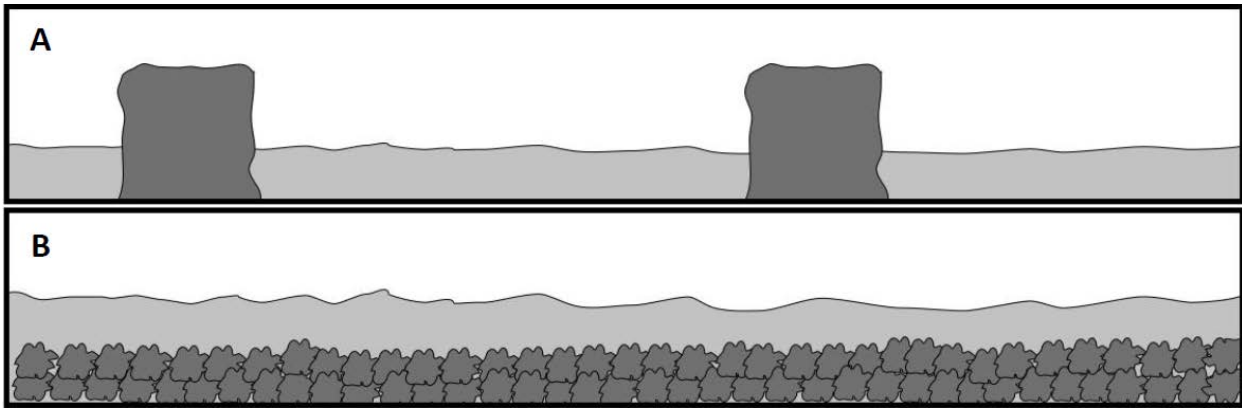

Figure 2-6: Schematic representation of the two modeled depositional environments of the block (dark gray) and ash (light gray) layers, (A) block and ash units representing a checkerboard mixing in the pyroclastic flow and (B) smaller block layer is first deposited and later covered and insulated by the ash layer

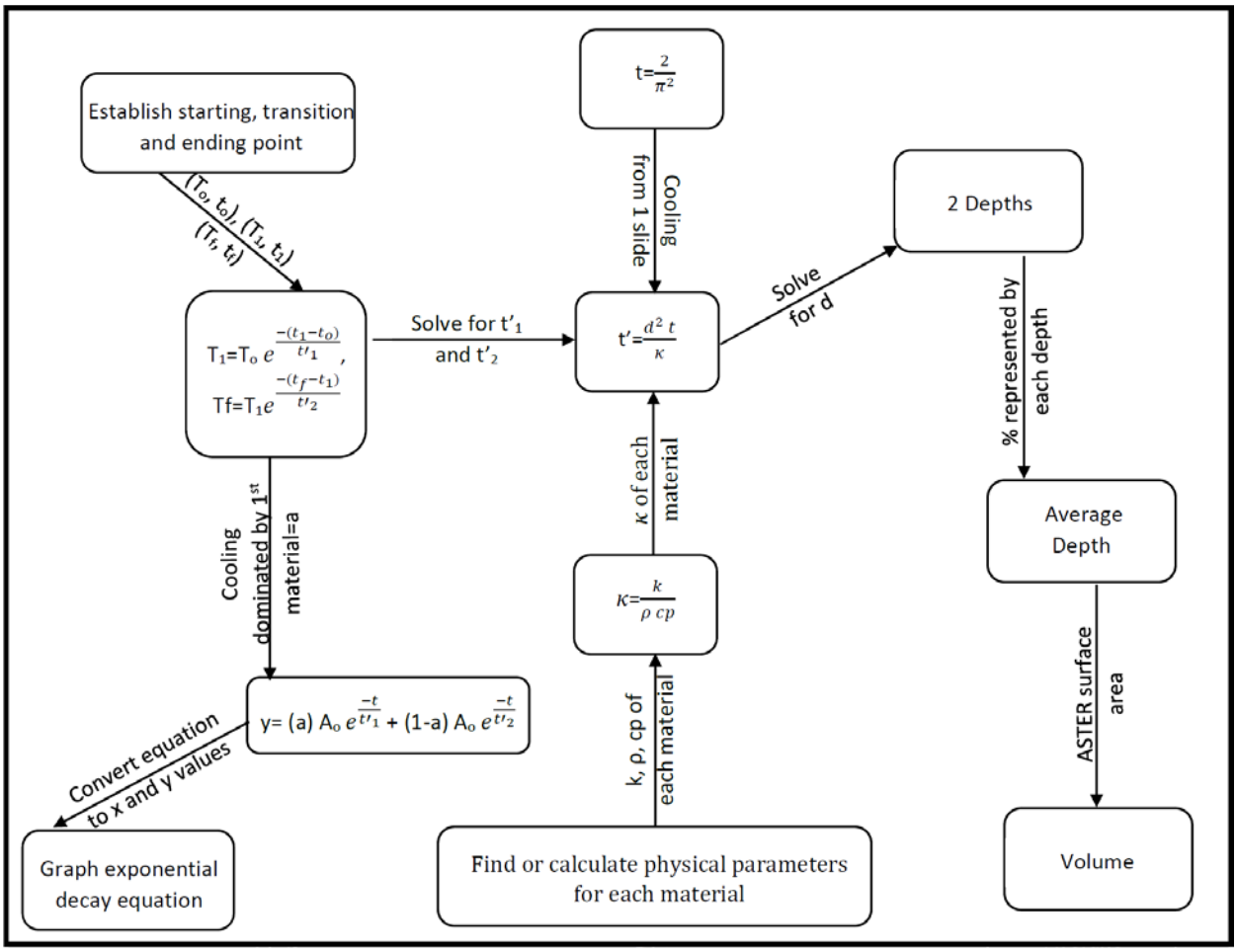

Figure 2-7: Flow chart of second-degree polynomial exponential decay methods and calculations

An approach was also developed for a situation where the pyroclastic flow is not composed of two independently isothermally cooling materials of varying depths. In this method the depth of the flow is uniform and layer 2 is buried by layer 1, causing layer 2 to be insulated by layer 1 (Figure 2-6B). Using this approach, layer 1 cools the same way as in the previous method and its depth remains the same value that was calculated for the average depth of layer 1. In order to calculate the non-isothermally cooling and the insulated depth of layer 2, the following equation is used:

$$t'_2 = \frac{\overline{d_2}^2 t}{\kappa_2} - \frac{\overline{d_1}^2 t}{\kappa_1} \quad (12)$$

Here, κ_1 and κ_2 represent the thermal diffusivity for layer 1 and 2, and $\overline{d_1}$ and $\overline{d_2}$ represent the average values of the depths these layers. For layer 1 this would be the previously calculated average depth of the material, based on its percentage of flow composition. The equation is solved for $\overline{d_2}$, which represents the average depth of layer 2 required to underlay layer 1 and still produce the exponential decay related to t'_2. These two depths are combined to find the average total depth of the flow, which is then used to calculate the volume.

2.2.4. Dome Growth Calculations

To find the total amount of material lost to pyroclastic flows each day, the average thickness calculated for the lower flow is assumed to be the total thickness of the entire (upper and lower) flow. This thickness is multiplied by the total area of the flows (upper and lower) to find the total volume of a typical Shiveluch pyroclastic flow. The total number of recorded pyroclastic flows from June 1, 2009 to December 31, 2009 is extracted from the archival data of weekly activity for Shiveluch gathered by the Smithsonian Institute Global Volcanism Program (2009). The number of flows multiplied by the total flow volume and divided by the number of days in the study results in the total amount of material lost to pyroclastic flows per day.

2.3. Results

Inspection of the ASTER data archive acquired after the June 25 pyroclastic flow revealed 4 cloud-free scenes acquired before the flow was covered by later activity (Figure 2-8). The normalized temperatures of the pyroclastic flow found in these 4 scenes are plotted (Figure 2-9). As a result of the time gap between the onset of the flow to the point where the first ASTER scene was captured, the rate of cooling had slowed, resulting in an apparent linear cooling rate, which is assumed to be incorrect.

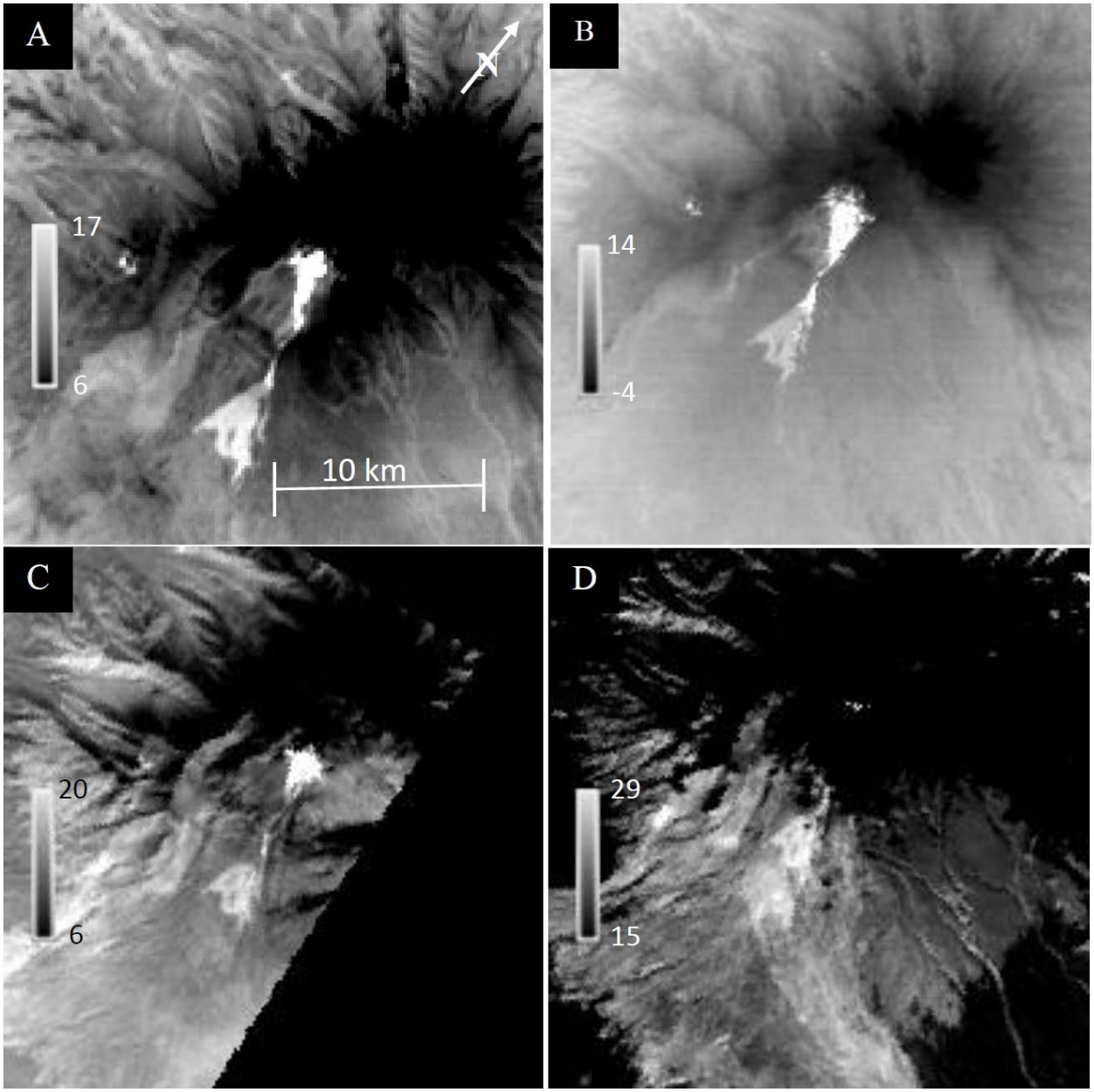

Figure 2-8: Thermal infrared ASTER brightness temperature data showing the four clear scenes of Shiveluch Volcano used in the study. All temperatures in degrees Celsius. (A) ASTER data acquired on July 30, 2009 @ 10:50 UTC. (B) ASTER data acquired August 15, 2009 10:50 UTC (C) ASTER data acquired August 28, 2009 00:44 UTC (D) ASTER data acquired September 6, 2009 00:38 UTC

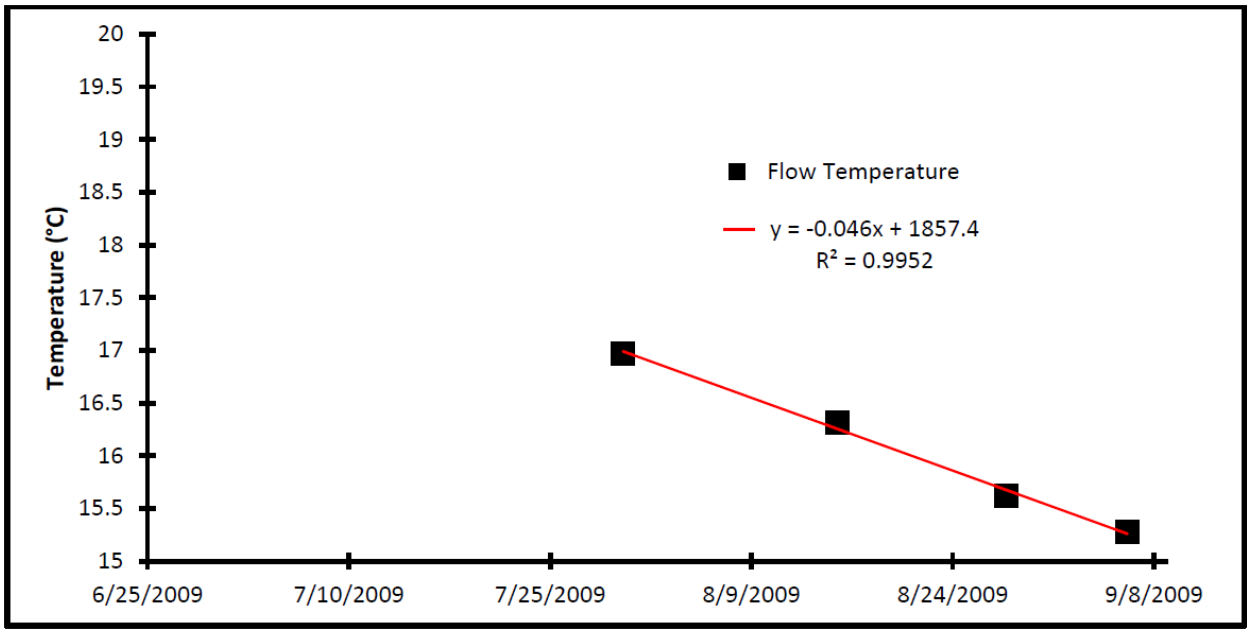

Figure 2-9: ASTER pyroclastic flow temperatures plotted in a temperature versus time graph.

The first clear AVHRR capture of the pyroclastic flow occurred June 25 at 15:21 UTC, just hours after its emplacement. Five other clear AVHRR scenes were acquired between the time of the flow emplacement and the first clear ASTER scene. Where pyroclastic flow temperatures calculated from the AVHRR data are combined with the ASTER data, an exponential cooling curve becomes apparent (Figure 2-10A). The best fit line representing the pyroclastic flow temperature is modeled as: $y=29.49x^{-0.55}$ with an r^2 of 0.91 (Figure 2-10B).

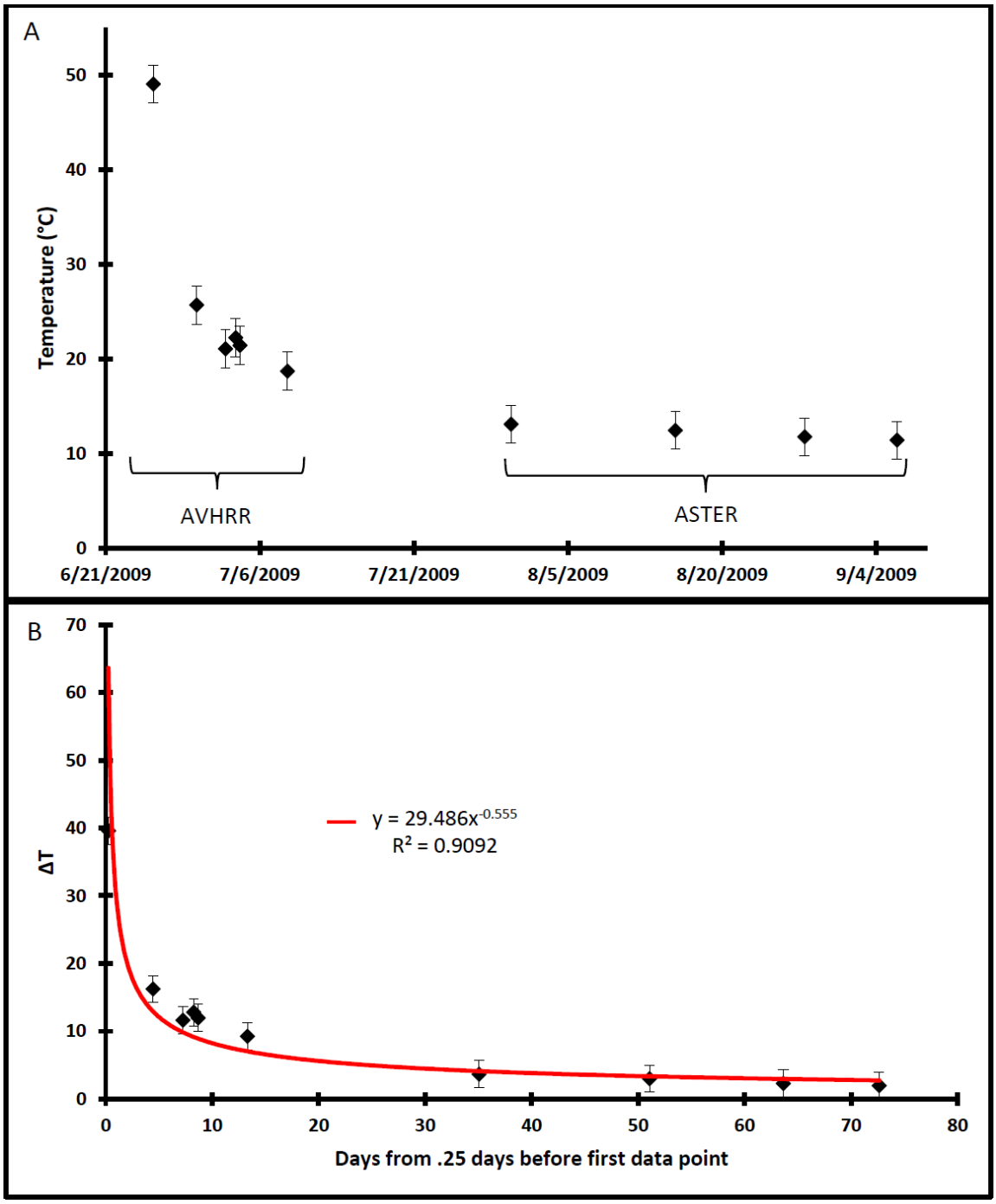

Figure 2-10: AVHRR and ASTER pyroclastic flow temperatures versus time (A) measured/modeled temperatures of the flow and (B) same temperatures with a best fit power rule equation shown. Error bars denote the ~2°C uncertainty where deriving brightness temperature from the satellite data.

From this best-fit equation, the time of emplacement is calculated by first establishing a temperature of emplacement. The hottest pixel at the summit of young Shiveluch in the ASTER scene captured on July 30 (Figure 2-8A) is 95°C hotter than background temperature. Accepting this brightness temperature to be the equivalent to the emplacement brightness temperature and solving the cooling equation yields a value of 0.121 days (2.9 hours). This can be interpreted as the time from the graph's start (June 25, 2009, 09:21 UTC), or equivalent to a calculated emplacement time of June 25, 2009 at 12:14 UTC. This corresponds well with the emplacement time window determined from both the seismic and satellite imaging data of the area. Repeating this approach for the ambient temperature (2°C above background) results in a time of 127.5 days to reach the ambient temperature.

Initially the total volume and average depth of the flow are calculated by converting the cooling rate into a cooling curve using values of radiant, rain, and convective cooling. A range of different wind velocities from 0 to 5 m/s are used (Figure 2-11). Based on these cooling curves and the mass-heat balance equation, it is determined that the modeled flow depth could vary from 0.22, 3.32, 9.95, to 16.59m deep with wind speeds of 0, 1, 3, and 5 m/s, respectively. Due to this large uncertainty, a different approach is used.

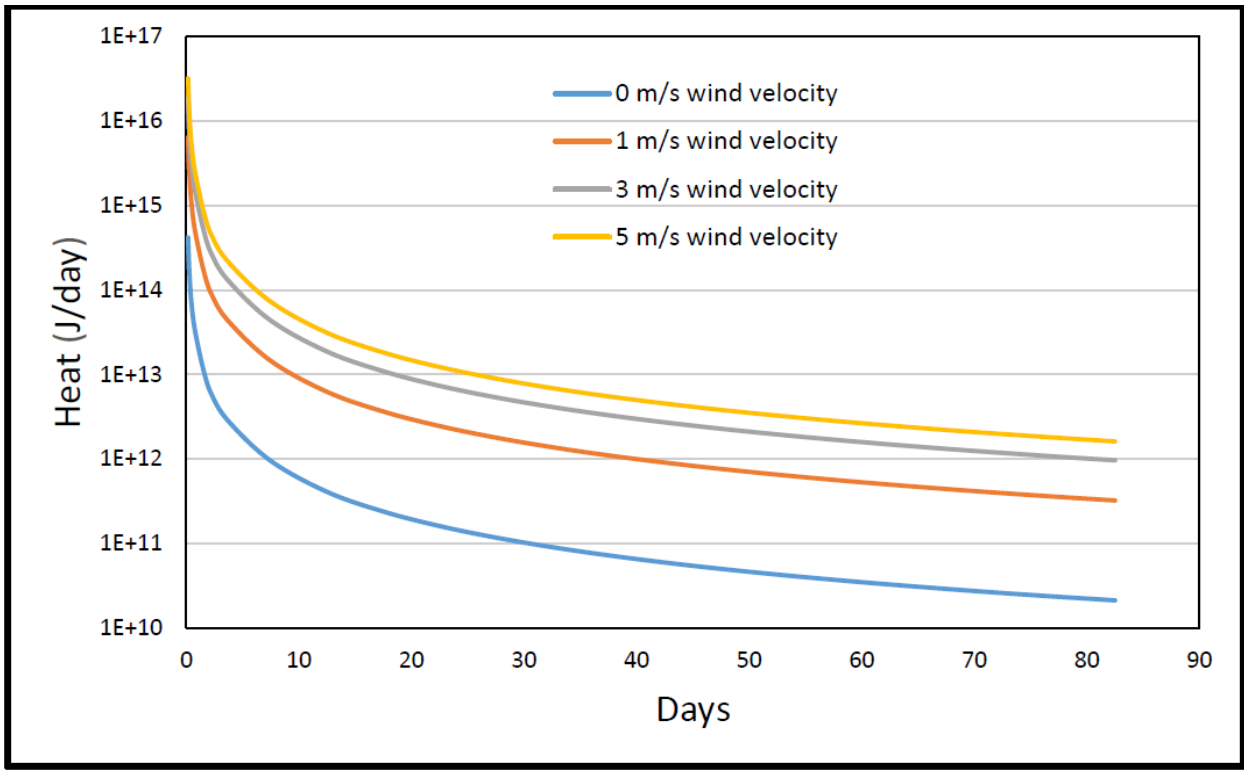

Figure 2-11: Cooling curves dervied from the cooling rate equation in Figure 2-10. These curves range represent the wide range of cooling possibilities based on the uncertainty of the wind speed.

A new method is developed where total volume and average depth of the flow are calculated based upon the shape of the cooling rate. By using the exponential decay equation (7) with the given starting and ending points of T_o=95, t_o=0.121 and T_f=2, and t_f=127.51, a value of 35.98 for t' is calculated. An average depth of 4.8m can be calculated using the value of t' in equation (8) with the average values of k = 3.064 W/m K, ρ = 2.2 g/cm^3, and cp = 850 J/kg K for basaltic andesite pyroclastic flows. To confirm the accuracy of this approach, the exponential decay equation created from these values are plotted against the original cooling rate captured by ASTER and AVHRR (Figure 2-12). Examining Figure 2-12 reveals that a first order equation for exponential decay through the starting and ending points of this graph do not correlate well with the cooling rate data collected.

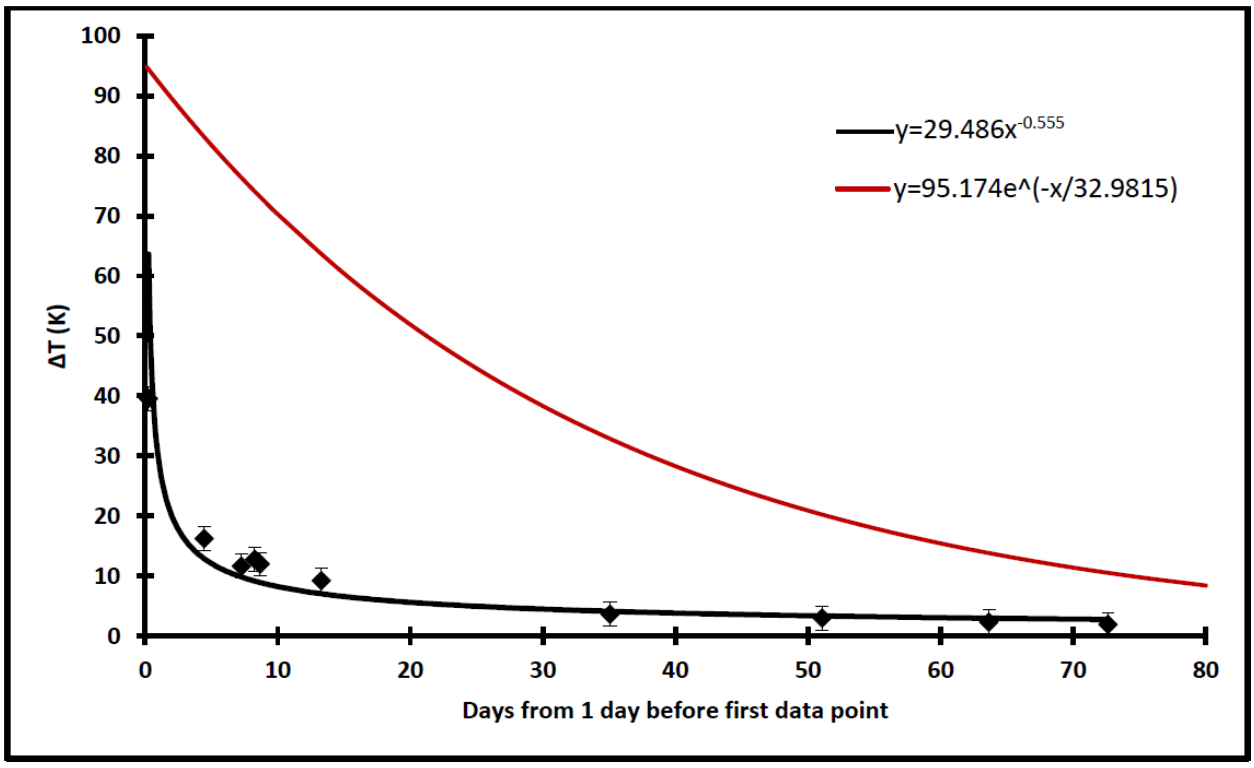

Figure 2-12: First order exponential decay cooling equation, in red, used to match the starting and ending points of the observed cooling rate equation.

The bi-modal size distribution of typical block and ash flows necessitates a second degree polynomial. The point where the cooling of the flow transitions from fast to slow cooling (Figure 2-13) occurs at approximately 5 days and 12.1°C (t_1, T_1). Based on this transition point, values of t'_1=2.421 and t'_2=68.1624 are calculated. In the case of material 1 (quickly cooling), values for basaltic andesite pyroclastic ash of ρ=1.9 g/cm^3, cp=925.7 J/kg K, k=1.71 W/m K (Charbonnier and Gertisser, 2008) are used to calculate κ. The values for material 2 are based on basaltic andesite, ρ= 2.66g/cm^3, cp=815 J/kg K, and k=3.7 W/m K (Wohletz and Heiken, 1992; Waples and Waples, 2004). A thermal diffusivity of 3.50×10^{-3} m^2/hour is calculated for material 1 and 6.14×10^{-3} m^2/hour for material 2, from these data depths of 1.00178m (~1 m) for material 1 and 7.04 m for material 2 are calculated. The location of the transition point on the temperature axis revealed

that 88% of the cooling is dominated by the more quickly cooling material and 12% is dominated by the slowly cooling material. Using these percentages for each material, the flow is determined to have an average thickness of 1.73 m over a total surface area of 3.0 km^2, the lower flow portion is therefore determined to have a volume of 5.12×10^6 m^3. Finally, based on equation (10), a second degree polynomial exponential decay equation of $y=83.7531e^{-x/2.421} + 11.4209e^{-x/68.1624}$ is determined to best represent these values (Figure 2-13).

Additionally, the values of t' and the average depth of material 1 calculated from the second degree polynomial model are used in equation (12) to find the average depth of material 2 where the depth is uniform throughout the flow and insulated by an overlaying material 1. In this situation, material 2 would have to be 1.85m thick which yields a total flow thickness of 2.73m and would produce a volume of 8.10×10^6 m^3. Therefore, the range in volume of the flow is bounded by the lowest volume of material where the flow is cooling isothermally (5.12×10^6 m^3) and the largest volume where the flow has a uniform depth (8.10×10^6 m^3).

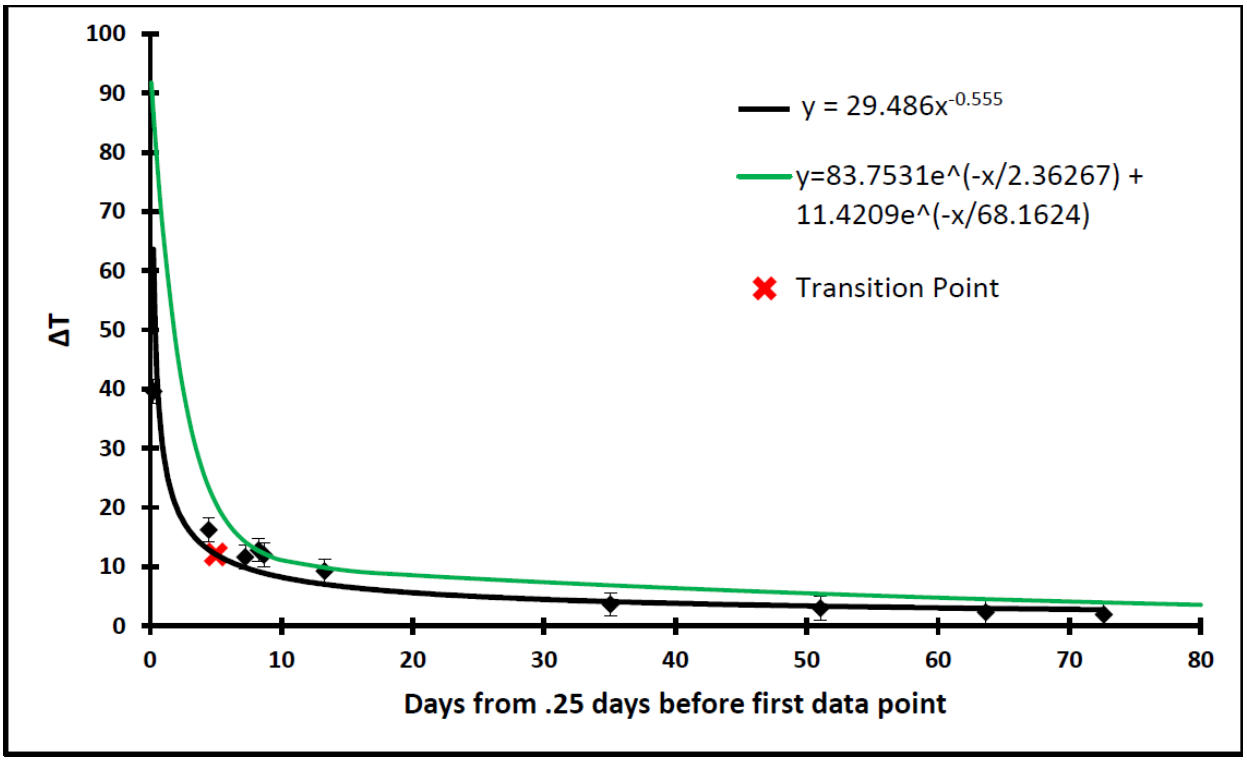

Figure 2-13: Second order exponential decay cooling equation, in green, used to match the starting, transition, and ending points.

2.3.1. Dome Growth Rate

Combining the surface areas of the upper (0.5 km^2) and lower (3.0 km^2) pyroclastic flows and assuming the thickness of the entire deposit is bounded by the range from 1.73 to 2.73m, the total volume range varies from 5.98×10^6 to 9.39×10^6 m^3. According to the Global Volcanism Program (2009), at least 8 pyroclastic flows occurred in a six month period between June 1, 2009 and December 31, 2009. Therefore, a range of 4.78×10^7 to 7.51×10^7 m^3 or 2.61×10^5 to 4.10×10^5 m^3/day of volcanic material was removed from the dome by pyroclastic flows. This range lies between the two growth rates calculated for the dome through different techniques (Zharinov and Demyanchuk, 2008; Ramsey et al., 2012). Depending on which technique is more accurate,

the dome would vary between a range of 0.38×10^6 – 0.23×10^6 m^3/day (growth) to -0.16×10^6 – -0.31×10^6 m^3/day (loss).

2.4. Discussion

2.4.1. Error Analysis

2.4.1.1 Data Integration

For this methodology, ASTER data alone are typically not enough to create a complete cooling rate profile due to the sparse cloud-free data over long periods following an eruption. Data acquired by the AVHRR sensor subject to the thermally integrated pixel equation (1) are required to expand the timeframe. In this situation, however, difficulty arises where attempting to determine which AVHRR pixels are affected by hot temperatures from only the lower pyroclastic flow unit (Figure 2-4). The 950m separation between the upper and lower flow units results in very little mixing of the thermal energy from the two units. The lower unit contains at most only $2.7\times10^{-3}km^2$ of the upper unit, which would change the final flow temperature by a maximum of 4.0×10^{-6} °C.

2.4.1.2. Flow Emplacement Temperature

The assumed emplacement temperature of 95°C above background may appear too low. During a gravitational collapse based pyroclastic flow at Soufriere Hills, physical emplacement temperatures of 99-121°C, 99-149°C, and 200-250°C were measured by Cole et al. (1998). Pixel

temperatures obtained remotely are brightness temperatures, which are lower than the actual kinetic temperatures due to less than unity emissivity values and pixel-integrated temperatures (Rybicki and Lightman, 1977, 2008). For example, a surface with an average emissivity of 0.8 would produce a brightness temperature that is 80% of the kinetic temperature if the incorrect emissivity of 1.0 is assumed. This basaltic andesite composition has an emissivity range from 0.90 to 0.98 (average of 0.94). Using this average emissivity, the pixel-integrated kinetic temperature at emplacement would be 101°C. This is approaching the lower range of emplacement temperatures recorded at Soufriere Hills and it is within range of physical temperatures recorded at other block and ash pyroclastic flows (Voight and Davis, 2000; Charnonnier and Gertisser, 2008).

2.4.1.3. Alternative Methods for Volume Calculations

Methods similar to those used in Harris et al., (1998) are used to calculate a volume for this pyroclastic flow. The energy lost due to conductive cooling is negligible at the surface temperatures recorded for this flow. Additionally, the total amount of heat lost from both radiative and rain cooling accounts for a change in modeled depth of only 0.3 mm. Therefore, convective heat loss dominates. In order to calculate the total amount of heat lost by each type of cooling, approximately 9 physical parameters relating to the flow and flow environment are needed. Some of these parameters, such as the frictional wind speed, the wind speed, or the amount of forced and free convection can only be crudely estimated without in situ measurements.

Comparing the shape of the cooling rate using exponential decay, in contrast, relies on only three physical parameters, all of which remain constant. These are the density, specific heat capacity, and the thermal conductivity of the material. Once the composition of a flow is established, which can be done remotely through analysis of the TIR emissivity spectra, these 3 parameters can easily be found in literature or calculated. This allows depths and volumes of flows to be calculated, which provides the possibility of applying this approach to any hot flow unit remotely recorded in the TIR wavelength region.

2.4.1.4. Surface Temperature

The exponential decay modeling method shown here is dependent upon the isothermality of the surface, which allows an accurate value of surface temperature to be made. If large cracks are present in the flow's surface, satellite data could record temperatures influenced by these warmer areas, which would result in the data over-estimating the surface temperatures. There are several results that suggest this is not the case. First, in several field campaigns no large cracks on the surface of the Shiveluch pyroclastic flows were observed (M. Ramsey, pers. commun.). Additionally, as demonstrated by Wright et al (2000), large hot cracks tend to have a much larger effect on increasing the average radiance in the Short Wave Infrared (SWIR) where compared to TIR wavelengths. This would allow the flow to remain radiant in the SWIR for an unrealistic amount of time. However, where observing the AVHRR SWIR wavelengths of this flow, no emitted radiance is seen after the first eleven days. If cracks are present of the surface of this flow, the amount of energy they produce must be very low. Therefore, any cracks would be small

enough to not significantly affect the detected radiance and the derived surface temperature is considered accurate.

2.4.1.5. Accuracy of Dome Growth Estimates

From June 1 to December 31, 2009 material is lost from the dome at a rate of 0.26×10^6 m^3 to 0.41×10^6 per day. Using TIR data, Ramsey et al. (2012) calculated a 2005 extrusion rate of 1.03×10^5 m^3 /day, whereas using geodetic data, Zharinov and Demyanchuk (2008) calculated an extrusion rate of 6.4×10^5 m^3/day. The extrusion rate of geodetic data indicates the dome gains volume throughout this entire 6 month period, increasing the likelihood of dome collapse. However, from October 22, 2009 until November 11, 2010, no collapses were reported (Global Volcanism Program, 2011). Therefore the dome was likely losing volume in the last half of 2009, supporting the slower dome extrusion rate calculated by Ramsey et al, 2012. Using this rate over the 6 month period, the dome lost volume at a rate of -1.58×10^5 to -3.07×10^5 m^3/day.

Currently, this method of measuring the growth rate of a lava dome can only be used as an estimate for several reasons. First, domes do not extrude at a constant rate, measurements calculated in 2005 could be very different in 2009. Also, many of the flows during this study period occurred in quick succession (Global Volcanism Program, 2009) and are not captured by the ASTER sensor due to inclement weather conditions and low temporal resolution. This can lead to a misrepresentation of both the number and the size of flows.

2.4.2. Pyroclastic Flow Structure

The second degree exponential decay model, based on the assumption of isothermal cooling, results in a fine-grained layer that is ~1m deep, comprising 88% of the pyroclastic flow composition, and a blocky layer that is ~7m deep, comprising the remaining 12%. At a pixel-integrated brightness temperature of 12.1°C and 5 days after flow emplacement, the fine-grained material has cooled to a point where the hotter blocky layer dominates. However, it is unlikely that this entire flow cools isothermally and 88% of the flow is covered exclusively by ~1 m of fine-grained material and the remaining portion covered exclusively by ~7m blocks. Whereas such environments do occur on Shiveluch (Figure 2-14), it is clear that isothermal heat loss does not extend over entire flows (Figure 2-15). To account for these situations where blocks are buried by the fine-grain material (Druitt, 1998; Schwarzkopf et al., 2005) an alternative approach can be considered where the flow does not cool isothermally and the depth of the flow is uniform. In this case an average depth of 2.73m would be constant throughout the entire flow. Both of these models are used to calculate the extremes of the largest and smallest calculated volumes of the different depositional environments of block and ash flows.

Both of these models calculate average thicknesses that are typical of block and ash flows. At Soufriere Hills Volcano, Calder et al., (1999) observed the largest block and ash flow to "produce thick (1-15m), coarse grained deposits, confined to valleys with blocks of up to several meters in diameter". Belousov et al., (1999) studied the Holocene history of many block and ash flows on Shiveluch and found deposits ranging from 1-5 m thick, which agrees with the thicknesses calculated in this study.

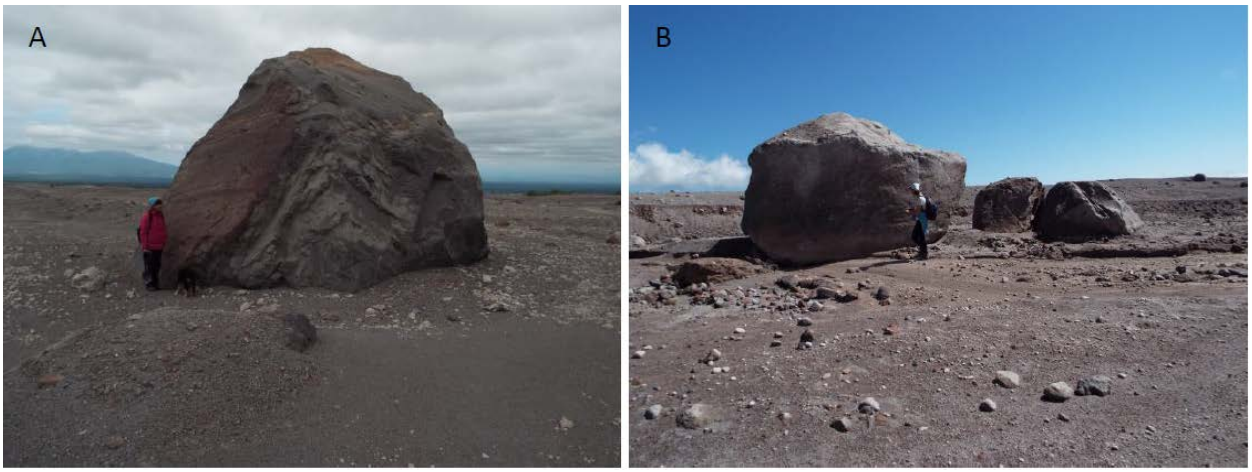

Figure 2-14: Photos of the Shiveluch block and ash flow in 2015 (taken by J. Krippner) (A) ~6m block visible above the finer-grain layer on the 2005 deposit ~12km from the summit. (B) a group of large blocs visible above the fine-grain layer from the 2010 deposit ~15 km from the summit.

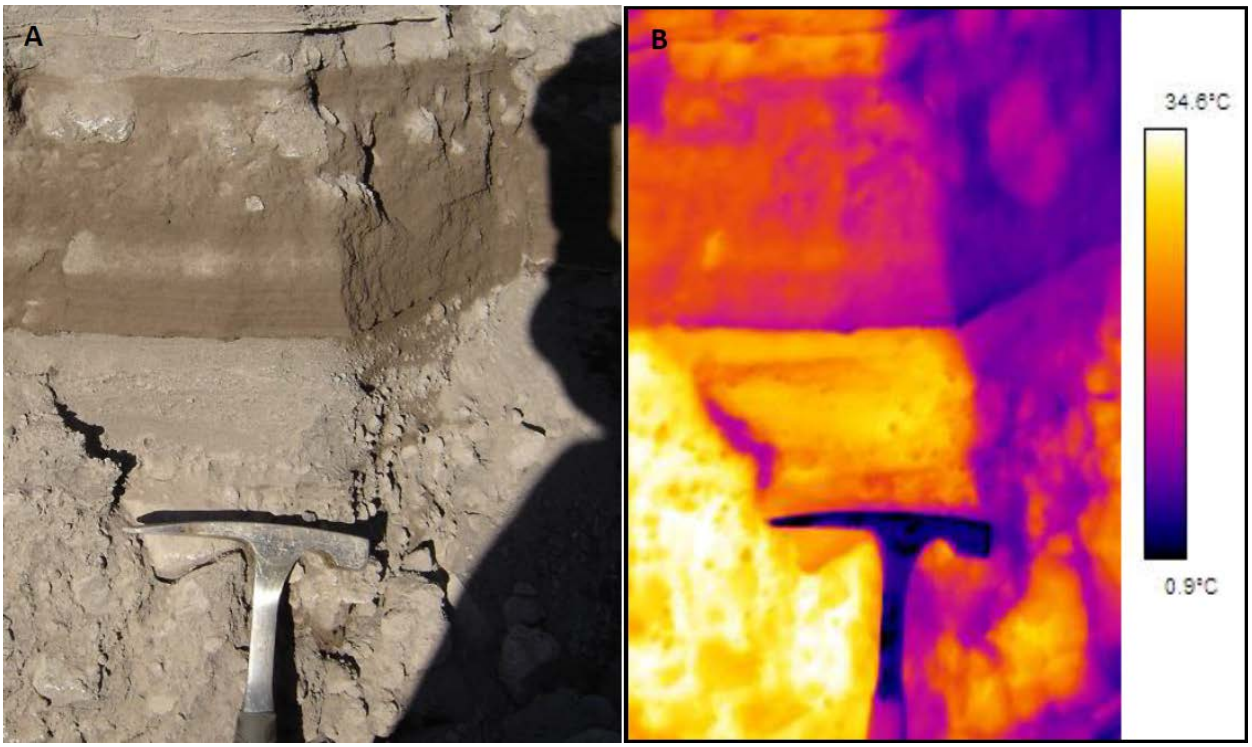

Figure 2-15: Images of a block and ash flow cross-section in 2005 (taken by M. Ramsey). The images show the upper ~1m with a buried warmer block-rich layer and a cooler fine-grained upper layer. (A) visible image and (B) TIR image.

2.4.3. Minimum amounts of data required for analysis

In order to use this method with the smallest number of data points, at least three TIR scenes of a pyroclastic flow must be collected and one of these scenes must be acquired from a high spatial resolution sensor. The high spatial resolution scene determines the surface area of the flow and enables the use of the thermally-integrated pixel equation on higher temporal resolution data. The first point should be acquired within three days of emplacement and the last point should be a minimum of ten days after emplacement. With these three points a best fit line can be created to form an equation that represents the cooling rate. If the flow of interest is a block and ash flow, a second order polynomial equation will be needed. In this case, the cooling rate between the first and second point would capture the rapid cooling rate and the second to third point would capture the slow rate. If no difference is observed between cooling rates in these two periods, a second order polynomial is likely unneeded.

2.5. Conclusions

Pyroclastic flows are one of the most dangerous hazards associated with active volcanism. These flows cover large areas and some tend to occur in quick succession, causing older pyroclastic flows to be covered by new flows. Because of these factors measuring the volume of a recent pyroclastic flow can be extremely dangerous and difficult. However, the methods shown in this study provide a way for pyroclastic flow volumes to be measured entirely remotely. This is achieved by first establishing a cooling rate of a pyroclastic flow. As long as one high spatial resolution TIR ASTER image is captured to establish the surface area of the flow, the thermally

integrated pixel equation (1) can be used to include scenes captured by the higher temporal resolution MODIS and AVHRR sensors to increase the number of points in the data set. By including these data, a more complete cooling rate dataset is establish over the limited time where the pyroclastic flow is exposed to the surface. To use these methods with limited data, a minimum of three TIR scenes are needed, with one scene acquired within three days of emplacement and one at least ten days after emplacement. These data can be used to form an equation representing the cooling rate, provided at least one of these scenes is ASTER based. With this information, and by following the steps outlined in this study, cooling rates can be matched to an exponential decay equation and the range of volumes and depths of the pyroclastic flow can be determined. Furthermore, the growth rate of the corresponding dome can then be calculated by finding the rate at which the dome is extruded and subtracting the rate at which material is lost to block and ash flows. By having knowledge of the rate at which the dome is gaining or losing material, the potential risk of the occurrence of a new pyroclastic flow can be estimated.

Also, because this method relies on the prior knowledge of only three physical parameters, specific heat capacity, density, and thermal conductivity, it can be repeated on any pyroclastic flow where the composition is known. This extends its usefulness to any volcano observed by a TIR sensor with a high enough spatial resolution to accurately determine the surface area of a flow.

2.6. Acknowledgements

Funding for this research was made possible by NASA under the Science of Terra and Aqua Research Program (NNX11AL29G) and the ASTER Science Team. The research presented here would also not have been possible with the support of the people and programs available through V-ADAPT, Inc. and the help of Dr. Rainer Johnsen in the Department of Physics and Astronomy at the University of Pittsburgh.

3. PREDICTING ERUPTIONS FROM PRECURSORY ACTIVITY USING REMOTE SENSING OF THERMAL ANOMALIES

Reath, K.A.[1], Ramsey, M.S.[1], Dehn, J.[2], Webley, P.W.[2]

[1] Department of Geology and Planetary Science, University of Pittsburgh, 4107 O'Hara Street, Pittsburgh, PA 15260

[2] Geophysical Institute, University of Alaska Fairbanks, 903 Koyukuk Drive, Fairbanks, AK 99775

3.1. Introduction

With 29 currently active volcanoes, the Kamchatka Peninsula is one of the most volcanically active regions on Earth. Volcanic hazards such as lahars, pyroclastic flows, earthquakes, and ash-clouds have been associated with eruptions in this area. This moderate/high level of volcanic activity has long been an area of interest (e.g., Gorshkov, 1959; Fedotov, 1984; Fedotov and Masuerenkov, 1991; Casadevall, 1993; Belousov et al., 1999; Ramsey and Dehn, 2004; Carter and Ramsey, 2009). This subduction zone also contains a slab window between the Pacific, Komandrsky, and Okhotsk plates, occurring at the point where the Aleutian island arc meets Kamchatka, which leads to this increased volcanic activity and can alter magma compositions over relatively short distances (e.g., Yogodzinski et al., 2001; Portnyagin et al., 2005; Jiang et al., 2009; Koloskov et al., 2014). Carbon dating and detailed mapping of historic flows determined the activity at each volcano for the past 10 Ka - 50 Ka (Braitseva et al., 1995), which identifies the most historically active volcanoes as: Kluichevskoi, Bezymianny, Tolbachik, Kizimen, Sheviluch, Alny, and Gamhen volcanoes (Figure 3-1). Many of these same volcanoes remain some of the

most active in the region today. The hazards associated with these eruptions create a limited local risk due to the low population concentration (Rose and Ramsey, 2009). Larger scale eruptions, however, produce ash-clouds that pose an increased risk to the approximately 200 aircraft and 200,000 people that fly over the area daily (Miller and Casadevall, 2000). Recent volcanism in the region has been monitored with spaceborne data by the Kamchatka Volcano Emergency Response Team (KVERT) and the Alaskan Volcano Observatory (AVO).

Figure 3-1: Location map of the volcanoes found in the Kamchatka Peninsula with Kliuchevskoi volcano denoted in bold font. Modified from Rose and Ramsey, (2009).

Precursory activities of the volcanoes in this region (Figure 3-1) are varied. For example, Bezymianny volcano tends to be somewhat predictable, with thermal energy released from the summit that gradually increases until an eruption occurs (Carter et al., 2008; Sobolevskaya and Senyukov, 2008; van Manen et al., 2010; van Manen et al., 2013). Conversely, Tolbachik volcano has a history of large scale fissure eruptions occurring with little to no interpretable thermal precursory activity (Edwards et al., 2013; Kugaeunko et al., 2014). Kliuchevskoi volcano consistently produces precursory activity, however this activity has had limited application to predicting the size and duration of an upcoming larger eruption. With the current methods available to monitor thermal activity, only precursors days to weeks prior have been linked to an upcoming eruption at Kliuchevskoi. This type of activity is common to many volcanoes throughout the world (e.g., Francis and Rothery, 1987; Oppenheimer et al., 1993, Harris et al., 1997a; Dehn et al., 2002; Pergola et al., 2004; Pergola et al., 2009; Marchese et al., 2014). A more detailed study of the precursory history of Kliuchevskoi using the current suite of spaceborne TIR sensors could provide a methodological approach for volcanoes world-wide.

3.1.1. Monitoring of North Pacific Volcanoes

During the 1989-1990 eruption of Redoubt volcano in Alaska, AVO developed a color-coded alert system for monitoring volcanoes and the associated risks (Guffanti and Miller, 2013). This system more effectively communicated volcanic activity levels to non-scientists. It has been modified in subsequent years and adopted by the International Civil Aviation Organization (ICAO) as the recommended alert-system for all volcano observatories world-wide. Although still somewhat qualitative, the AVO system is the only standardized international volcano alert protocol

currently in use (Fearnley et al., 2012). The color codes used in this system (Green, Yellow, Orange and Red) represent lower to higher levels of concern and shorter time frames for the expected onset of eruption. The United States Geology Survey (USGS) now employs a similar system where the terms Normal, Advisory, Watch, and Warning replace Green, Yellow, Orange, and Red.

In Kamchatka, KVERT provides status reports of volcanic activity to the local authorities and international community regarding any imminent volcanic risk (Heiken et al., 1992; Schneider et al., 2000; Neal et al., 2009). These status updates are determined using an array of monitoring instruments, including seismic and GPS stations, ground-based visual and web camera observations, and low-spatial, high-temporal resolution orbital satellite data. The satellite data are collected and maintained by several groups such as the Moderate Resolution Imaging Spectroradiometer (MODIS) volcano archive (MODVOLC) used by KVERT (Dehn et al., 2000; Schneider et al., 2000; Wright et al., 2004). In addition, AVO and the University of Alaska Fairbanks (UAF) monitor data from the Geostationary Operational Environmental Satellites (GOES) sensor, which collects thermal infrared (TIR) data with an average pixel size of 4km acquired every 15 minutes, the MODIS sensor with a 1 km TIR pixel size acquired every 4 to 6 hours, and the AVHRR sensor, with 1 km TIR pixel size acquired every 15 minutes to 6 hours.

Due to the large pixel size of these sensors, smaller and weaker thermal anomalies are not detected by these sensors. Therefore, subtle changes in thermal flux, such as what is commonly produced in the initial stages of precursory activity, or spatially small thermal features, such as the appearance of new fumaroles at the summit, commonly go undetected. In some cases, however, seemingly random and isolated peaks in thermal activity are detected months

to weeks before the onset of an eruption. These peaks in thermal output have been observed at Kliuchevskoi. Dehn et al., (2000) proposed these are likely the result of strombolian activity, suggesting that a large sudden increase in thermal energy is produced from fresh material expelled during a strombolian eruption. The material then rapidly cools, resulting in a rapid decrease in thermal output. Therefore, examining changes in thermal activity with a sensor unable to detect lower levels of thermal output results in these singular and seemingly isolated spikes being the only indication of an eruption. In order to capture the entire thermal flux record related to the many styles of subtle thermal precursory activity, a sensor with a higher-spatial resolution and better radiometric accuracy is required.

3.1.2. ASTER

The ASTER sensor is one of the five instruments on the National Aeronautics and Space Administration (NASA) Terra satellite, which was launched in December 1999. ASTER has 15m per pixel spatial resolution with three wavelength channels in the visible/near infrared (VNIR) and 90m per pixel spatial resolution with five wavelength channels in the TIR. With this high spatial resolution and a 60 km swath width, the temporal resolution is limited to 1-5 days at higher latitudes and 16 days at the equator (Yamaguchi et al., 1998; Ramsey and Dehn, 2004). The ASTER TIR sensor has a modeled noise equivalent delta temperature (NEΔT) of between 0.15-0.3°C, allowing accurate temperatures to be derived following atmospheric correction and temperature/emissivity separation. (Gillespie et al., 1998). Another unique aspect of ASTER is that it is scheduled daily, which affects the amount of coverage acquired and later processed. This schedule is created by individual user requests, global mapping campaigns, and emergency

requests for acquisitions (Yamaguchi et al., 1998). In late 2006 the ASTER Urgent Request Protocol (URP) was implemented, which allows an automatic request for ASTER data to be triggered by the detection of thermal anomalies from an array of low spatial resolution sensors (Ramsey, 2015). For example, whenever the AVHRR senor detects a volcano related thermal anomaly via the AVO monitoring program currently in place, the URP system is triggered and an ASTER observation is scheduled for the next available overpass (Ramsey and Dehn, 2004; Duda et al., 2009; Ramsey et al., 2004). Whereas this system does not provide real-time data, it does expedite the ASTER scheduling/acquisition/processing pathway, providing data to users as quickly as possible (Carter et al., 2008; Ramsey, 2015). This increase in temporal resolution of ASTER data has improved the sensors efficiency to capture thermal flux data over given time span. That, combined with the moderately high spatial and accurate radiometric resolution of the ASTER TIR array, makes the data more sensitive to thermal flux from these smaller anomalies, thus improving the detection of thermal precursory activity prior to an eruption.

3.1.3. Data Hybridization

The ASTER, AVHRR and MODIS instruments have strengths and weaknesses that impact the analysis of thermal infrared data for precursory activity. The high spatial resolution of ASTER allows detection of subtle changes in low-grade thermal energy output and also produces a more detailed thermal image of the surface (Figure 3-2A). The high temporal resolution of both the AVHRR and MODIS instruments greatly improve the ability to capture events occurring on shorter time scales. Both MODIS and AVHRR data are less useful for differentiating background temperatures unaffected by volcanogenic activity from those associated with thermal anomalies

(Figure 3-2B and 2C). However, valuable information can be extracted from the combined datasets of all these instruments. The presence of detectable thermal anomalies in the AVHRR and MODIS data are the result of brief large outputs of thermal energy, which have been interpreted to be associated with strombolian eruptions. Where compared to ASTER data, these strombolian events commonly coincide with variations in the trend of thermal flux at the summit, this correlation plays an important role in understanding precursory mechanisms.

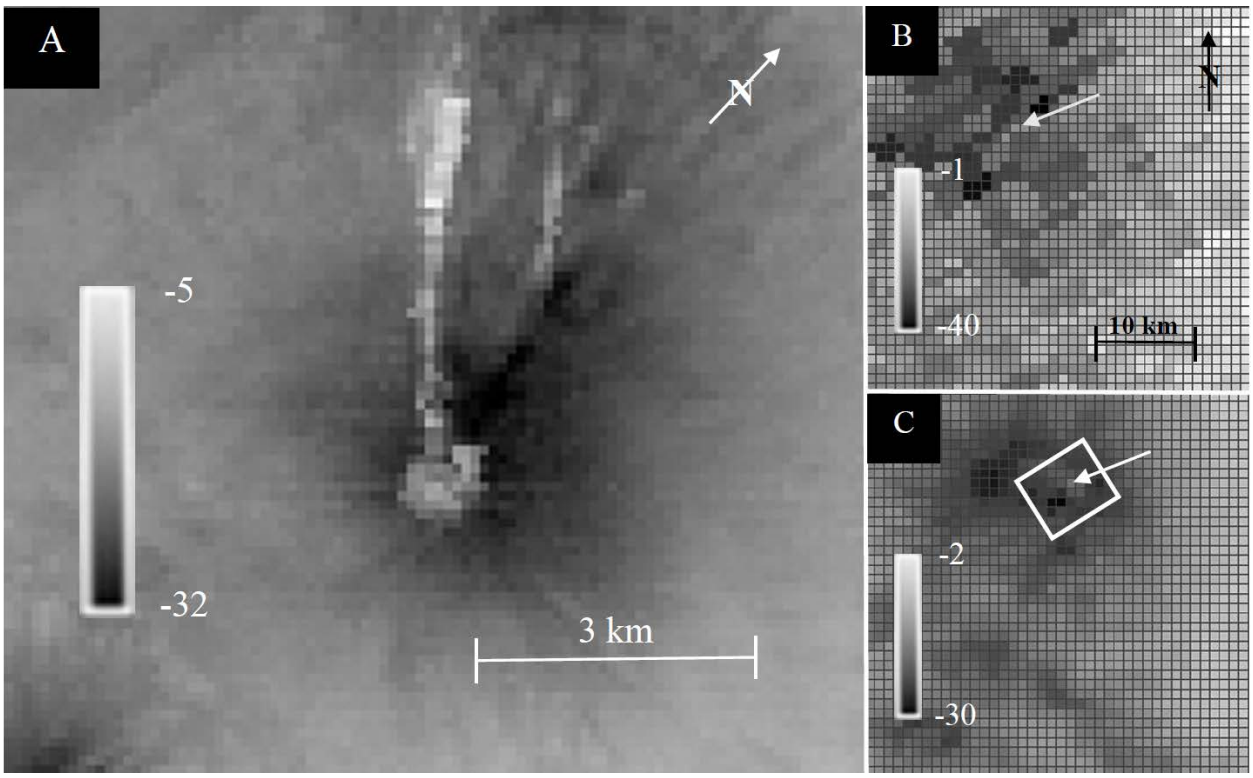

Figure 3-2: Thermal infrared brightness temperature data of Kliuchevskoi volcano with all temperatures in degrees Celsius. (A) ASTER data acquired on April 25, 2009 at 10:51 UTC. (B) MODIS band 21 (3.96 µm) data acquired on April 26, 2009 at 09:53 UTC. (C) AVHRR b and 3 (3.74 µm) data acquired on April 26, 2009 at 09:13 UTC. The images in Both B and C are retrieved from the Okmok algorithm used to monitor volcanoes in the North Pacific and are tiled to better differentiate pixels. The white arrows in images B and C point to Kliuchevskoi volcano, the white box in C signifies the area pictured in A.

3.1.4. Strombolian Eruptions

Strombolian eruptions are commonly observed during periods of activity at Kliuchevskoi (Menyailov, 1975; Rose and Ramsey, 2009; van Manen and Dehn, 2009; Smithsonian Global Volcanism Program, 2013). Past research on these eruptions has shown that they likely originate from the bursting of a gas slug at the magma free surface (Macdonald, 1972; Chouet et al., 1974; Blackburn et al., 1976; Ripepe et al., 1993; Vergnioelle and Brandies, 1996; Patrick et al., 2007). Whereas the exact method of the formation of this gas slug is a point of debate each method shares several common points (Parfitt, 2004). First, the volcanic gases within the magma form bubbles that eventually coalesce into an expanding gas slug (Parfitt and Wilson, 1995; Vergnioelle and Brandeis, 1996). As the gas slug moves up the volcanic conduit, it continues to gain volume and expand from the continued addition of gas (Kirchdorfen, 1999; Chouet et al, 1999). Finally, once the gas slug reaches a shallow depth with a minor amount of over pressure (~0.5-4 bar, Ripepe and Marchetti, 2003) the slug bursts through the magma surface, resulting in an eruption of ballistics and increased output of gas (Blackburn et al., 1976). After the expulsion of the slug, the upward driving mechanism and the additional volume from the gas has been removed. Therefore, the height of the magma in the conduit will drop, which may lead to backfilling of the conduit from the slumping of inner crater walls (Calvari and Pinkerton, 2004) or from the rollback of explosion ejecta into the vent (Booth and Walker, 1973; Self et al., 1974; Francis, 1993). This backfill increases the overpressure and can lead to additional eruptions which, clear the vent produce ballistics and ash (Patrick et al., 2007).

3.1.5. Kliuchevskoi Eruptions of Interest

Of the 29 active volcanoes in Kamchatka, Kliuchevskoi is one of the most active, producing an average of 6.0×10^7 tons of material per year (Fedotov et al., 1987; Fedotov and Masurenkov, 1991; Ozerov et al., 1997). In the past 21 years flank, summit, and paroxysmal type eruptions have all been recorded (Fedotov and Masurenkov, 1991; Rose and Ramsey, 2009). Sixteen flank eruptions have occurred since 1907 and the last paroxysmal summit eruption was in 1994. Eruptions from the summit crater are the dominant type, occurring every 1-2 years in the past century (Fedotov and Masurenkov, 1991; Smithsonian Global Volcanism Program, 2013). These eruptions vary from strombolian to plinian in scale and have a longer duration than flank eruptions (Gushchenko, 1979; Rose and Ramsey, 2009; Smithsonian Global Volcanism Program, 2013).

In 2005, 2007 and 2009 Kliuchevskoi produced eruptions large enough to be classified as a Volcanic Explosive Index (VEI) of 2, and in the case of both the 2005 and 2009 eruptions, a VEI 1 eruption was believed to have reached its conclusion 6-8 months before the VEI 2 eruption of interest (Smithsonian Global Volcanism Program, 2013). In 2007, a relatively long period of time of assumed inactivity passed before the onset of the eruption. Seemingly random and isolated thermal anomalies (e.g., Dehn et al., 2000) were seen in the AVHRR data before each of these eruptions. However, without higher spatial resolution data, these anomalies were not linked to the onset of a larger eruption. The onset of each eruption was not predicted for a period longer than days to a week before according to analysis of the AVO daily reports and Dehn and Harris, (2015). Although this does allow for a warning to be issued before large eruptions, mitigation of potential hazards beyond evacuation or avoidance become extremely difficult in this time scale.

This study therefore seeks to improve this time by improving our understanding of the precursory period and the activity therein by incorporating ASTER data into the existing satellite-based monitoring dataset. A more complete understanding of the eruptive precursors should allow the warning time to an eruption onset to be greatly extended, thus lowering the associated risks.

3.2. Methods

3.2.1. Data Collection

All data acquired by orbital instruments during the precursory time periods for the Kluichevskoi eruptions were initially inspected using the US Geological Survey (USGS) Global visualizer viewer (Glovis) and University of Alaska Fairbanks (UAF) Volcanic Ash Detection, Avoidance, and Preparedness for Transportation (V-ADAPT, Inc.) program. All available cloud-free scenes over the summit were selected. In the case of the AVHRR and MODIS data, only images where a summit thermal anomaly could be distinguished from background were included.

3.2.2. Period of Analysis

The thermal activity produced at the summit of Kliuchevskoi prior to the large eruptions in 2005, 2007, and 2009 was analyzed in detail. The data were constrained to a time period in which thermal activity can be directly related to the precursory activity of these eruptions. This time period in both the 2005 and 2009 events occurs between the inactivity preceding the VEI class 1 eruption and the onset of the VEI class 2 eruption. This chosen time period precludes thermal anomalies related to prior eruptive phases from being classified as precursory activity. This time

period extends from September 15, 2004 to January 20, 2005 and from April 16, 2009 to August 1, 2009 (Smithsonian Global Volcanism Program, 2013) respectively for the 2005 and 2009 events. The precursory period of the 2007 eruptive phase is different than the other two eruptions. In 2007, there was no VEI 1 eruption 4-6 months before the onset eruption on February 15, 2007. The prior eruptive cycle was classified as inactive on April 7, 2005 (Smithsonian Global Volcanism Program, 2013), resulting in an inactive period of approximately 21 months between eruptions. This presented a unique opportunity to greatly extend the period of precursory analysis, which was chosen to be one year to quantify the inactive phase of Kliuchevskoi as well as the onset of precursory activity. Within this one-year period, enough data were captured to positively define all 3 phases of precursory activity.

3.2.3. Data Processing

ASTER radiance-at-sensor data were atmospherically corrected to surface radiance using the standard Level 2 (AST_09T) product (Thome et al., 1998; Abrams, 2000). Emissivity and brightness temperature were separated for each pixel using the emissivity normalization approach (Gillespie, 1985; Realmuto, 1990; Reath and Ramsey, 2013). This process relates radiance to emissivity and temperature using the plank equation and produces a unique emissivity image for each of the five ASTER TIR channels available and one brightness temperature image for the entire scene. AVHRR and MODIS infrared data were converted directly into radiant temperature in near real time using the Okmok algorithm and archived by UAF (Dean et al., 1998; Dehn et al., 2000; Bailey et al., 2010). Only AVHRR band 3 (3.74μm) data (3B in AVHRR-15 and later) and MODIS band 21 (3.96μm) data were included in this analysis. These bands correspond to the

wavelength region most commonly used to detect high heat sources, such as volcanoes and fires (Dehn et al., 2000; Ramsey and Dehn, 2004; Pergola et al.,2004).

A background temperature is first calculated for each brightness temperature image. In the ASTER data the background temperature is calculated by averaging the temperatures from an 11x11 pixel ($9.8x10^5$ m^2) region of interest (ROI) within 1 km and at approximately the same elevation as the observed thermal anomaly. The area of the ROI was chosen specifically to approximate the size of an AVHRR and MODIS TIR pixel and capture any smaller-scale pixel to pixel temperature variations. These ROIs are geolocated at the same latitude and longitude in every ASTER scene and confirmed free of thermally-anomalous pixels and clouds. Background temperatures for AVHRR data are determined by calculating the temperature of a pixel adjacent to the thermally anomalous area with no perceived temperature artifacts, such as (1) pixel bleeding, from an adjacent high-temperature anomaly (Dehn et al., 2002; Harris et al., 1997b, 1999); (2) a thermal rebounding artifact ("recovery pixel") created by miscalculating the radiance value of the pixel directly adjacent to a thermally-elevated pixel; (3) cosmic ray hits; (4) station mask transmission errors; and/or (5) clouds. Due to the multitude of factors affecting the AVHRR data and the abundance of AVHRR scenes analyzed in this process, finding a single geo-located pixel to be used as the background value for every scene was not possible.

The specific criteria needed to classify a pixel as containing a thermal anomaly is discussed in detail by Pieri and Abrams (2005), who refer to thermal anomalies as pixels containing elevated thermal activity. This elevated activity increases the amount of radiant energy, which is directly related to an increase in brightness temperature from that pixel. This does not affect the background pixels, if chosen correctly. The radiometric accuracy for ASTER brightness

temperatures using the emissivity normalization approach is ±1-2°C (Thome et al., 1998) and ±2.5°C for AVHRR, both assuming a natural environment with atmospheric integrated water vapor (Goita and Royer, 1997). Therefore, anything less than 2°C above the derived background temperature would be indistinguishable from noise and not distinguished in this analysis. A value of 2°C above the background temperature was therefore chosen as the threshold, above which a pixel is considered thermally anomalous. The distribution of anomaly temperatures in the ASTER data are determined by including the entire summit area affected by increased thermal output and determining the pixel with the highest temperature in this area. The reasoning for using the pixel with the highest temperature rather than the average temperature of the region is twofold. First, the area affected by the thermal anomaly does not remain constant. Analyzing the total area would introduce fluctuations in both total area and derived temperature to determine the total amount of heat produced. However, by only examining the hottest pixel, the area remains constant and only the most intense thermal output is tracked. Second, vent temperature fluctuations are more extreme than those of the entire thermal anomaly. In most cases, the vent is captured by one or two of the hottest pixels. This guarantees that only heat variations from the vent are used.

Thermal anomalies in the AVHRR ad MODIS data were typically dominated by one pixel, once again producing the highest temperature. This pixel can be related to the rapid thermal spikes recorded at the summit of Kliuchevskoi. MODIS and AVHRR captures data at a higher temporal resolution than ASTER and can therefore be used to increase the number of measured temperatures in the temporal dataset. The higher temporal resolution in the AVHRR and MODIS datasets also increases the probability of cloud-free scenes and capturing short-lived/high

thermal output events, such as a strombolian eruption. However, in this study, confirmed thermal anomalies on the summit of Kliuchevskoi were only identified by MODIS within a week of the eruption onset. During this period of eruptive activity AVHRR data also produced abundant results and therefore the inclusion of MODIS data was deemed unnecessary.

The background temperatures derived in each of these scenes is subtracted from the thermal anomaly temperature in order to calculate the thermal anomaly temperature above background (ΔT_{ta}). The only factors that would change the derived background temperatures are environmental (e.g., time of day, season, local slopes, etc.) rather than volcanogenic. Therefore, the process of subtracting the background temperature also allows for the removal of these artifacts. These ΔT_{ta} data are plotted against time for the analysis period to determine the presence of any volcanic precursors. The plots are analyzed for patterns that lead to the better understanding of precursory processes, which in turn can indicate the possibility of an upcoming eruption. Although AVHRR data are connected in these plots, this is only to improve the graphic representation of the progression of points through time. Any period longer than six hours between AVHRR-derived temperatures is likely the result of no discernible thermal anomaly. In some cases, patterns that are related to events require further analysis. Where this occurred, combined analysis of the ASTER and AVHRR data spanning the event period proved useful to understand the processes responsible for these patterns.

In cases that required further analysis, the brightness temperature data are compared to the next available clear ASTER scene to examine the smaller-scale spatial variations occurring at the summit. These analyses are both qualitative (e.g., observing the locations of the hottest pixels) and quantitative (e.g., using the ROI approach to find the total area and average

temperatures). It is likely that, in some cases, AVHRR recorded a thermal anomaly smaller than its pixel size. In order to produce an accurate reading of the average temperature of the thermal anomaly, the integrated pixel equation (Rothery et al., 1988) was applied to the AVHRR pixels affected by the thermal anomaly:

$$T_{pixel} = T_{hot}\left(\frac{A_{hot}}{A_{pixel}}\right) + T_{cold}\left(\frac{A_{pixel} - A_{hot}}{A_{pixel}}\right) \quad (1)$$

In this equation: T_{pixel} = original pixel(s) temperature, T_{hot} = temperature of hot feature, T_{cold} = temperature of cool feature, A_{hot} = area of hot feature, and A_{pixel} = total area cover by all pixel(s) included in equation. The equation is solved for T_{hot}, or the temperature of the hot feature within the pixel of interest. This approach is typically not required for the higher spatial resolution of the ASTER data as it is assumed the hot fraction fills most/all of the ASTER TIR pixel. Therefore ASTER data can provide an area for the hot feature or A_{hot} and T_{cold}, or the background temperature is gained from the temperature of the background AVHRR pixel.

3.2.4. Analysis of the 3 Eruptive Cycles

Each eruptive cycle provides a unique insight into what is occurring during the precursory phase and how the data can be interpreted. It is important to note that when these two datasets are analyzed, two very different features are being represented. Due to the small area of the summit vent (several hundred meters maximum), flux related to changes in thermal output is only observed with a high spatial resolution sensor, such as ASTER. AVHRR and MODIS data cannot detect low-level thermal flux, instead recording short-lived/high temperature events. As mentioned, these measurements are not continuous. Each peak in AVHRR thermal output likely

corresponds to a single strombolian event but only one temperature increase is recorded due to the rapid cooling following the eruption. In order to properly analyze these datasets, the data from each sensor must be considered independently and the differences between ASTER and AVHRR considered carefully.

The 2009 eruptive cycle contains the most complete dataset and is therefore analyzed first using the results as the control of a typical four month period before an eruption. In this dataset, peaks in the AVHRR-derived temperature data were further analyzed for strombolian activity. The added time period of the 2007 eruption was examined in order to extend the transition from inactivity to precursory activity. It was also used to determine what processes may have caused this eruption to escalate to a VEI 2 eruption without evidence of an initial VEI 1 phase seen in the other eruptions. The 2005 eruption data had the least amount of available data as the eruption occurred prior to the ASTER URP system being fully implemented. These data were examined to demonstrate how the URP system improved the understanding of volcanic processes and how volcanic precursors can be derived from even a limited amount of ASTER scenes.

3.3. Results

3.3.1. 2009 Eruptive Cycle

Analysis of the precursory data from the 2009 eruptive cycle revealed several important features (Figure 3-3). First, the spike in thermal output recorded in AVHRR data on May 21, 2009 19:32 UTC was analyzed to determine the possibility that it was the result of strombolian activity. The

ASTER data acquired 11 days prior (May 10, 2009 00:32 UTC) and five days after (May 26, 2009 00:33 UTC) this event were analyzed. The difference in thermal activity is apparent on and around the summit (Figure 3-4). In the center of Figure 3-4A is the summit of Kliuchevskoi where a small cooling flow can be observed on the northwest (NW) flank produced during the previous VEI 1 eruption. No other thermal anomalies are observed. Later, a large thermally-elevated area on the southeast (SE) flank of the edifice is observed and the flow seen in the previous image is larger and more pronounced (Figure 3-4B). The maximum pixel temperature on the SE flank has increased 33°C from the previous image and is an average of 17°C above the background temperature. Both of these scenes are captured within one minute of each other 16 days apart, thereby eliminating any possibility of environmentally-related thermal artifacts in the derived background temperature. The increase in both thermal output and areal extent of thermally-elevated pixels can only be the result of the deposition of volcanic material on the surface. The thermally integrated pixel equation (1) was used to determine whether the activity was intense enough to produce the observed temperature spike in the AVHRR data acquired on May 21, 2009 19:32 UTC. The result equates to an average deposition temperature of 46.4°C above the background. The deposit also produced enough material to be detected as a thermal anomaly 17°C above background in the ASTER scene (Figure 3-4B). Additionally, a majority of the heat from this event had dissipated by the next clear AVHRR acquisition, approximately 1.5 days later on May 27, 2009 20:02 UTC. By this time, the average temperature of deposit had decreased to 5.9°C above background temperatures. These temperatures suggest relatively rapid cooling after the deposit was emplaced. This would result from a thin-mantling deposit similar to the spatter common following strombolian eruptions. It is important to note here that although these flows

produce thermally anomalies, they are not located at the summit and therefore are not directly related to longer-term thermal output from the system.

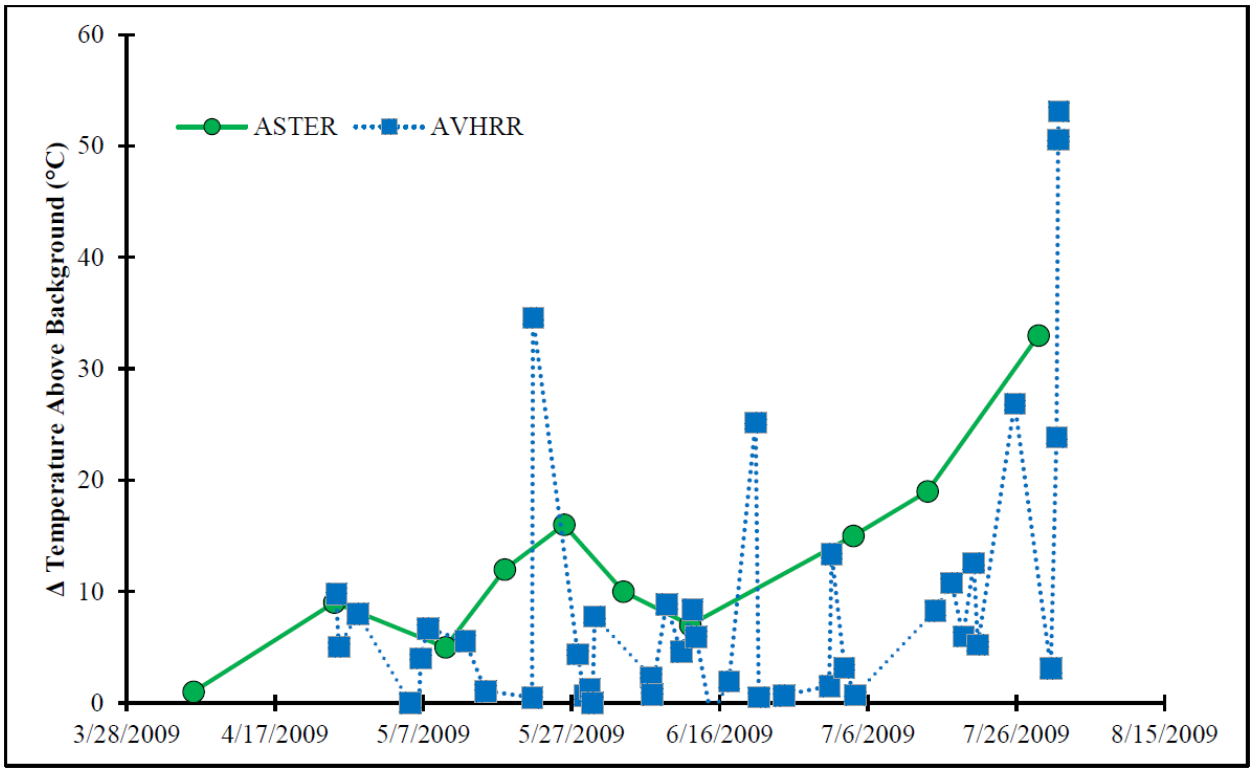

Figure 3-3: Temperature versus time plot of the 2009 activity at Kliuchevskoi volcano with date written in US format. The temperature difference represents the elevated crater temperature minus the background temperature. Data were gathered from April 25, 2009 until the onset of the eruption (August 1, 2009).

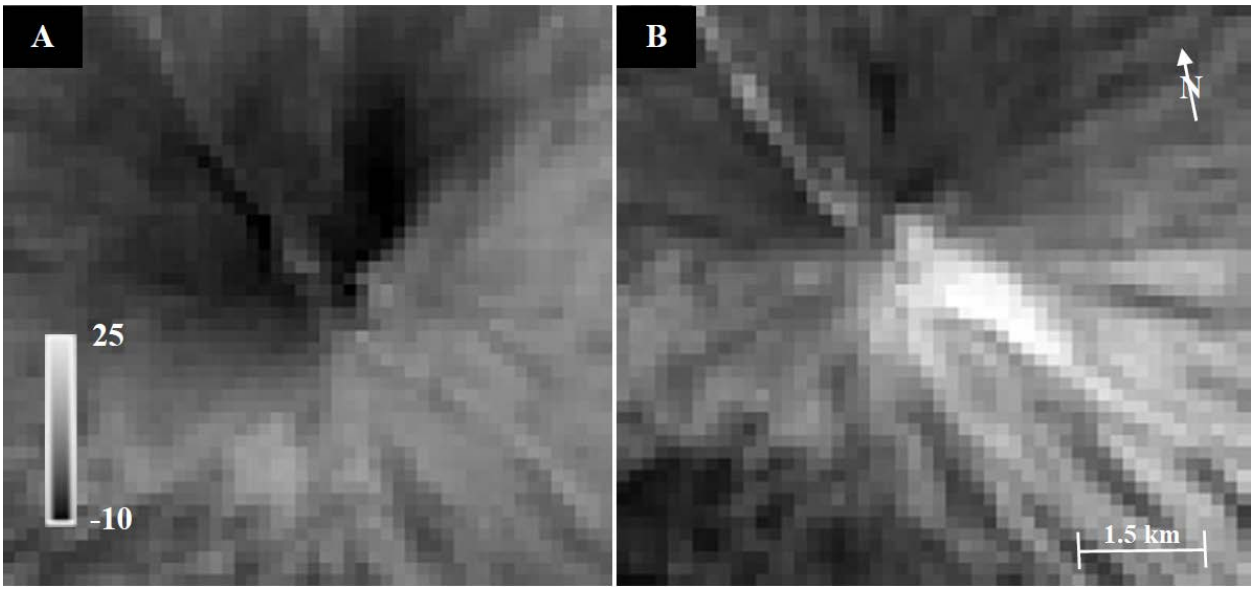

Figure 3-4: ASTER thermal IR temperature data of Kliuchevskoi Volcano collected on May 10, 2009 at 00:32 UTC (A) and May 26, 2009 at 00:33 UTC (B). A strombolian eruption occurred on May 21, 2009 and a region of elevated temperatures on the southeast flank is observed. This is caused by the still-cooling debris from these strombolian eruption. The temperature range is constant in both images and is in °C above background temperatures.

With this understanding of the AVHRR temperature data, the ΔT_{ta} versus time can be examined further (Figure 3-3). Over the entire study period, the ASTER data records the total thermal flux emanating from the summit, which results in an overall trend of an increase in temperature until the onset of the VEI 2 eruption. The AVHRR data are more sporadic with no observable trend until July 25, 2009, where the temperatures begin to steadily increase. However, analyzing these two datasets together reveals more information about the possible events leading up to the eruption. Importantly, fluctuations between short-term increases and decreases in ASTER-derived temperature coincide with increases in both intensity and the rate of thermal spikes in AVHRR data. Assuming these spikes are the result of strombolian eruptions, a link between the occurrence of these eruptions and the changes in thermal output can be observed (Figure 3-3). From June 12, 2009 until the onset of the eruption on July 31, 2009 a

consistent and rapid increase in thermal output is observed in the ASTER data, regardless of the trend in the AVHRR data. This increase in thermal output reaches levels high enough to be finally be detected in both AVHRR and ASTER data on July 25, 2009. At this point the precursory activity was detected by the AVO monitoring system. Six days before the eruption, AVO staff were able to confirm that activity at Kliuchevskoi had increased. However, the activity level was not raised from green to yellow until August 1, 2009 after a tephra plume was detected.

3.3.2. 2007 Eruptive Cycle

The 2007 precursory data (Figure 3-5) produced similar results to the 2009 analysis, with several important distinctions. First, there is a larger time period between eruptions before this eruptive phase, which allows the precursory data to be analyzed over a truly inactive period. During this phase the heat from the vents of the summit maintained a consistent temperature of approximately 10°C above background for a period of eight months, lasting from January 3, 2006 to August 7, 2006 (Figure 3-5). This inactive period is hereby referred to as Phase I. The end of Phase I is marked by a repeat of the variable thermal output observed in the 2009 precursor data. This variable thermal output phase (Phase II) lasts for approximately 4 months, from August 7, 2006 until December 22, 2006. The final phase (Phase III) last for approximately two months, from December 22, 2006 to February 15, 2007, and is once again characterized by an increase in thermal output at a relatively consistent rate leading up to the onset of eruption. However, in this case, Phase III does not increase as consistently as found in the 2009 data. From January 16-29, 2007 there is a 2-week period where the thermal output is diminished in both ASTER and

AVHRR data. With this exception, the precursory activity of Phase II and III behaves nearly identically to behavior seen prior to the 2009 eruption. However, in this eruptive cycle Phase II lasts 2 months longer than in 2009, which is likely the result of precursory activity being recorded and analyzed over a longer time period. Phase II transitioned to Phase III 56 days before the onset of eruption in 2007, this same period lasted 49 days in 2009.

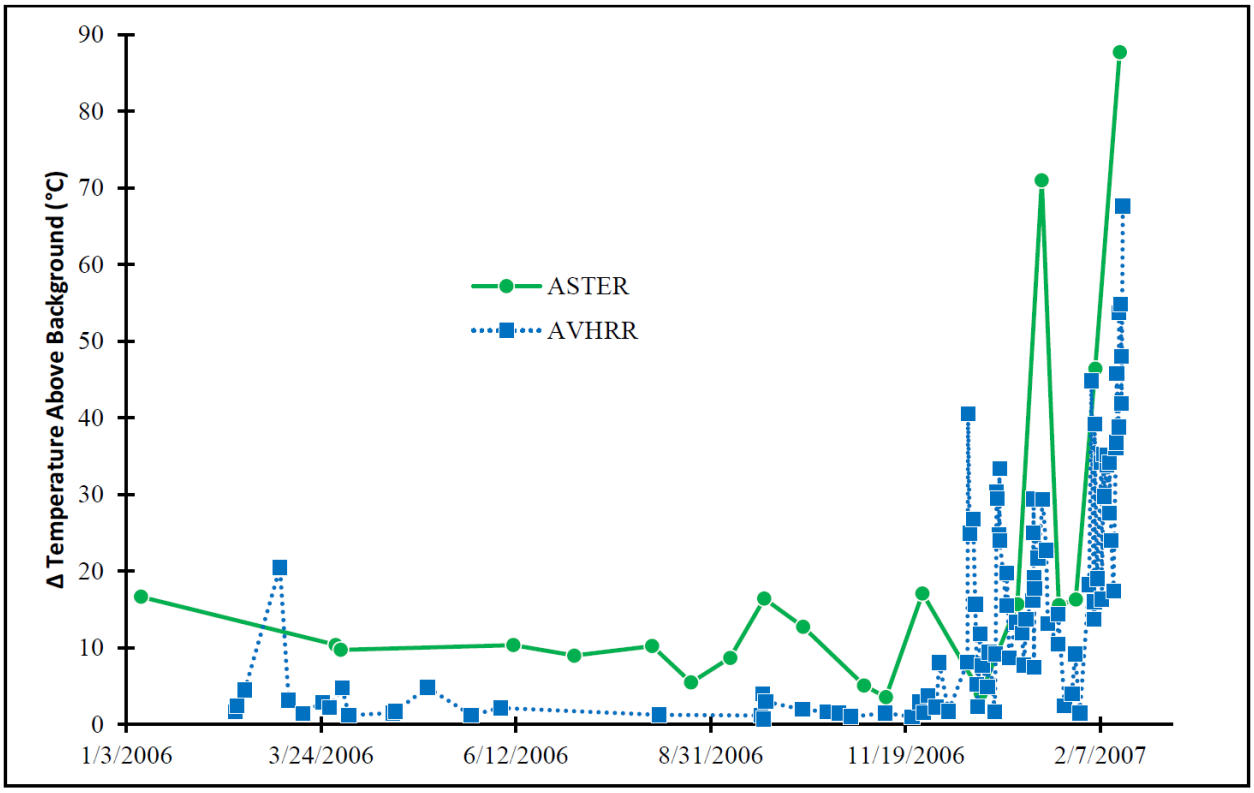

Figure 3-5: Temperature change versus time plot with date written in US format of the period one year before the VEI classification 2 eruption that occurred February 15, 2007.

Phase III contains one large fluctuation in thermal output (Figure 3-5). In order to further analyze the cause of this rapid drop in thermal activity, the ASTER TIR scenes acquired directly before the event on January 14, 2007, during the event on January 21, 2007, and directly after the decrease in heat on February 15, 2007 were analyzed in more detail (Figure 3-6). Observation reveal that

the data captured before the thermal decrease (Figure 3-6A) show a large amount of heat being produced in four centrally located pixels with a maximum temperature of 38°C and an average temperature of 5°C above the background. The total area of the thermal anomaly at the crater is 0.75 km^2. In the second time frame (Figure 3-6B) the thermal anomaly expanded to 0.79 km^2, and the average temperature decreased to 4°C above background. In the third time frame (Figure 3-6C) the maximum temperature again increases to 41°C, measured from several pixels in the same location as those observed in the January 14, 2007 scene (Figure 3-6A). The thermal anomaly in Figure 6C has also decreased in area to 0.67 km^2 whereas the average temperature has risen to 6°C above background. Immediately after this large decrease in thermal output, temperatures at the summit begin to increase rapidly and within ten days a VEI 2 eruption begins.

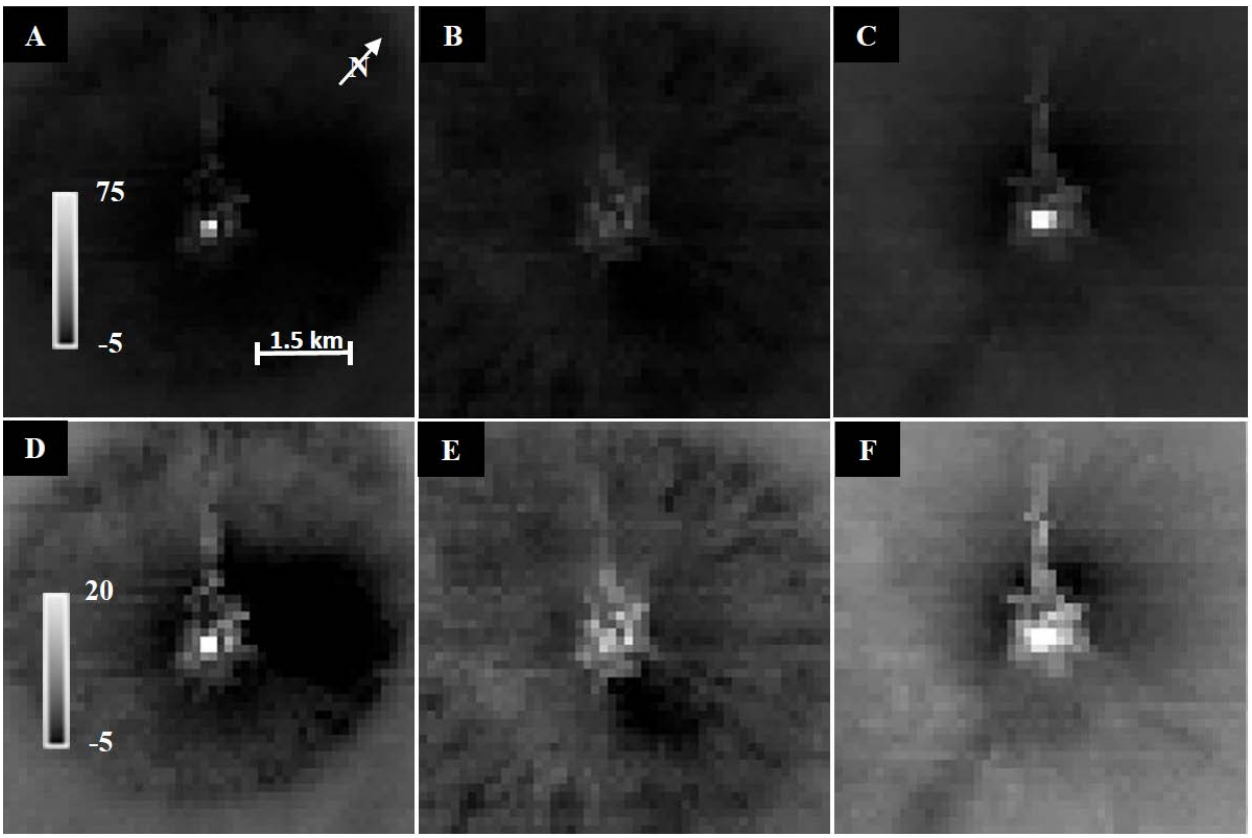

Figure 3-6: ASTER images centered on Kliuchevskoi volcano crater captured (A, D) January 14, 2007 at 10:50 UTC, (B, E) January 21, 2007 at 10:56 UTC, and (C, F) February 15, 2007 at 10:50 UTC. Two different temperature ranges, (A-C) -5 to 75°C and (D-F) -5 to -20°C above background temperatures are used.

3.3.3. 2005 Eruptive Cycle

The precursory activity before both the 2009 and 2005 eruptions are generally similar. In both cases a VEI 1 eruption occurred at least 5 months prior to the subsequent VEI 2 eruption. AVHRR thermal spikes appear to occur at similar intervals with slightly different intensities. The significant data difference between the 2005 and 2009 eruptive cycles is the number of ASTER scenes available (Figure 3-7). Increased ASTER data frequency occurred directly after the implementation of the ASTER URP program, which went into place in late 2005 (Duda et al., 2009; Carter and Ramsey, 2010; Ramsey, 2015). The benefits of this program are evident and provide

insights into the benefits of future higher spatial/higher temporal resolution instruments. Whereas the number of clear scenes recorded during 2009 allowed for a clear interpretation of the activity leading to the eruption, only three clear scenes were acquired during in the precursory period in 2005 (Figure 3-7). It is therefore difficult to extract any meaningful trends with so few data points. However, visually examining the three ASTER scenes does provide some valuable clues (Figure 3-8). In the first scene (Figure 3-8A) a single pixel within the summit thermal anomaly produced an elevated thermal output compared to the surrounding pixels. In the second scene (Figure 3-8B) this pixel no longer has an elevated temperature and all pixels within the anomaly have a relatively uniform temperature. The third scene (Figure 3-8C) was acquired less than a week before the onset of the larger eruption. In this scene, a single pixel of elevated temperature relative to background can once again be seen in the crater. The location of that pixel has changed, however. Whereas these data to do not provide the same level of quantifiable data as the 2007 and 2009 data series, thermal variability can still be observed at the summit.

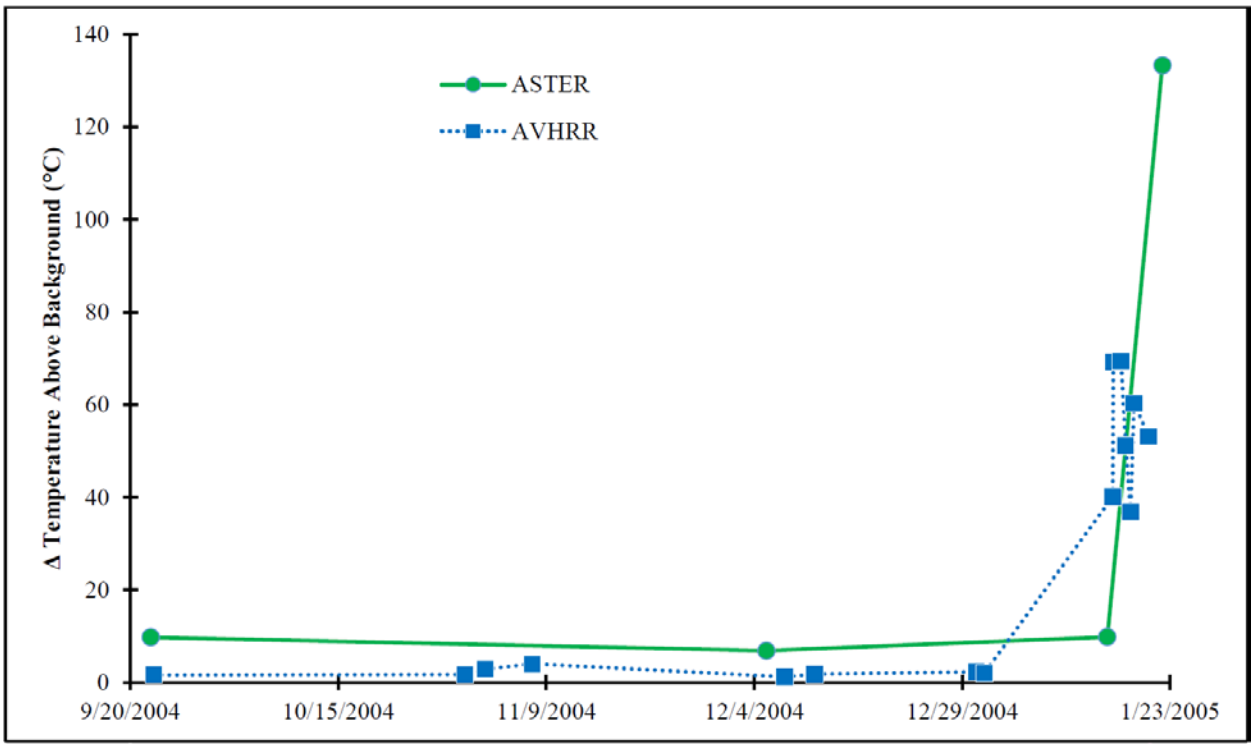

Figure 3-7: Temperature change versus time plot with dates written in US format of the period covering the period between September 15, 2004 VEI classification 1 eruption and the February 20, 2005 VEI classification 2 eruption.

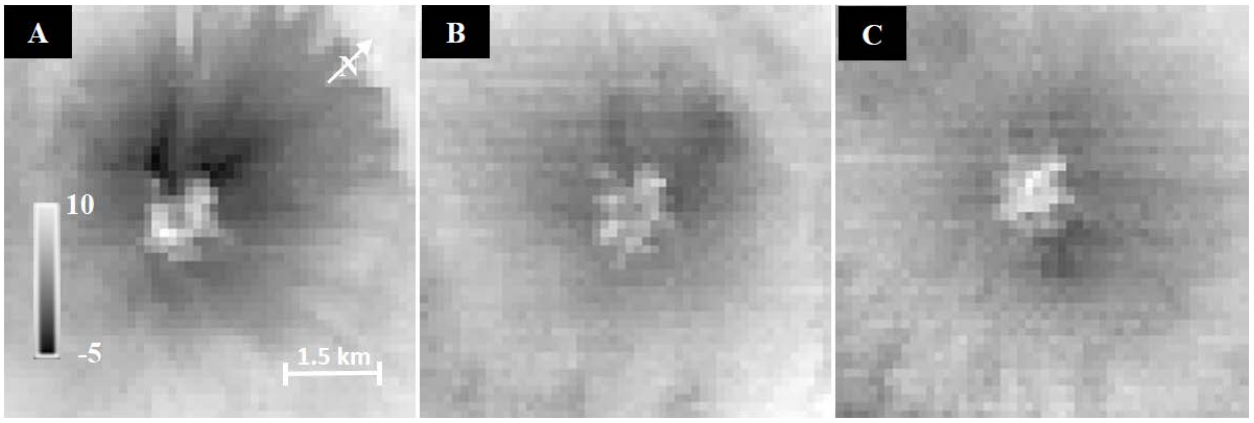

Figure 3-8: ASTER image data centered on Kliuchevskoi volcano crater captured (A) September 2, 2004 at 10:49 UTC, (B) December 5, 2004 at 11:01 UTC, and (C) January 15, 2005 at 10:55 UTC. Temperature ranges are constant for all 3 images and are in °C above background.

3.4. Discussion

3.4.1. Precursory Phases

Fluctuations in the thermal output over time (Phase II) prior to the onset of eruption were observed in each of the case studies. Whereas the lack of ASTER data before the 2005 eruption prevented these fluctuations from being as clearly tracked as the 2007 and 2009 eruptions, examination of the individual ASTER scenes suggest these fluctuations were still occurring. Furthermore, a pattern can be distinguished in the precursory activity of all three eruptions. During the restive phase (Phase I) there is a consistent, low-level thermal output from the summit crater only detectable with ASTER data. These periods last from months to years. The ASTER data gathered during the 2007 precursory period showed thermal variations were present approximately 6 months prior to the eruption (Phase II).

Following this phase, the thermal output from the summit begins to increase as gas begins to build in the conduit and a gas slug is formed. The gas slug expands with time and rises, driving the magma higher in the conduit. This results in an increase in thermal output and a larger thermal anomaly at the summit. After the strombolian eruption, this gas slug becomes depleted. As a result the height of the magma in the conduit and the thermal output both decrease. This cycle appears to repeat periodically throughout Phase II in some cases. In others, when this drop in magma height occurs, backfilling of the conduit from slumping of the inner crater walls or the rollback of explosive ejecta, produces a transition from a decreasing thermal output to an increasing one. This backfill is cleared from the conduit once the gas slug has been reestablished in the conduit. Patrick et al. (2007) describes that these eruptions should be accompanied by a small ash cloud, which may be occurring and visible at the site. However, such a cloud was not

large enough to be detected by either ASTER or AVHRR. Once this backfill has been cleared, the gas slug and magma levels once again rise in the conduit and the cycle repeats (twice in 2009 and 2.5 times in the 2007).

After several sequences of Phase II activity, the volcanic activity transitions to Phase III. Here, thermal output consistently increases until the onset of eruption. The ASTER data suggests Phase III begins approximately 2.5 months prior to the onset of the large, ash-producing VEI 2 eruption in 2009 and approximately 2 months before the onset in 2007. In the 2007 data, increased temporal resolution and numerous clear scenes at the time of this transition from Phase II to Phase III allowed the ASTER and AVHRR data to be directly compared. During this transition in ASTER data, a large strombolian eruption was recorded in the AVHRR data. This eruption most likely cleared and/or expanded the conduit allowing for a decrease in the confining (or lithostatic/overburden) pressure on the magma chamber, causing the ascent of magma toward the surface. As the magma rose in the conduit, thermal output increased and the driving mechanism controlling magma height shifts from the gas slug to consistently rising magma in the conduit. In prior studies, similar Phase III behavior has been noted by Pieri and Abrams (2005) in their observations of the precursory activity at Chikurachki volcano in 2003 using ASTER data.

These three phases produce distinctly different thermal variability over time due directly to the differing precursory activity. Examining the ASTER time series for a particular phase allows the current hazard state to be assessed and the approximate time before a larger eruption to be determined. Evaluating the transition from a constant thermal output (Phase I) and a variable thermal output (Phase II) can be accomplished easily given a large enough dataset. Once the ASTER-derived temperature at the crater varies more than 2°C per week, activity transitions to

Phase II. However, the transition between Phase II and Phase III is more subtle. In the 2007 data, a large thermal spike in the AVHRR data was observed at the same time the ASTER data transitioned to a consistent increase in thermal output. This spike is greater than any previously recorded in the cycle, suggesting a larger strombolian eruption. This eruption likely cleared and expanded the volcanic conduit reducing the confining pressure on the magma chamber, allowing magma to ascend and resulting in a consistent increase in thermal output. Because this larger strombolian eruption initiates this magma driven ascent, the indicator that signifies the transition to Phase III is the large spike in thermal output in the AVHRR data, followed by a steady increase in thermal output in the ASTER data, which lasts longer than 21 days. Whereas this transition is observable in the 2007 ASTER data due to the increased number of available scenes, the 2009 data presents a challenge for determining this transition to Phase III. From June 12 to July 4, 2009 there were no cloud-free ASTER scenes acquired. Solely based on the 2009 ASTER data (Figure 3) one would conclude that the precursory activity transitions from Phase II to Phase III on 12 June 2009. However, by including the higher temporal resolution AVHRR data, there is a much improved opportunity for capturing a cloud-free scene. For example, a large thermal detection was observed in the AVHRR data on June 20, 2009. The event corresponds with a large strombolian eruption equivalent to the one that indicated the transition to phase III in the 2007 precursory activity. ASTER data cannot confirm this transition point directly; however, it is clear based on the 2009 dataset, that if more clear ASTER data were available in 2007, the large conduit-clearing event on June 20, 2007 would mark the actual transition from Phase II to Phase III. With definitions of these transition points and intensity of thermal activity in each phase, it is

possible to distinguish the precursory activity phase and time before the onset of a larger eruption.

Including ASTER data in the precursory activity timeline allows the period of fluctuations associated with the onset of an eruption to be increased from six days to four months. Within this four month period two distinct phases were identified. Consistent fluctuations in thermal output occur with a minimal rise in the average of thermal output were detected approximately two to four months before the eruption. Approximately 2 months before to the onset of the 2009 eruption, the activity shifts to a consistent increase in thermal output. Similar activity was also observed before both the 2005 and 2007 eruptions; however the consistent increase is less obvious for reasons explained in this study. This distinction in activity occurs as the eruption cycle nears its onset can also be used to improve the accuracy in predicting the time of eruption.

3.4.2. Implementation into Volcano Monitoring

Many geophysical and remote sensing networks are currently used to monitor volcanic activity, including seismic, deformation, hydrology, gas as well as ground-based and orbital remote sensing datasets. The USGS assesses the capability of thermal remote sensing in volcanic monitoring, acknowledging its importance in monitoring increased heat flow that may result from magma ascent (Freymueller et al., 2008). It also mentions that tracking the thermal emission over time could play an important role in understanding volcanic unrest. However, when this report was written, thermal monitoring was confined to low spatial/high temporal resolution orbital data to classify particular types of volcanic activity after an eruption had begun. Including a higher spatial resolution sensor such as ASTER to the existing monitoring system provides a

guideline for Phase II to Phase III activity. These guidelines are: (1) a change of more than 2°C in thermal output at the summit in less than 1 week (Phase II transition); and (2) an sustained increase in thermal output lasting more than 21 days that is preceded by a large spike in thermal output in AVHRR or MODIS data (Phase III transition).

Currently, no quantitative values relating to the time before an eruption or the degree of activity are assigned to the color code levels used to communicate the eruptive state of a volcano. The limitation with these color coded systems is that the distinction between Green (normal conditions), Yellow (unrest), and Orange (heightened unrest with expectation of eruption) is a judgment call by the observatory scientists (Guffanti and Miller, 2013). However, including ASTER data into an already established monitoring system using AVHRR and MODIS data, precursory activity can be classified and quantitative values assigned to each color codes. For example, Phase I would be equivalent to green (normal) activity, Phase II to yellow (advisory), and Phase III to orange (watch). The criteria for the red (warning) level would not change as it signifies the eruption onset (Figure 3-9). The inclusion of these data therefore should provide a quantitative transition to the next color code as well as provide insight into the potential hazards associated with each code as well as a good approximation of the eruption timing.

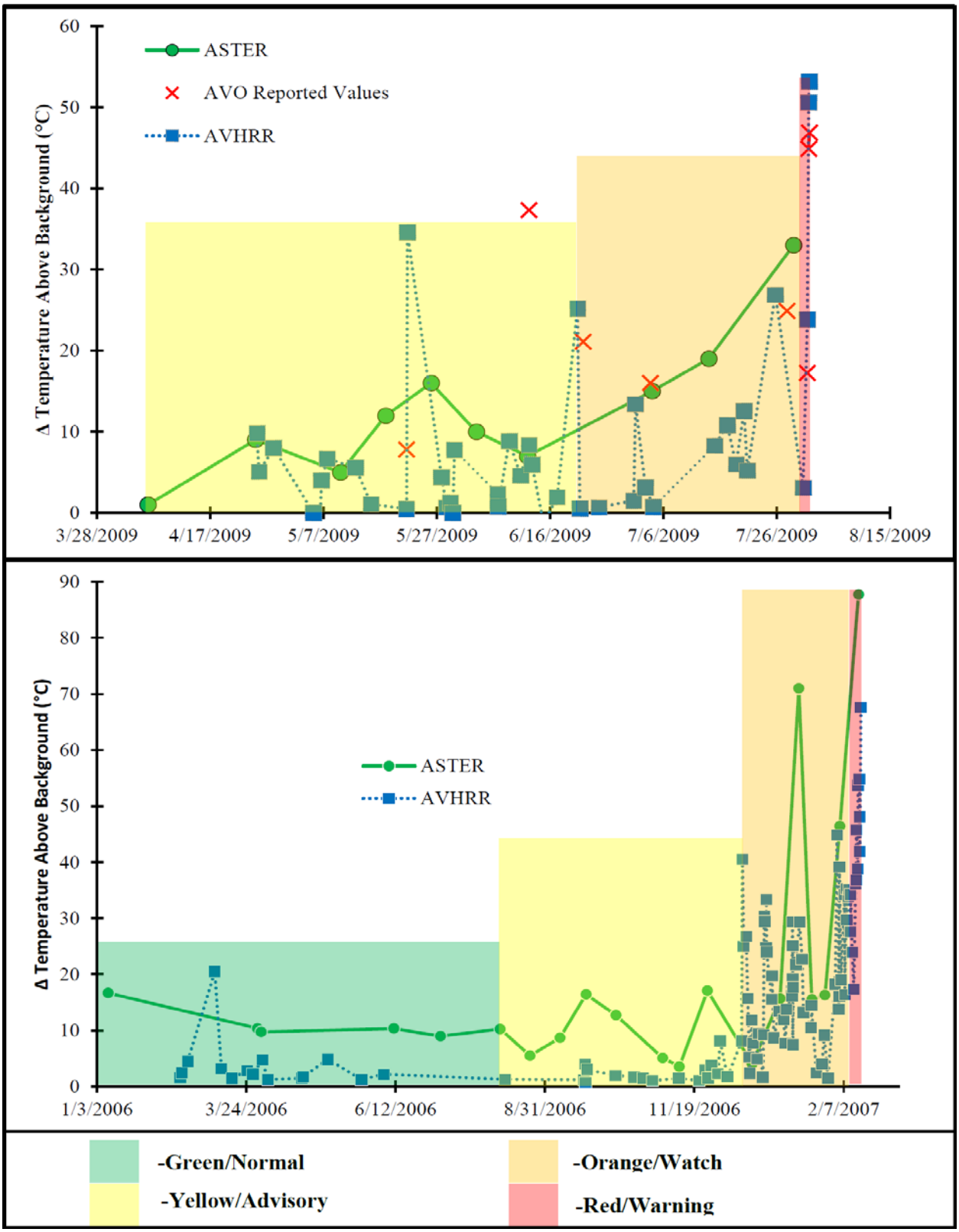

Figure 3-9: Plot of 2009 and 2007 precursory activity including correlating activity levels for each precursory phase.

3.4.3. Phase III Activity in 2007

The precursory activity for the 2007 VEI 2 eruption showed slight differences from the 2005 and 2009 eruptions. In both the 2005 and 2009 eruptions a period of VEI 1 eruptions preceded the VEI 2 eruption by approximately 4-6 months. The constant presence of precursory activity between these active periods indicate that the prior VEI 1 eruptions were linked to the later VEI 2 eruptions. Before the 2007 eruption there was no VEI 1 period. Also, during Phase III of the 2007 eruption there existed a period of lower thermal output lasting approximately two weeks. This preceded a large increase in thermal output followed by the eruption approximately 10 days later. Closer observation of the summit region in the ASTER data provides evidence of what may be occurring (Figure 3-6). The majority of thermal output is being detected in four pixels centered on the primary vent within the crater (Figure 3-6A). One week later (Figure 3-6B/E), these four pixels are no longer thermally-elevated, likely due to the conduit being blocked by backfill. During this period the size of the thermal anomaly expanded by a 5% despite the average temperature drop. This increase in total area is likely the result of the expansion of the crater fumarole field, which would provide new pathways for gas now blocked at the primary vent. The total heat released during this period is lower than that recorded earlier, indicating pressure and heat is being blocked. As pressure builds below the blocked vent, a threshold is reached and a large strombolian/volcanian vent-clearing eruption occurs, likely expanding the diameter of the conduit and increasing Figure 3-6C the 4 hottest pixels have temperatures once again higher than the surrounding pixels. However, in this case the area encompasses more than four pixels and reaches temperatures as high as 75°C above background. The production of an expanded dominant vent also reduces in the size of the thermal anomaly to 0.67 km^2. This suggested that

previous smaller (and more widely distributed) fumarole pathways are no longer active (or greatly reduced in activity as not to be detected by ASTER). A somewhat similar process was described in the Oppenheimer et al., (1993) analysis of Lascar volcano. It was believed that the explosive event that occurred in August 1986 at Lascar was triggered following the emplacement and solidification of a lava dome, which was proposed to impeded the degassing from fumaroles. The increase in pressure that occurred as a result of the presence of the dome and triggered an explosive eruption. At Kliuchevskoi, no dome was present that would have impeded the thermal output. However, it is possible the rollback of ejecta in the vent from the strombolian eruptions detected in the TIR data prior to the decrease in thermal output or the slumping of the inner conduit, destabilized from strombolian eruptions, walls may have blocked or partially blocked the dominant pathway. Once this blockage was cleared and the vent expanded, confining pressure on the magma chamber was greatly reduced, allowing for a rapid rise in magma height and the subsequent VEI 2 eruption.

3.4.4. Detection of Strombolian Eruptions

Many strombolian eruptions have been observed at Kliuchevskoi (Gushchenko, 1979; Rose and Ramsey, 2009; Smithsonian Global Volcanism Program, 2013). Research performed on Stromboli Volcano by Worden et al, (2014) demonstrates that in order to record a thermal increase from a strombolian eruption, a satellite overpass must occur within one minute of that eruption. This demonstrates that with the average number of strombolian eruptions that occur daily, a sensor with at least five overpasses per day to record this thermal signal. The temporal resolution of AVHRR (15 minutes to 6 hours depending on the latitude and orbital configuration of the

satellites carrying the AVHRR sensors) therefore suggests a strong likelihood that data are acquired soon after recently-deposited material at Kliuchevskoi. The spatial resolution of AVHRR constrains thermal detection to relatively large eruption events. Each spike in the AVHRR data therefore likely corresponds to a strombolian eruption of varying intensities (Dehn et al., 2000). This can now be confirmed with the addition of the ASTER data captured before and after one of these transient thermal events, which shows a large thermal anomaly at the summit quickly cooling over time. For example, on May 21, 2009 AVHRR data detected a larger than average thermal increase that was shown in ASTER data acquired five days later to have a size, shape and temperature profile expected for a moderately-size strombolian event. This same material was not evident 11 days before the AVHRR detection. Furthermore, a day after the ASTER image was acquired; AVHRR detected a thermal anomaly found to be 5.9°C above background using the thermally integrated pixel equation (1). This material is cooling quickly, suggesting it is thick enough to radiate heat to produce a thermal anomaly in AVHRR for close to a week.

3.4.5. Limitations

The combined use of both AVHRR and ASTER data does improve the fidelity of the TIR precursory interpretations, however there are limitations. For example, in some cases the lack of temporal resolution of the ASTER sensor reduces the ability to make more accurate interpretations (e.g., the precursory period before the 2005 eruption). This could be the case at other volcanoes that have persistent cloud cover or where the ASTER URP program has not acquired improved temporal datasets. Important information may still be gained from these sparse data through visual examination. This would be made more difficult however, if the data were examined

without knowledge of the precursory patterns during a pre-established time period. Of concern are volcanoes in locations closer to the equator that are not observed under the URP program. This lack of data could be exacerbated by a combination of the poorer temporal frequency at the equator coupled with the common increased amount of clouds in tropical regions. Although it is still possible to collect enough clear ASTER scenes to make use of this precursory interpretation method, its likelihood is decreased in these situations.

3.4.6. Future Precursory Detection

A concern with the use of any ASTER data is the age of the sensor. It has exceeded its original six-year mission life by over ad decade at the time of this study. One ASTER subsystem, the shortwave infrared (SWIR), failed in 2008. There is, therefore, a great need for reliable, high-resolution, accurate TIR data from orbit. One possible solution is the planned Hyperspectral Infrared Imager (HyspIRI) sensor, which has not been officially approved by NASA and is subject to the outcome of the next NASA Earth Science decadal survey. The notional design of HyspIRI is to have a combined multispectral TIR sensor and a hyperspectral VSWIR sensor. The spatial resolution could be as small as 30 m and the TIR temporal resolution would improve to five days at the equator and one day closer to the poles (Roberts et al., 2012). This would be a substantial increase in both spatial and temporal resolutions, with both being critical to the approach presented here. A more complete high spatial resolution dataset, similar to the ASTER URP data now available for the northern Pacific volcanoes, would be possible in an increased amount of locations (Ramsey et al, 2013). The HyspIRI TIR dataset would reduce the temporal gaps and provide coverage of volcanoes in tropical regions, thus allowing this approach to be expanded to

active volcanoes throughout the world. Furthermore, the improved spatial resolution would produce more accurate visual and thermal interpretations of smaller-scale activity, critical for precursory studies.

3.5. Conclusions

This study focused on three specific eruptions of Kliuchevskoi volcano and identified three distinct phases of precursory activity leading up to a larger eruption. In Phase I the thermal output produced at the crater remains relatively constant, similar to the heat produced during the typical, restive state of the volcano. In Phase II the thermal output becomes more variable, likely driven by the creation and rise of gas slugs causing magma levels in the conduit to rise. The transition from increasing to decreasing thermal output are marked by a series of strombolian eruptions that expel the gas, erupt hot material onto the flanks, and allow conduit magma levels to drop thereby reducing the thermal output. This cycle is detected up to six months prior to the larger eruption and typically ends approximately six weeks prior to that eruption. In Phase III the thermal output will consistently increase until the onset of the eruption. In this phase confining pressure in the magma pressure is reduced to the point where magma consistently rises in the conduit. Each of these phases can also be placed into the context of the current color codes for volcanic monitoring. Phase I corresponds to green (normal) conditions; Phase II to yellow (advisory) conditions; Phase III to orange (watch) conditions; and the actual eruption onset to red (warning) conditions. Coupling these phases with the warning codes in place provides a more quantitative reference frame to implement these codes, allowing them to be correlated with thermal output, the levels of activity, and the time before an eruption.

The approach presented here may not be universally applicable to all volcanoes depending on the data availability and style of precursory activity. However, similar thermal precursory studies are needed on a range of volcanoes, with different eruptive styles, locations, and data availability to confirm this statement. In doing, the warning period before future eruptions could be increased, giving local populations greater time to prepare, evacuate and reduce the risk to life and property.

The ability to accurately interpret volcanic precursory activity prior to an eruption improves the chances of accurately forecasting the later onset of a larger eruption. There are volcanoes that produce interpretable thermal precursory activity months to weeks prior to a larger eruption and by carefully monitoring and interpreting current satellite-based data, this activity can be tracked. Many volcanoes, however, produce seemingly random heat patterns before an eruption, which may not be clearly identified as precursory activity until very near the eruption onset. The precursory approach of this study tries to improve the interpretations of these seemingly random heat patterns by combining high temporal resolution data (e.g., AVHRR and MODIS) with high spatial resolution data (e.g., ASTER). The results show that the accuracy of forecasting a larger eruption and the lead time needed to do so is greatly improved. Data availability will continue to worsen, however, with the current fleet of aging and/or failing (e.g., Landsat 8 TIRS) high spatial resolution TIR sensors and no firm commitment for replacement.

3.6. Acknowledgements

Funding for this research was made possible by NASA under the Science of Terra and Aqua Research Program (NNX11AL29G and NNX14AQ96G) and the ASTER Science Team. The research presented here would also not have been possible with the support of the people and programs available through AVO and V-ADAPT, Inc.

.

4. ASTER ANALYSIS OF PRECURSORY VOLCANOGENIC SO_2

Reath, K.A.[1], Watson, M.[2], Realmuto, V.J.[3], Ramsey, M.S.[1]

[1] Department of Geology and Planetary Science, University of Pittsburgh, 4107 O'Hara Street, Pittsburgh, PA 15260

[2] School of Earth Sciences, University of Bristol, Wills Memorial Building, Queens Road, Clifton BS8 1RJ, England

[3] Science Division, Solid Earth Group, Jet Propulsion Laboratory, 4800 Oak Grove Drive, Pasadena, CA 91109

4.1. Introduction

The amount of volcanic gas found in magma is a primary factor controlling the explosivity of volcanic eruptions (Heiken, 1994). By gathering enough quantifiable SO_2 data to create a dataset where variations in the degassing rate during the precursory period can be observed, information can be gained about the subsurface processes occurring before an eruption. These processes include the formation of gas slugs that cause strombolian eruptions and the rising of the magma column. Analyzing high spatial resolution satellite data, such as those from ASTER should allow variations in subtle precursory degassing to be detected. Changes in volcanic gas emission rates (fluxes) commonly correspond to variations in the volcanic conduit system occurring during this period (e.g. Tilling, 1989; Sutton et al., 1993; Andres and Rose, 1995; Delgado-Granados et al., 2001, Henney et al., 2012).

When volcanic eruptions occur, they produce large amounts of volcanic gases such as H_2O, SO_2, CO_2, HCl, HF, and H_2S, as well as aerosols in the form of silicate ash, sulfates in aqueous phase droplets, and ice (Watson et al, 2013). Among these gases, SO_2 is the easiest to detect from spaceborne sensors due to the low amount of SO_2 present in the atmosphere and the strong absorptions features of SO_2 in both the Ultraviolet (UV) and Thermal Infrared (TIR) wavelength regions of the electromagnetic spectrum (Campion et al., 2010). Furthermore, measuring SO_2 flux has been shown to be an important factor where examining magmatic activity in a shallow conduit system (Edmonds et al., 2003) as well as the dynamics of volcanic systems during the precursory period (Olmos et al, 2007; Inguaggiato et al., 2011; Werner et al., 2011).

Many factors, such as geochemistry, pressure, and temperature of the source magma can contribute to flux of SO_2 of any volcanic system (e.g., Symonds et al., 1994). SO_2 flux can also be influenced by the development of hydrothermal systems, new magma injected into the magma column, and changes in the permeability of fractures and bubble networks in the column (McGonigle et al., 2003). The largest factors influencing the degassing rate of SO_2 are attributed to mechanisms occurring in the volcanic system itself. For example, the influx of fresh juvenile magma into the magma column is generally characterized by an increase in the flux of SO_2 and other volcanic gases (Caltabiano et al, 1994; Daag et al., 1996). When this occurs, the magma column can ascend in the conduit and lead to an eruption. In contrast, at the end of an eruptive period, volatile exhaustion occurs and is characterized by a decrease in SO_2 flux (Kazahaya et al, 2004). Finally, where explosive strombolian or volcanian activity occurs, SO_2 flux is periodic and linked to the rate of these eruptions (Iguchi et al, 2008). Prior to a strombolian eruption, gases coalesce in the magma column or chamber to form a gas slug. This reduces degassing rates until

the slug reaches a critical volume and it is expelled from the magma column, resulting in a strombolian eruption (Jaupart and Vergniolle, 1998).

4.1.2. Monitoring SO_2

SO_2 flux was first commonly detected with a ground-based device called the COrrelation SPECtrometer (COSPEC) (Newcomb and Milan, 1970; Moffat and Millan, 1971). The COSPEC measures the absorption feature of SO_2 in the UV region. Whereas the versatility and usefulness of the instrument is evident by the multitude of studies and resulting publications (e.g. Malinconico, 1979; Casadevall et al, 1981; Andres et al, 1989; Kyle et al, 1994; Werner et al; 2013), the COSPEC instrument presents some drawbacks. This system can be flown, used in a vehicle, or from a stationary ground location. Data acquisition is generally labor intensive and requires both the instrument and the researcher to be in close proximity to the volcanic activity (Realmuto, 1997). Thus, the risk associated with collecting COSPEC data remains a concern. More recently, ground-based mini-Differential Optical Absorption Spectroscopy (DOAS) UV spectrometers have generally replaced the COSPEC, but also require relatively close-proximity measurements (McGonigle et al., 2002).

SO_2 is also routinely monitored from spaceborne and airborne sensors, beginning with the Total Ozone Mapping Spectrometer (TOMS) sensor (Krueger, 1983). Whereas TOMS had daily global coverage and its UV wavelengths were useful for detecting SO_2 plumes, its low spatial resolution of 50 km limited it to detecting SO_2 plumes from large eruptions (Krueger et al, 1990). In 1994, NASA's airborne Thermal Infrared Multispectral Scanner (TIMS) sensor was used to

detect SO_2 plumes in the TIR region (Realmuto et al., 1994). Depending on the flight altitude, the data have a spatial resolution as high as 3m, enabling detection of very low SO_2 levels. However, airborne sensor data are limited in their usefulness because of the expense of collecting the data and hence, the temporal resolution is poor.

There are several sensors currently in orbit that are used to detect SO_2, either in the UV range(e.g., the Ozone Monitoring Instrument (OMI), the Ozone Mapping Profiler Suite (OMPS)) or the TIR range (e.g., Atmospheric Infrared Sounder (AIRS), Infrared Atmospheric Sounding Interferometer (IASI)) (Figure 4-1). Each of these sensors is sensitive to SO_2 and provides nearly daily global coverage. However, they also have a low spatial resolution and/or a weak sensitivity to tropospheric SO_2, reducing their ability to quantify SO_2 flux in passive degassing plumes, which becomes critical for precursory monitoring (Henney et al., 2006; Campion et al, 2010).

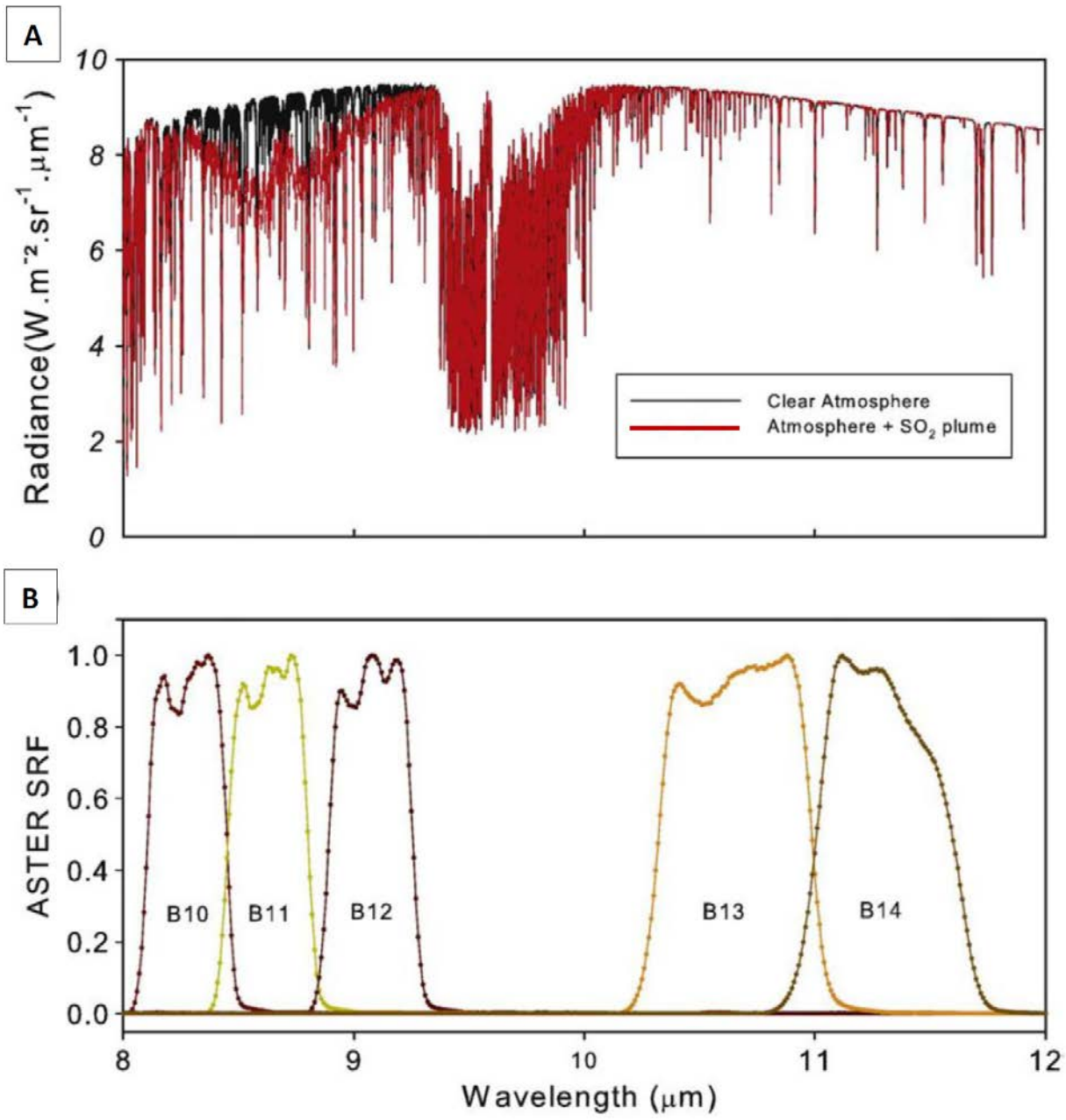

Figure 4-1: Comparison of the ASTER TIR channel locations to the absorption features of SO_2. (A) Modelled spectrum of atmosphere radiance for a clear atmosphere (black) and one containing 10 g/m^2 of SO_2 at an altitude of 3km (red). (B) Normalized spectral response function of ASTER TIR channels. Figure modified from Campion et al., 2010.

4.1.3. ASTER Sensor

The ASTER sensor was launched as one of the five instruments on the Terra satellite and first went into operation in 2000. ASTER has 15m spatial resolution in the Visible Near Infrared (VNIR) region and 90m spatial resolution in the TIR region. The TIR detector collects emitted radiance in 5 channels, (bands 11-14) centered at 8.3, 8.6, 9.1, 10.6 and 11.3µm and has a noise equivalent change in temperature (NEΔT) of 0.3K at 300K (Yamaguchi et al., 1998; Carter et al, 2008). After being erupted, SO_2 plumes generally move from the source vent at high velocities (Bluth et al., 1992) and disperse at a quick rate (Carn et al., 2007), limiting the amount of time where recently produced precursory SO_2 can be detected. ASTER's 60km swath width and acquisition times ranging from 1-5 days at the poles to 11-16 days at the equator, inhibits its use for routine, high temporal resolution volcanic monitoring (Yamaguchi et al., 1998; Ramsey and Dehn, 2004). However, ASTER has a daily acquisition schedule that controls which data are acquired and processed, based on individual user requests, global mapping campaigns, and emergency requests for acquisitions. In late 2006, the ASTER Urgent Request Protocol (URP) was implemented, enabling an automated system for volcanic data acquisition and expediting the ASTER scheduling/acquisition/processing pathway from 1-2 weeks to 1-5 days (Carter et al., 2008; Duda et al., 2009; Ramsey, 2015). The application of ASTER TIR data to detect SO_2 was realized before its launch due to the research of Realmuto et al. (1994, 1997), which focused on airborne TIR datasets. The SO_2 absorption feature corresponds with ASTER band 11 (Figure 4-1). Since its launch, numerous SO_2 studies have been performed using ASTER data (e.g. Realmuto et al., 2004; Urai, 2002; Kearney et al., 2004; Henney et al., 2006 and 2012; Campion et al., 2010 and 2012). These studies identified SO_2 emissions using several approaches. Some use band

ratios to compare bands sensitive to SO_2 absorption with those that are not. Others utilize the MAP_SO2 software, which uses the radiative transfer (RT) model based on the MODTRAN atmospheric correction program to estimate surface temperatures, emissivities and SO_2 plume concentrations. This software has recently been upgraded with the development of the PlumeTracker tool kit, which provides a much improved degree of accuracy in SO_2 detection (Realmuto et al, 2014).

4.1.4. PlumeTracker

PlumeTracker improves upon the MAP_SO2 software accuracy by using an updated version of MODTRAN in the RT model and allowing for ozone correction. Combining this new methodology with high spatial resolution ASTER TIR data, enables SO_2 flux from passively degassing volcanoes in the precursory stage to be analyzed for the first time. However, the accuracy of PlumeTracker is dependent upon the precision of the TIR radiance measurements (Realmuto, 1997). Radiance measurements are affected by the calibration and sensitivity of the instrument collecting the data as well as the accuracy of the SO_2 retrieval program itself. An instrument's sensitivity is specified by the design NEΔT, which is a measure of the smallest detectable change in temperature not considered to be noise. NEΔT remains relatively constant from image to image but does vary with the overall scene background temperature.

Identifying accurate SO_2 emissions using PlumeTracker depends upon the surface emissivity, surface temperature and elevation, plume altitude and thickness, and atmospheric temperatures and conditions (Realmuto et al, 2014). PlumeTracker uses a background emissivity spectrum extracted from TIR data away from the volcanic plume. Then, based on atmospheric

conditions and the elevation of the surface, the MODTRAN retrieval algorithm calculates how atmospheric conditions would modify the ground spectra before its thermal radiance reaches the spaceborne sensor. Any deviation from this calculated spectrum is attributed to either misfit error or the presence of SO_2. Without accurate surface emissivity and modeled atmospheric data, these calculations would produce invalid results. Additionally, plume altitude and thickness can play an important role in determining SO_2 concentrations. The retrieval algorithm is based on the thermal contrast between the ground and the plume (Realmuto, 1994; Realmuto, 2000). In a sensitivity analysis of the previous version of the software (MAP_SO2), Campion (2010) found that where ground and plume temperatures were similar, no SO_2 was detected. This thermal contrast (or lack thereof) is determined based upon the difference in elevation of the plume and the ground. In many cases there is no *a priory* information on the height of the plume, which results in a model assumption of the plume height being 1km above the vent. Whereas each of the variables needed for an accurate representation of SO_2 concentrations using PlumeTracker stem from multiple sources of information, this software enables these differing sources to be included in the model, resulting in the most precise model data available. This enables the user to generate the highly accurate SO_2 plume concentrations using any available TIR data.

4.1.5. Volcanic Precursor Data

Variations in the flux of SO_2 have been identified as a precursors to eruptive activity. Due to volcanic hazards, severe weather conditions, or remote locations of volcanoes, detecting these variations is not always possible. In many cases, remotely detecting these changes in SO_2 flux

from satellite sensors becomes the best and only option. ASTER possess the highest spatial resolution of the TIR and UV spaceborne sensors able to detect SO_2. With the increased accuracy of these data after being processed with PlumeTracker, it is the ideal candidate to detect the low degassing rates that occur during the precursory period. However, before these data can be interpreted from volcanoes on a global scale, the limitations and sources of error need to be identified as well as the expected magnitude and variability of activity during the precursory period need to be properly understood.

In this study, two well documented volcanoes, Mt. Etna, in Sicily, Italy, and Kilauea volcano in Hawaii, act as test locations to help constrain the limitations of the combined ASTER/PlumeTracker method and facilitate establishing a baseline of SO_2 flux observations before an eruption. Possible limitations to the ASTER/AVHRR method include determining the minimal amount of degassing needed to detect a SO_2 plume, the sensitivity of daytime and nighttime data, and the effect of cold backgrounds on the detection sensitivity. These ASTER derived data can be tested against both ground and satellite based measurements captured at both of these volcanoes, producing a more complete dataset. The accuracy and limitations of the ASTER data from these studies can then be used to evaluate the potential of this approach in monitoring activity at volcanoes where environmental conditions or lower degassing rates limit the amount of usable data points, such as Kliuchevskoi volcano in Kamchatka, Russia.

4.1.6. Mt. Etna

Mt. Etna is the largest active volcano in Europe and one of the most active volcanoes on Earth. Etna is also one of the leading sources of volcanogenic SO_2 in the world (Berreshiem et al., 1983; Bluth, 1997; Aiuppa et al., 2005). For this reason, as well as for the large amount of CO_2 it produces, Etna has been the subject of numerous volcanic degassing studies where volcanic activity has been closely related to the SO_2 degassing rates (e.g. Malinconico, 1979; Caltabino et al., 1994; Francis and Maciejewski, 1995; Bruno et al., 1999; Pugnaghi et al., 2006; Pugnaghi et al., 2013). For example, Caltabiano et al. (1994) used a COSPEC and found SO_2 flux diminished up to 1 month before eruptive events, at which point it would then increase to well above background levels prior to the eruption.

The most recent eruption of Mt. Etna occurred on December 2, 2015 after two years of relative inactivity. The eruption was noted to be among the strongest in the last 20 years, producing a 1km high lava fountain, lava bombs, and several km high ash clouds (Global Volcanism Program, 2015). This activity continued until December 9th, when activity had diminished to strombolian eruptions and small ash clouds (Global Volcanism Program, 2015). Unfortunately, reported information relating to volcanic activity during the precursory period of this eruption is limited, therefore no ground-based SO_2 flux data are available before this eruption. However, the occurrence of strombolian eruptions producing ash clouds were reported in early May (Global Volcanism Program, 2015). This eruption presents an opportunity to analyze SO_2 flux on a well-monitored volcano to demonstrate the utility of PlumeTracker and ASTER data during the precursory and eruptive period. As had been noted in the past, the modeled flux

should show a decrease months before, and then an increase leading up to, the eruption (Caltabiano et al., 1994).

4.1.7. Kilauea Volcano

Another volcano that has been the subject of many SO_2 emission studies is Kilauea Volcano (e.g. Andres et al, 1989; Gerlach et al., 1998; Porter et al., 2002; Carn et al., 2009, Edmonds et al., 2013). Kilauea currently has two main vents that produce the majority of the SO_2: Halemaumau crater, a pit crater found within the large summit caldera of Kilauea, and Pu'u'O'o, a vent found in the eastern rift zone. On March 19, 2008, the first explosive summit eruption since 1924 opened a new crater, known as Observation crater, within Halemaumau (Wilson et al., 2008). This crater was expanded by subsequent explosive events that occurred on April 9 and 16, August 1 and 27, and September 2, 2008, until the crater was filled by a lava lake on September 5, 2008 (Global Volcanism Program, 2008). The advantage of a summit derived eruption, compared to a rift derived eruption, is that it offers a direct window into the summit magma column and therefore more accurately represents the degassing processes related to the summit magma chamber (Edmonds et al, 2013). During this period, SO_2 emissions were monitored by the Hawaii Volcano Observatory (HVO). A SO_2 background degassing rate of approximately 140 t/d was detected until early January, when emissions began to steadily increase until a high of 2500 t/d was reached on March 16, 2008 (Global Volcanism Program, 2010). As a result of the opening of a new crater and its subsequent infilling with a lava lake, SO_2 levels remain elevated well above background levels recorded in 2003-2007 (Global Volcanism Program, 2010). Applying

PlumeTracker to the ASTER TIR data should allow rates to be extracted and compared to ground-based monitoring stations and reinforce the utility of TIR data to analyze SO_2 emissions, while providing additional insight into the volcanic processes occurring during this series of eruptions.

4.1.8. Kliuchevskoi Volcano

Of the 29 active volcanoes in Kamchatka, Kliuchevskoi is one of the most active, producing an average of 6.0×10^7 tons of material per year (Fedotov et al., 1987; Fedotov and Masurenkov, 1991; Ozerov et al., 1997). At an elevation of 4750m, Kliuchevskoi is the tallest volcano in Asia and therefore commonly has cold temperatures and unstable weather conditions at the summit. Summit eruptions are the dominant style at Kliuchevskoi over the past few decades, occurring approximately every 1-2 years (Fedotov and Masurenkov, 1991; Rose and Ramsey, 2009; Global Volcanism Program, 2013). These eruptions are characteristically Strombolian to sub-Plinian in nature and have a longer duration than the prior flank eruptions (Gushchenko, 1979; Global Volcanism Program, 2013). Relatively small SO_2 emission rates have been identified at Kliuchevskoi during eruptive periods in the past (SEAN Bulletin, 1994; Bluth et al., 1997; Rose and Ramsey, 2009; Clarisse et al., 2012). This limited amount of SO_2 degassing, coupled with the summit weather conditions, will serve as a worse-case test of the PlumeTracker software to identify summit SO_2 emissions in ASTER TIR data. Additionally, Reath et al. (2016, submitted) studied the thermal eruptions precursors at Kliuchevskoi occurring in 2009, which provides a unique opportunity to compare the thermal to the degassing eruption precursors.

4.2. Methods

4.2.1. Data Collection

ASTER Level 1B (L1B) and the digital elevation model (DEM) data products were chosen using the US Geological Survey (USGS) Global visualizer viewer (Glovis). Only cloud-free summit data were chosen for this analysis. In addition, Moderate Resolution Imaging Spectroradiometer (MODIS) data, used to extract atmospheric information, were chosen using the NASA, Land, Atmosphere Near real-time Capability for EOS (LANCE) Rapid Response website. MODIS scenes were selected that were acquired at the same time as the ASTER scenes. Data were download using the NASA Level 1 and Atmosphere Archive and Distribution System (LAADS) ftp site.

4.2.2. Data Pre-Processing

Each ASTER scene is received as a Level 1B, AST_L1B product (Abrams, 2000). In order for data to be processed by the PlumeTracker software, it must be separated into several input data formats (Realmuto, 2014). These data productss are an IRAD data product, which corresponds to TIR radiance at the sensor data comprised of the five TIR ASTER channels. A spectral response data product, which contains the spectral response specific to the sensor being analyzed; and a Zen data product, which contains the zenith angle at which each pixel in the scene was captured. There are other optional data products which the software does not require to run. These include the latitude and longitude values of each pixel, for precise geolocation of the data set. Although it is considered an optional data product, a DEM is needed to account for the surface elevation under the plume to improve detection accuracy. DEM data products are generated from any clear

daytime ASTER scene and processed on-demand as a level-2 product. In order to match the DEM to nighttime radiance data, several DEM scenes were mosaicked together in order to span the entire area represented by the radiance image. These mosaics were resampled, using a DEM sampling tool developed by V. Realmuto and the Jet Propulsion Laboratory (JPL), to match the area of the scenes being processed.

One or several index images are created in the same dimensions and orientation as the original TIR ASTER scene. These index scenes allow the user to navigate within PlumeTracker. By creating several different types of index images, this navigation is much more clear and accurate. In this study, three types of data are used to create the index images. The most basic is the brightness temperature, which is extracted by performing emissivity normalization on TIR radiance data. Visible Near Infrared (VNIR) images were also used and resized to match the 830 by 700 scene dimension of the TIR data. Finally, TIR decorrelation stretch (DCS) images were created (Gillespie et al., 1986). These images are designed to highlight compositional and temperature variations in a TIR scene (including absorbing atmospheric gases). Three ASTER TIR channels are chosen and for the DCS depending on the spectral feature under study. In this case, bands 14, 13, and 11 are assigned to red, green and blue (RBG) to primarily highlight SO_2, which commonly is denoted by a yellow color in the DCS. Another important piece of data that allows SO_2 concentration to be modeled is an accurate atmospheric profile at various altitudes. Fortunately, the MODIS sensor, which is also on the Terra satellite, collects atmospheric profile data that assigns atmospheric values to every MODIS pixel. However, each MODIS pixel is an order of magnitude larger than ASTER and the atmospheric profile must be extracted over water to ensure its accuracy. In order to confirm the location of the collection of the atmospheric

profile, the MOD021KM (one kilometer calibrated radiance) and the MOD07_L2 (atmospheric profile) data products are needed. The locations of cloud-free pixels close to the volcano of interest and still over the ocean are identified in the MOD021KM data and the atmospheric profiles of these pixels are extracted from the MOD07_L2 data.

4.2.3. SO_2 Processing

After entering the pre-processed data into PlumeTracker, a background ASTER TIR emissivity is established in order to 'fine-tune' the atmospheric values. To accomplish this, an area with a known emissivity spectrum, typically over snow or water, is identified using the index images. The known emissivity spectrum is assigned to this area and a TIR temperature retrieval is performed. The temperature retrieval algorithm calculates the actual emissivity of the area and corrects for the atmospheric scatter by comparing the emissivity spectrum to that of the known spectrum. Assuming the atmospheric profile received is accurate, the calculated spectrum should match the assigned spectrum. However, even the most accurate atmospheric profile introduces uncertainties. PlumeTracker allows the user to modify both water vapor and ozone concentrations to better match the observed and predicted spectra. The 'true' atmospheric values are established once these factors have been modified to the point where the spectra have their best match. Next, an area with a similar composition to the area beneath the SO_2 plume is selected in the index images and its emissivity is calculated and assigned as the background emissivity. The SO_2 retrieval algorithm is run on the entire area surrounding the volcano. The model calculates SO_2 concentrations needed to best match the extracted spectrum

on a pixel by pixel basis in the sample area. Upon completion, PlumeTracker produces several maps, including the SO_2 concentration map and a misfit map, which shows the areas with the highest amount of error in calculating SO_2 concentrations.

Two methods are used to test the validity of the produced SO_2 concentration map. The first method compares the concentration map and the misfit map. Values of the misfit map are based on least square fit values between the observed and predicted spectra. Any values below 1 are considered a reasonable match. The pixel spectra can also be examined visually on a pixel by pixel basis to confirm how well the predicted and observed spectra match.

4.2.4. Calculating Quantitative SO_2 Data

A significant feature of the PlumeTracker software is its ability to produce SO_2 concentrations in g/m^2 for each pixel, which allows a quantitative total estimate of SO_2 to be calculated at that moment in time. To produce these values for a SO_2 plume, the ENVI software is used to create a region of interest (ROI) that surrounds only the areas where SO_2 emissions were positively identified (Figure 4-2). This ROI was limited to areas within 4km of the emission source in order to analyze recently produced SO_2, before it becomes dispersed into the surrounding air. The average values within this region were then multiplied by the total area of the ROI to produce a total instantaneous SO_2 amount. In areas where PlumeTracker did not identify any SO_2 emissions, the total SO_2 amount is assigned a value of 0. The results allow SO_2 to be directly compared and plotted over time in order to interpret any changes in emission rates that may precede or occur during an eruption. For this study, the SO_2 data relating to the 2009 eruption of Kliuchevskoi is

also plotted against the previously-established thermal anomaly temperature dataset in Reath et al. (2016, submitted) as a comparison.

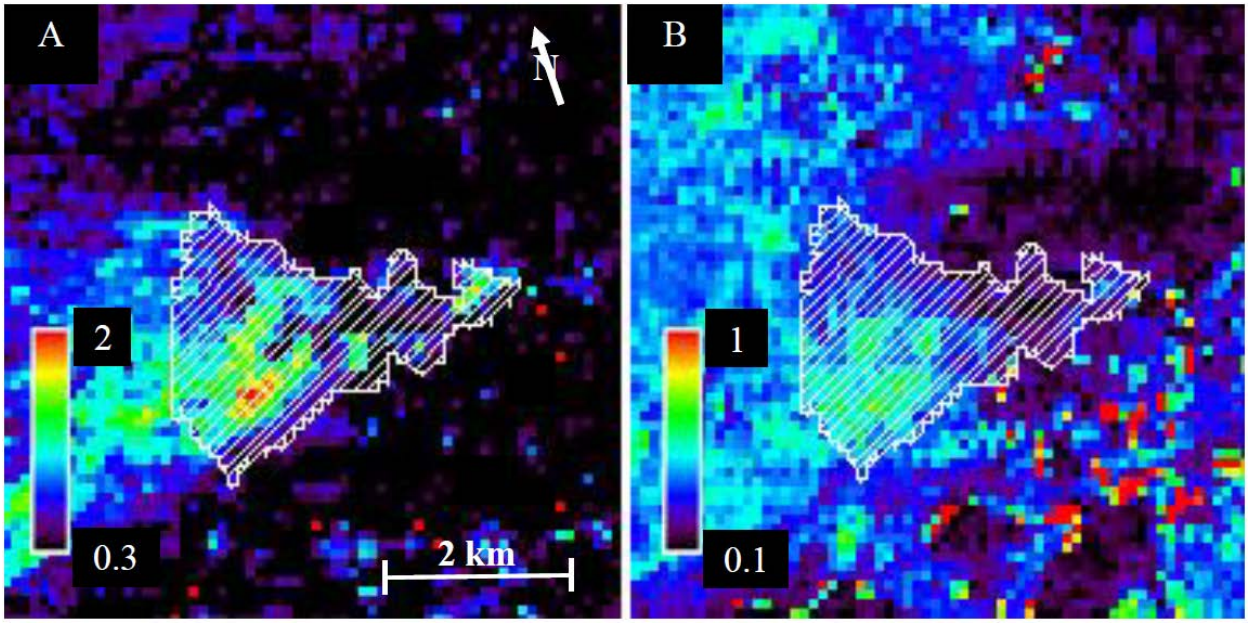

Figure 4-2: Images modified from an ASTER scene acquired June 2, 2009 00:45 UTC of Mt Etna, showing the ROI area assigned to SO_2 plume in white. (a) SO_2 concentration map with values in g/m^2 and (b) SO_2 misfit map with values in least square fit

4.3 Results

4.3.1. 2015 Etna Eruption

Daytime ASTER data collected over Mt. Etna from September 19, 2014 to December 18, 2015 are used in this study. Unfortunately, no completely cloud-free scenes are available after December 18. Based on the data gathered during this study, from September 18, 2014 to April 22, 2015 the total amount of instantaneous SO_2 remained relatively constant averaging approximately 15kg within 4km of the source vent. These emissions increased to 32kg on May 24 and peaked at 55.6kg on June 2, 2015. In the scene captured on May 24, 2015, the SO_2 plume was partially

obscured by clouds, meaning this value may be underestimated. The timing of this peak and the large plume observed in the June 2 ASTER scene (Figure 4-3) suggest it is related to a continuation of the strombolian activity that was reported in early May. On July 20, total modeled emissions had once again dropped to 35kg. From July 20 to December 18, 2015, no cloud-free daytime ASTER scenes were acquired. The December 18 scene was captured 9 days after activity related to the eruption was reported to have ended. In this scene the lowest SO_2 emissions were recorded, with 4.24kg of SO_2 within 4km of the source. Variations in the instantaneous SO_2 amounts of these data are seen in Figure 4-4.

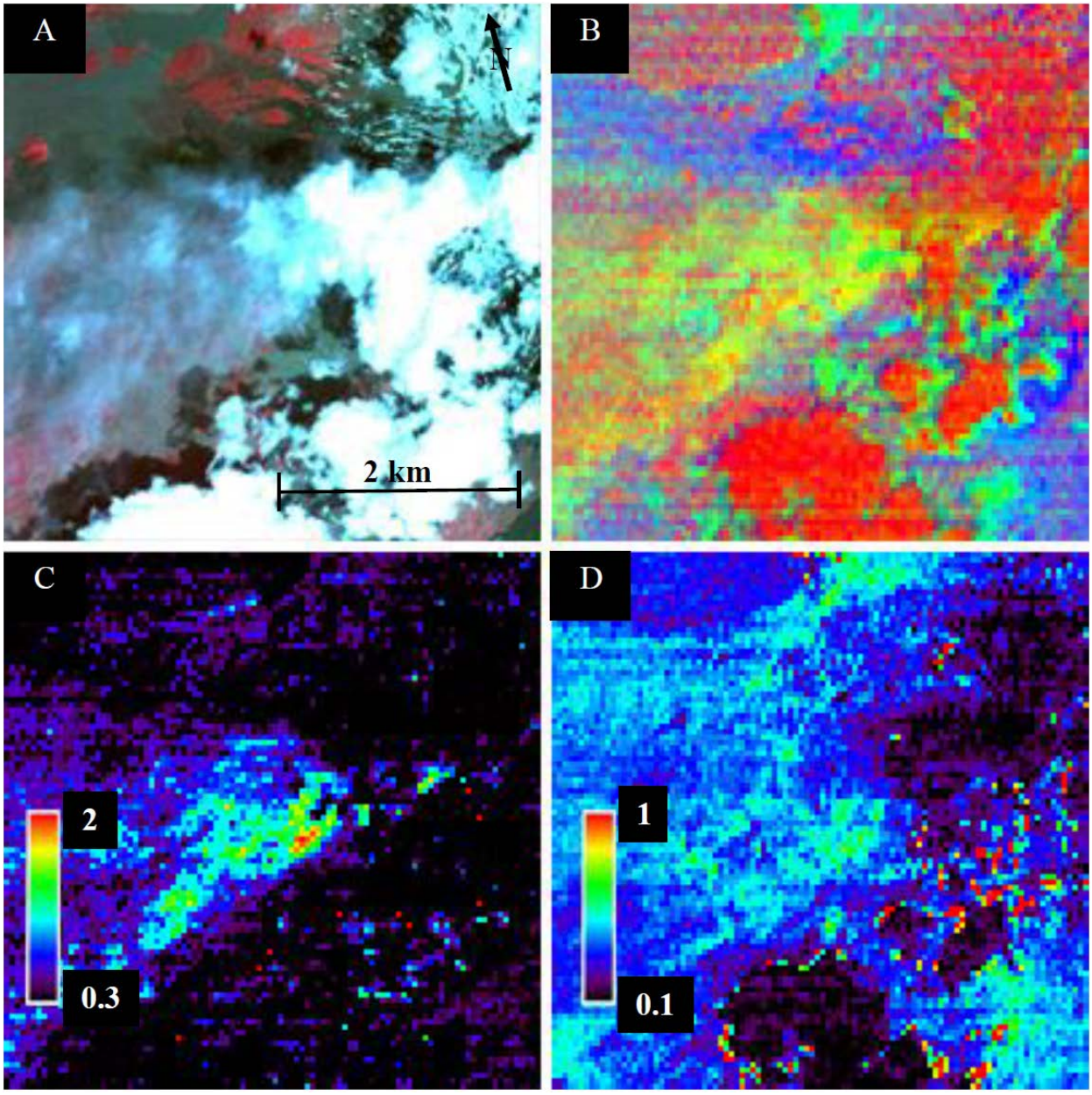

Figure 4-3: Images modified from the ASTER scene acquired June 2, 2015 09:54 UTC over Mt. Etna (A) VNIR image with bands B3, B2, B1 in RGB (B) Decorrelation stretch (DCS) with bands B14, B13, B11 in RBG, SO_2 shows up as yellow (C) SO_2 concentration map with values in g/m^2 and (D) misfit map with values in least square fit

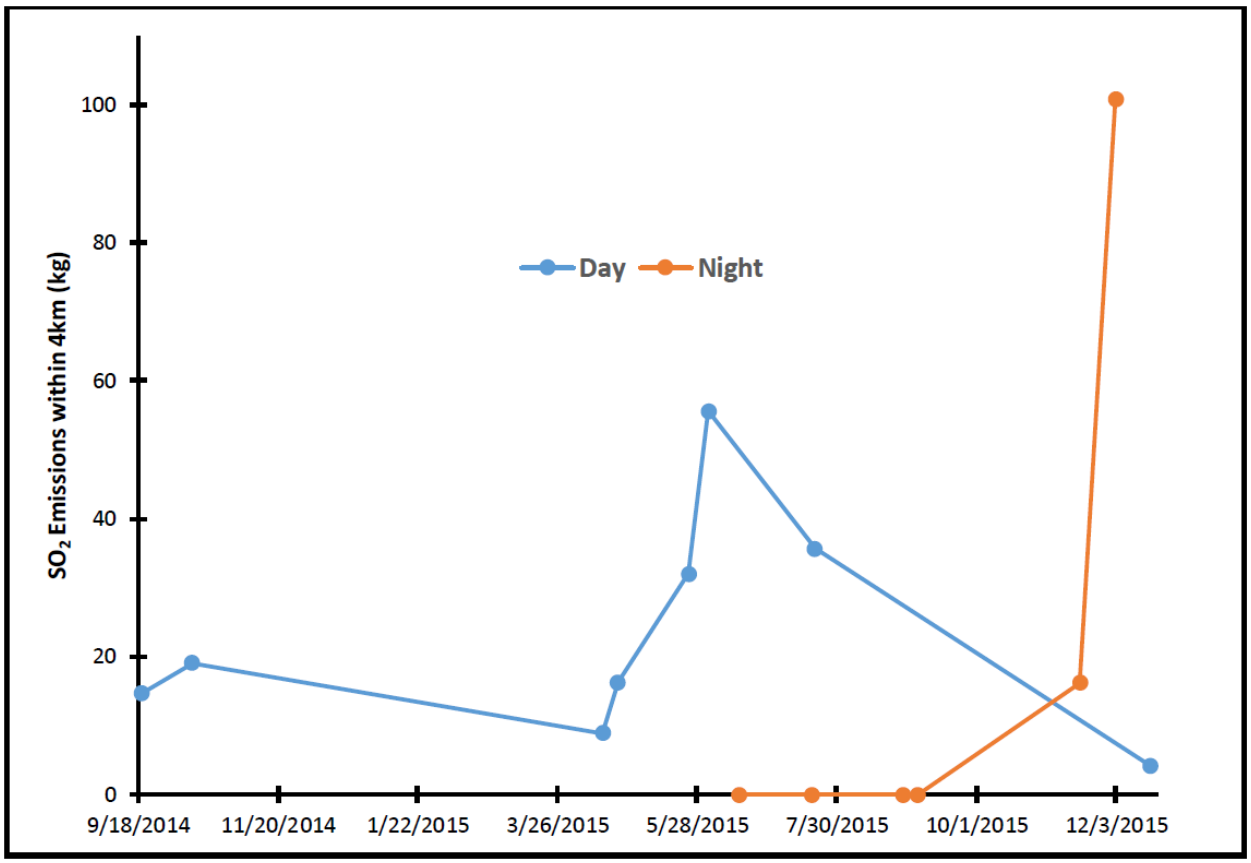

Figure 4-4: SO_2 emissions measured within 4km of the Mt. Etna vent. Daytime data are plotted in blue and nighttime data in red. These two datasets cannot be directly compared due to the differing TIR sensitivity levels between day and night. Whereas these values appear together on one graph, they are plotted as two separate datasets.

Six nighttime ASTER scenes from June 16 to December 2, 2015 were used in an attempt to fill some of the temporal gap present in cloudy daytime ASTER data (Figure 4-4). It is important to note that there is a difference in SO_2 detection sensitivity between scenes captured at day and night. Whereas the values for these two datasets cannot be directly compared, valuable information can be gathered by analyzing both the day and night scenes together. From June 16 to September 4, 2015, no SO_2 was detected, which is best shown by the June 16 scene (Figure 4-5), captured between two daytime scenes that identified large amounts of detectable SO_2. On

August 28 a plume originating from a summit vent was detected. However, it was not modeled as having any detectable SO_2. The scenes acquired 15 days before the onset of eruption, on November 16 and hours after the onset of eruption on December 2, did positively identify a SO_2 plume. However, in both cases this plume was more diffuse than in previously observed daytime scenes (Figure 4-6).

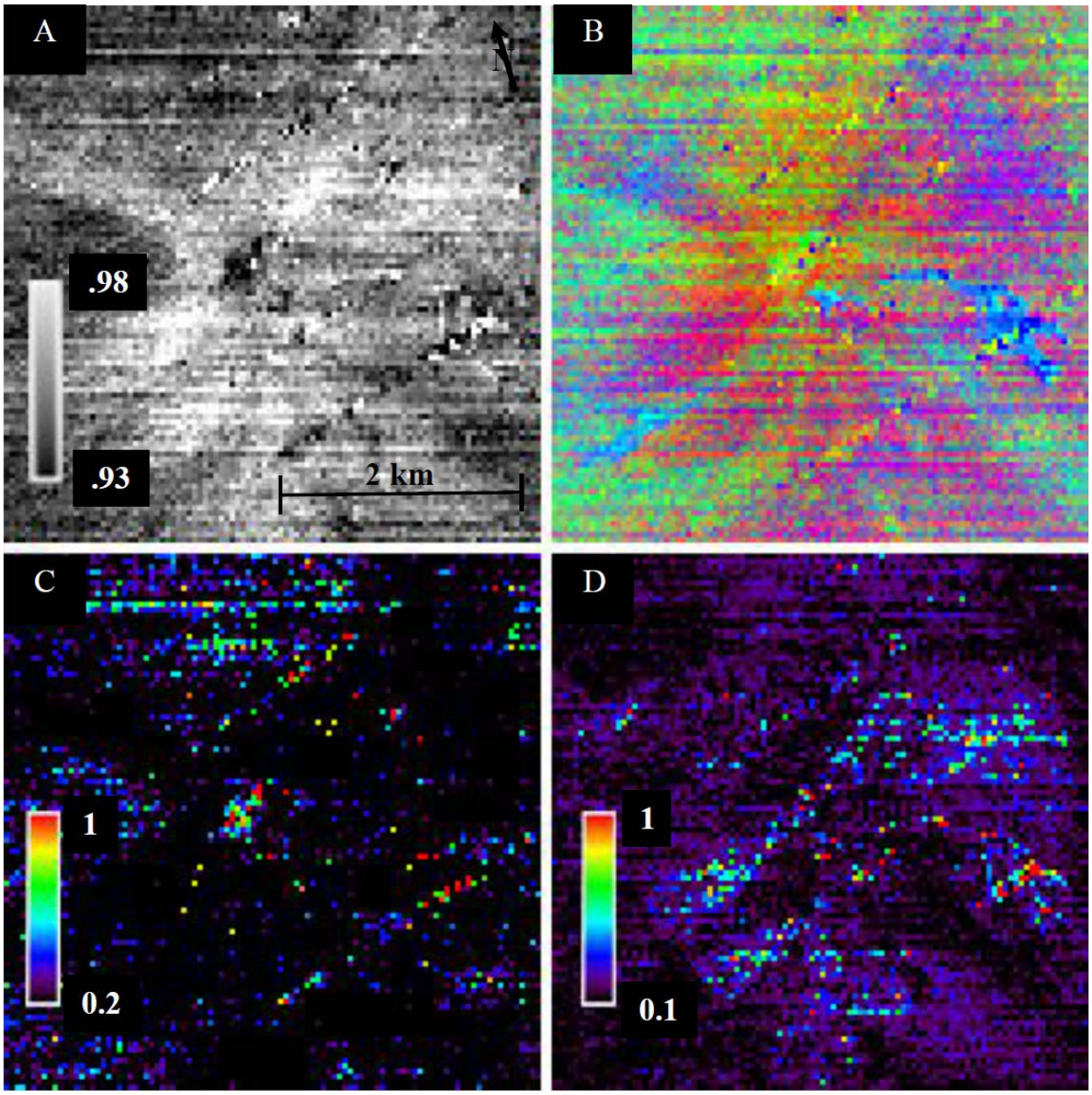

Figure 4-5: Images modified from the ASTER scene acquired June 16, 2015 21:10 UTC over Mt. Etna (A) Band 11 (8.6µm) emissivity (B) Decorrelation stretch (DCS) with bands B14, B13, B11 in RBG, highlighting SO_2 in yellow (C) SO_2 concentration map with values in g/m^2 and (D) misfit map with values in least square fit

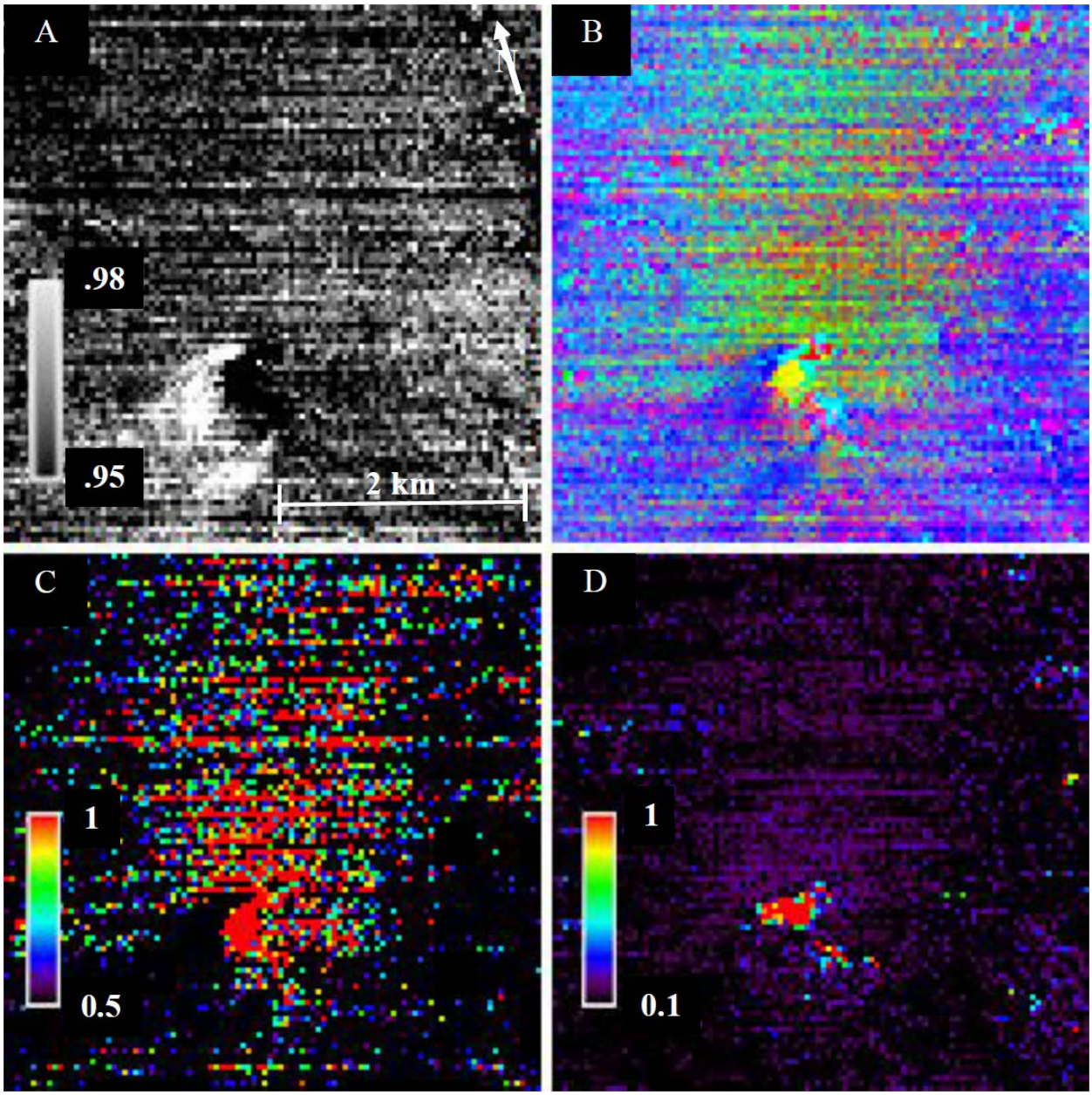

Figure 4-6: Images modified from the ASTER scene acquired December 2, 2015 21:10 UTC over Mt. Etna (A) Band 11 (8.6µm) emissivity (B) Decorrelation stretch (DCS) with bands B14, B13, B11 in RBG, highlighting SO_2 in yellow (C) SO_2 concentration map with values in g/m^2 and (D) misfit map with values in least square fit

4.3.2. 2008 Kilauea Eruption

Daytime ASTER scenes collected over Kilauea from July 7, 2007 to March 23, 2008 are used in this study. No cloud-free data are available for 28 months before and 36 month after this period. Daytime ASTER data modeled with PlumeTracker are able to detect SO_2 emissions during periods when the emission rate recorded by HVO is at background levels (140 t/d) (Global Volcanism Program, 2010); however, these plumes are difficult to distinguish in ASTER data. HVO recorded emissions rates elevated by two to four times background levels starting in early January. This lasted until March 3rd where an emission rate of 970 t/d was recorded. This rate increased rapidly with a measurement of 1600 t/d on March 12 and 2500 t/d on March 16 (Global Volcanism Program, 2010). Using ASTER data collected March 23, 2008, 4 days after the explosive eruption that created overlook crater, a large SO_2 plume was observed originating from the eastern side of Halemaumau crater (Figure 4-7), 81kg of instantaneous SO_2 are detected in this image. The next flux measurement from HVO, also recorded on March 23, had dropped to 2200 t/d. Three days later, on March 26 the emission rate had dropped 1500 t/d (Global Volcanism Program, 2010). Due to a lack of cloud-free daytime captured ASTER data, the remainder of this eruption was analyzed using only night ASTER scenes captured from November 25, 2007 to August 23, 2008. The only nighttime scene that positively identified SO_2 emissions was captured on April 17, 2009, one day after the third explosive event that expanded Overlook Crater (Figure 4-8). On this day, 91kg of SO_2 could be identified within 4km of its source. Although three night scenes captured on March 28, July 6, and August 23, 2008 had plumes originating from Overlook crater, none were modeled as containing SO_2. This phenomenon is best exemplified by the scene captured on August 23 (Figure 4-9). In this scene a southerly plume can be seen. However, in

none of the four images presented in Figure 4-9 does this plume exhibit SO_2 spectral features. The instantaneous SO_2 values gathered from these methods as well as the range of weekly SO_2 flux measurements captured by HVO are shown in Figure 4-10.

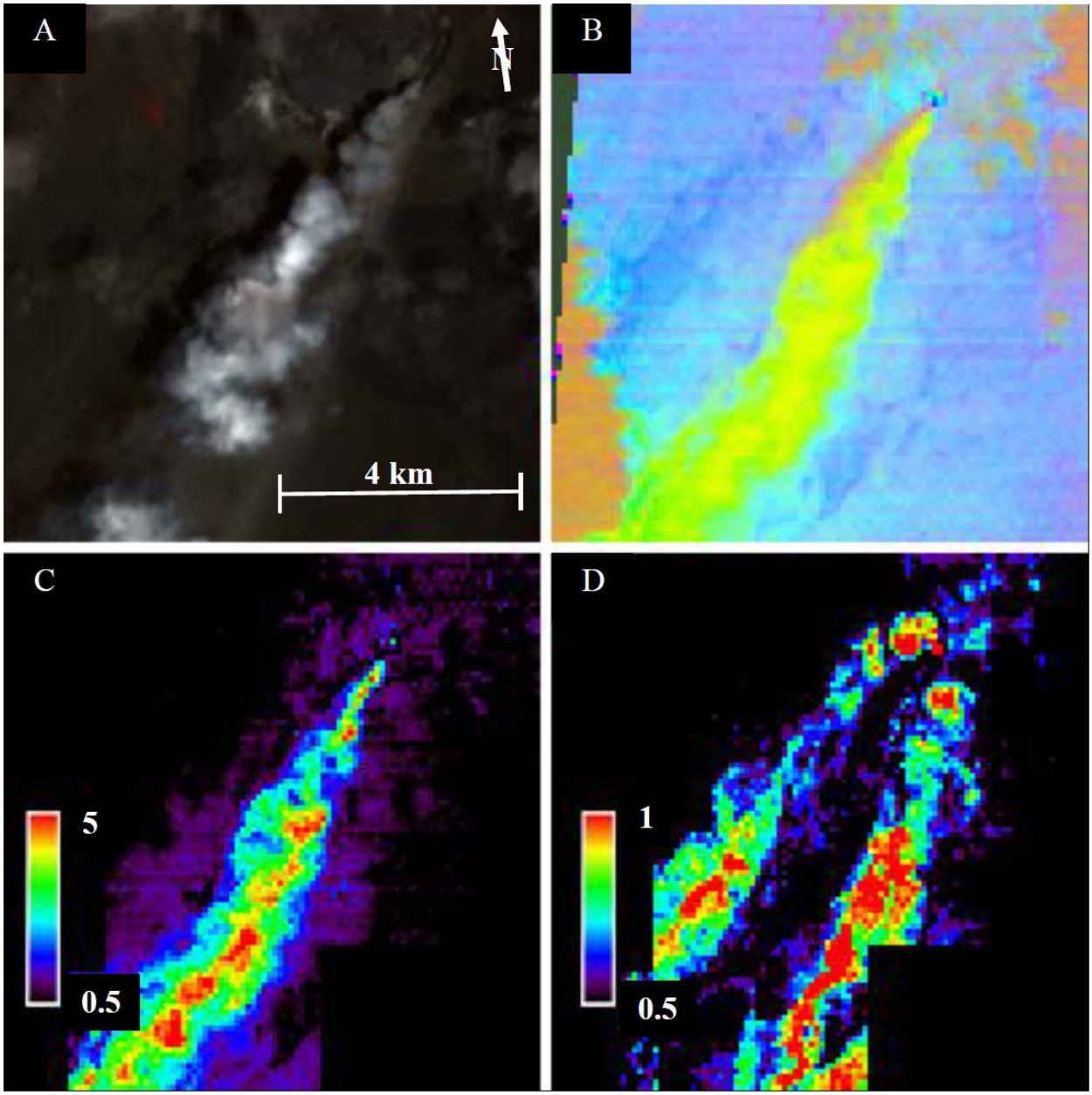

Figure 4-7: Images modified from ASTER scene acquired on March 23, 2008 20:59 UTC over Halemaumau Crater, Kilauea Volcano (A) VNIR map with bands B3, B2, B1 in RGB (B) Decorrelation stretch (DCS) with bands B14, B13, B11 in RBG, highlighting SO_2 shows in yellow (C) SO_2 concentration map with values in g/m^2 and (D) misfit map with values in least square fit

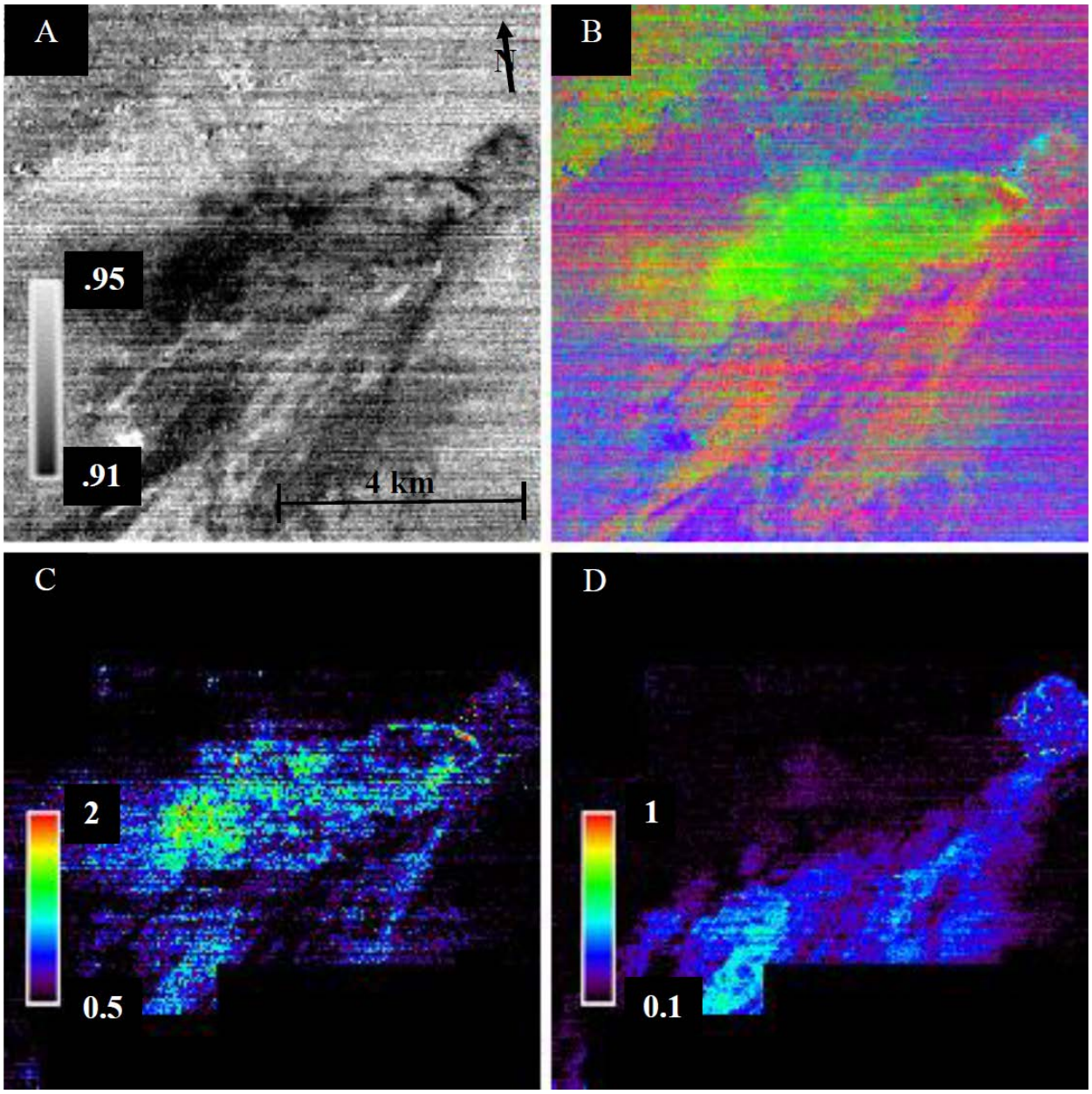

Figure 4-8: Images modified from the ASTER scene acquired April 17, 2008 08:42 UTC over Halemaumau Crater, Kilauea Volcano (A) Band 11 (8.6µm) emissivity (B) Decorrelation stretch (DCS) with bands B14, B13, B11 in RBG, highlighting SO_2 in yellow (C) SO_2 concentration map with values in g/m^2 and (D) misfit map with values in least square fit

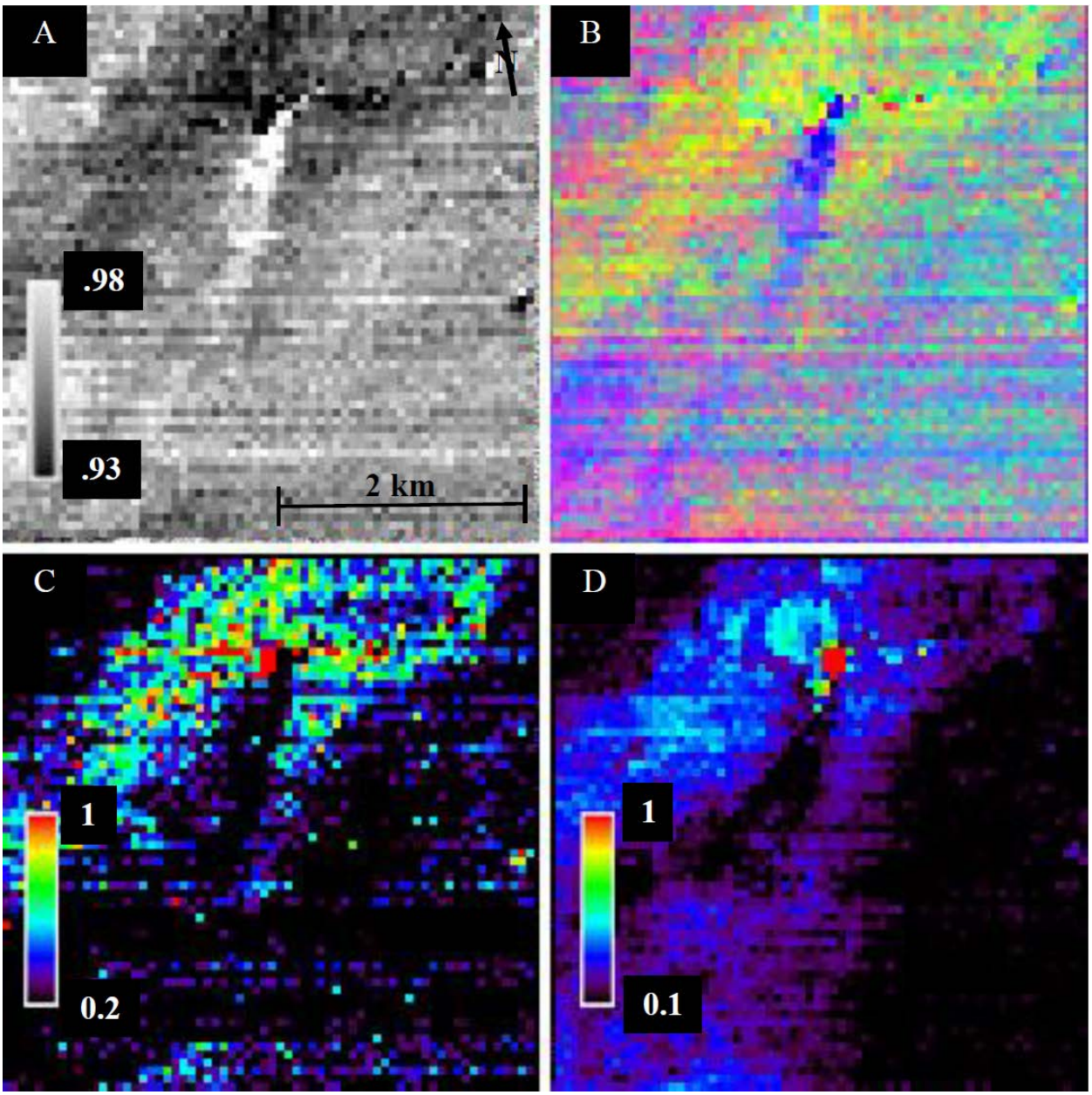

Figure 4-9: Images modified from the ASTER scene acquired August 23, 2008 08:43 UTC over Halemaumau Crater, Kilauea Volcano (A) Band 11 (8.6µm) emissivity (B) Decorrelation stretch (DCS) with bands B14, B13, B11 in RBG, showing almost no SO_2 (C) SO_2 concentration map with values in g/m^2 and (D) misfit map with values in least square fit

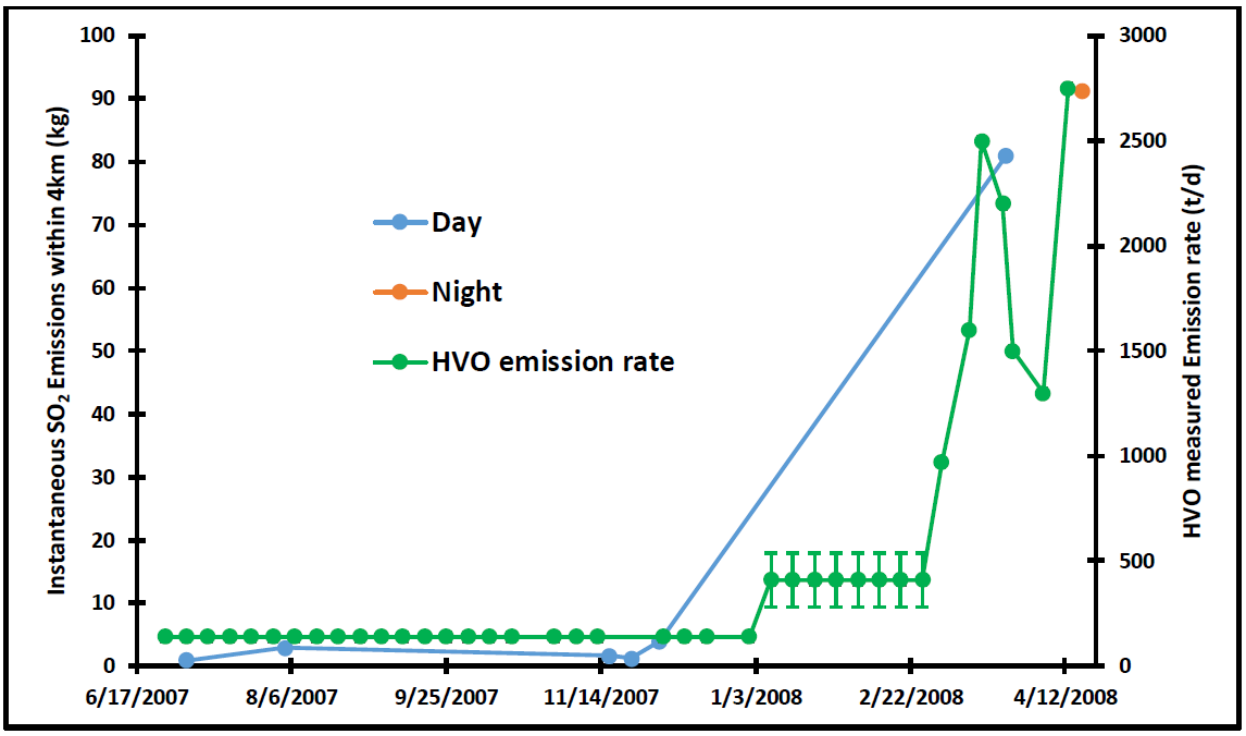

Figure 4-10: SO_2 emissions within 4km of the vent source of Overlook crater calculated using PlumeTracker recorded as blue points (day) and a red point (night). Green points represent emissions rates measured from the ground by HVO as reported to the Global Volcanism Program, (2010).

4.3.3. 2009 Kliuchevskoi Eruption

Of the ten daytime ASTER scenes captured in the precursory time period before the 2009 eruption, four scenes produce valid results after the data are processed. In these scenes the noise levels surrounding Kliuchevskoi are low enough that it is possible to detect a SO_2 plume or to determine if the area surrounding the summit is free of SO_2. None of the scenes captured at night produce valid results. Of the four valid daytime scenes, SO_2 plumes are only detectable in two scenes. On April 6, 2009, 11.8kg of total SO_2 are detected. A small SO_2 plume is observed originating from the main vent, drifting to the northwest (Figure 4-11C). A single pixel with high concentrations of SO_2 on the west slope of Kliuchevskoi may be the result of a degassing

fumarole. On both May 10 and 26, 2009, no SO_2 emissions are detected. On July 4, 71.2kg of total SO_2 emissions are detected originating from the crater and drifting to the northwest (Figure 4-12). The lava flow created during the previous eruption runs through the center of the area and is positively identified as containing SO_2. Where these values are plotted against the previously established thermal anomaly temperature values (Figure 4-13) a correlation between precursory phases and SO_2 amount are observed. During Phase II, where the variation in thermal anomaly temperatures are believed to be the result of strombolian eruptions, little to no airborne SO_2 is detected. Whereas in a scene collected in Phase III increased amounts of airborne SO_2 are detected. In this phase, the consistent increase in thermal output is believed to be the result of the magma column rising in the conduit.

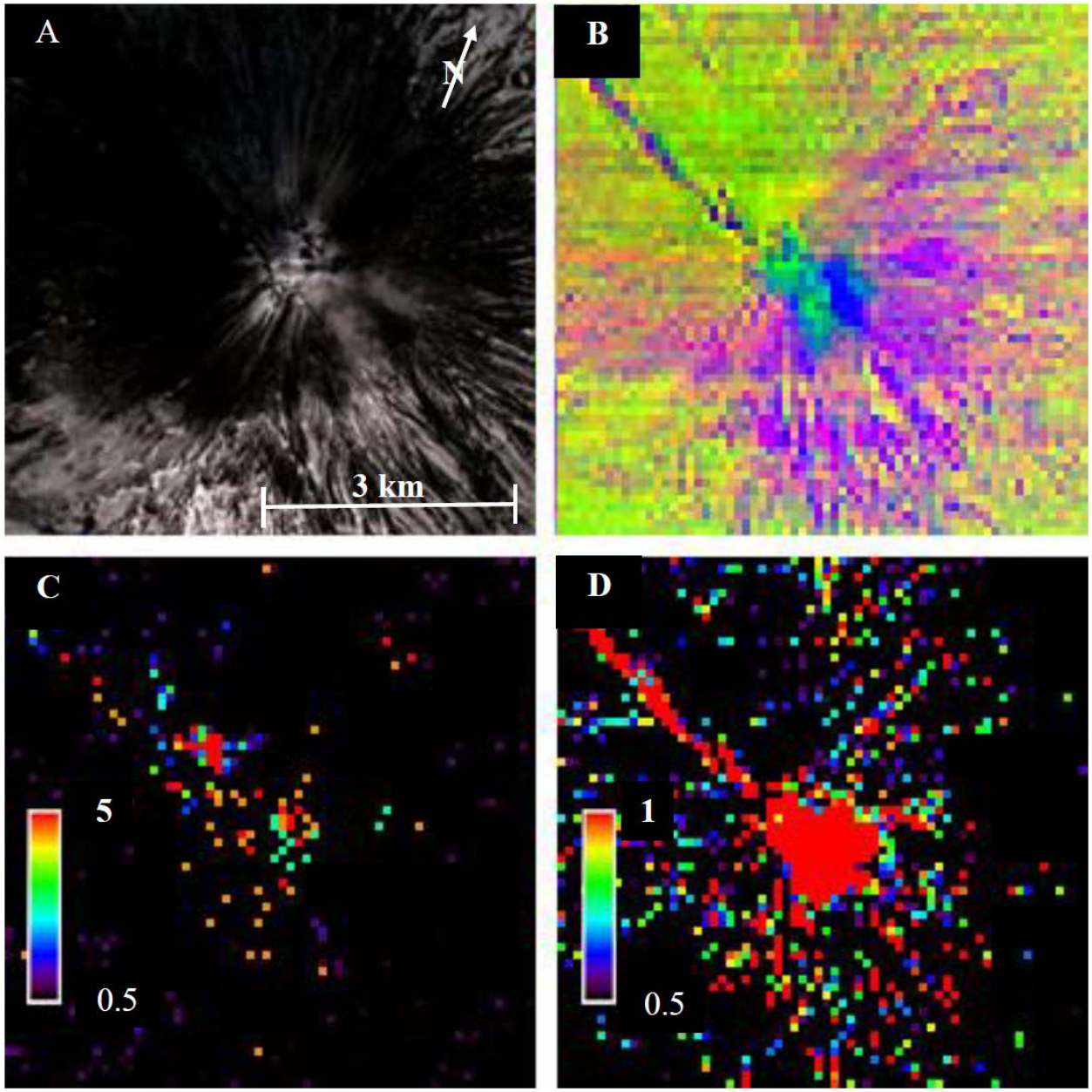

Figure 4-11: Images modified from the ASTER scene acquired April 6, 2009 00:45 UTC (A) VNIR map with band B3, B3, and B1 (B) decorrelation stretch map with bands B14, B13 and B11 in RBG (C) SO_2 concentration map with values in g/m^2 and (D) misfit map with values in least square fit

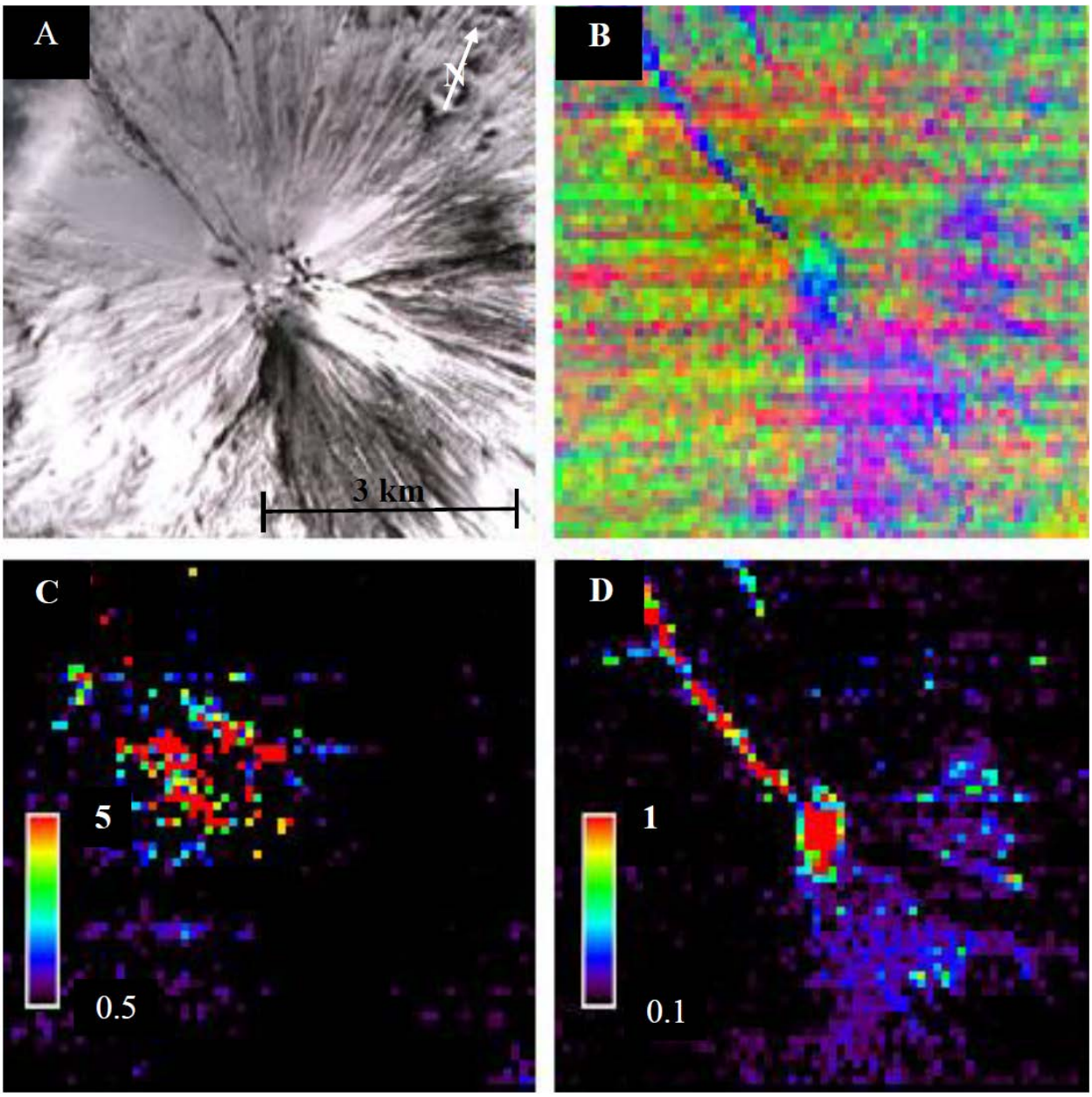

Figure 4-12: Images modified from the ASTER scene acquired July 4, 2009 00:38 UTC (A) VNIR image with band B3, B2 and B1 in RBG (B) decorrelation stretch image with channels B14, B13 and B11 in RBG, (C) SO_2 concentration map with values in g/m^2 and (D) misfit map with values in least square fit

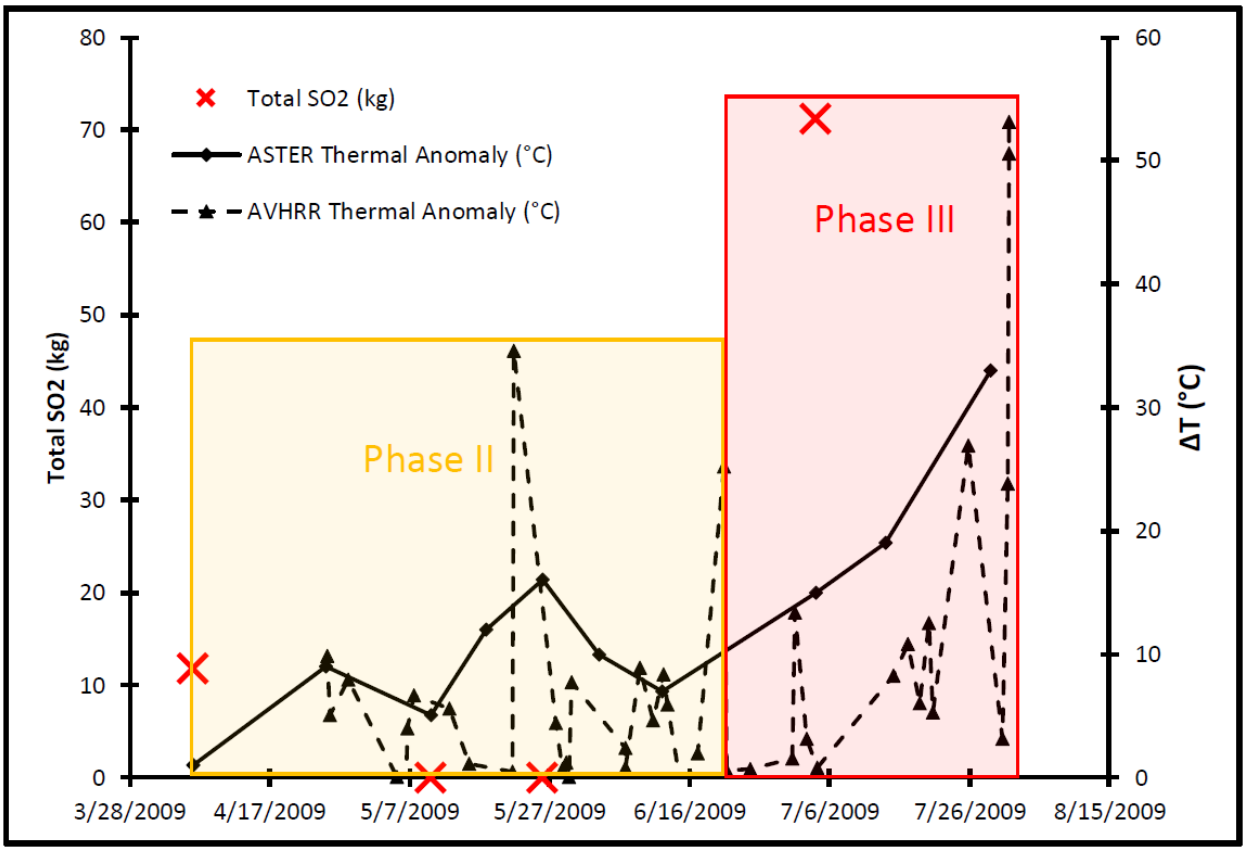

Figure 4-13: Total SO_2/Temperature plot of the precursory period prior to the VEI 2 eruption on August 15, 2009. Phases II and III as classified by Reath et al. (2016, submitted) based on thermal output.

4.4. Discussion

4.4.1. Utility of ASTER data to Detect SO_2

During the precursory eruption period on both Etna and Kilauea, no daytime data were collected due to ASTER's limited temporal resolution combined with cloudy weather conditions. However, where compared to the two sensors currently employed in NASAs global sulfur dioxide monitoring network, the Ozone Monitoring Instrument (OMI) and the Ozone Mapping Profiler Suite (OMPS) (NASA, 2016), the increased sensitivity of ASTER to lower SO_2 concentrations is evident (Figure 4-14). In fact, for the SO_2 plume on June 2, 2015 (Figure 4-14A) both OMI and

OMPS data, captured on the same day as ASTER, detect only minimal amounts of SO_2 (Figure 4-14B&C). A lower concentration of SO_2 over a smaller area is easily detected using the high spatial resolution ASTER TIR data compared to OMI and OMPS. This enables ASTER to detect much smaller plumes at much lower SO_2 concentrations (i.e., passive degassing) that are typically produced during the precursory phase.

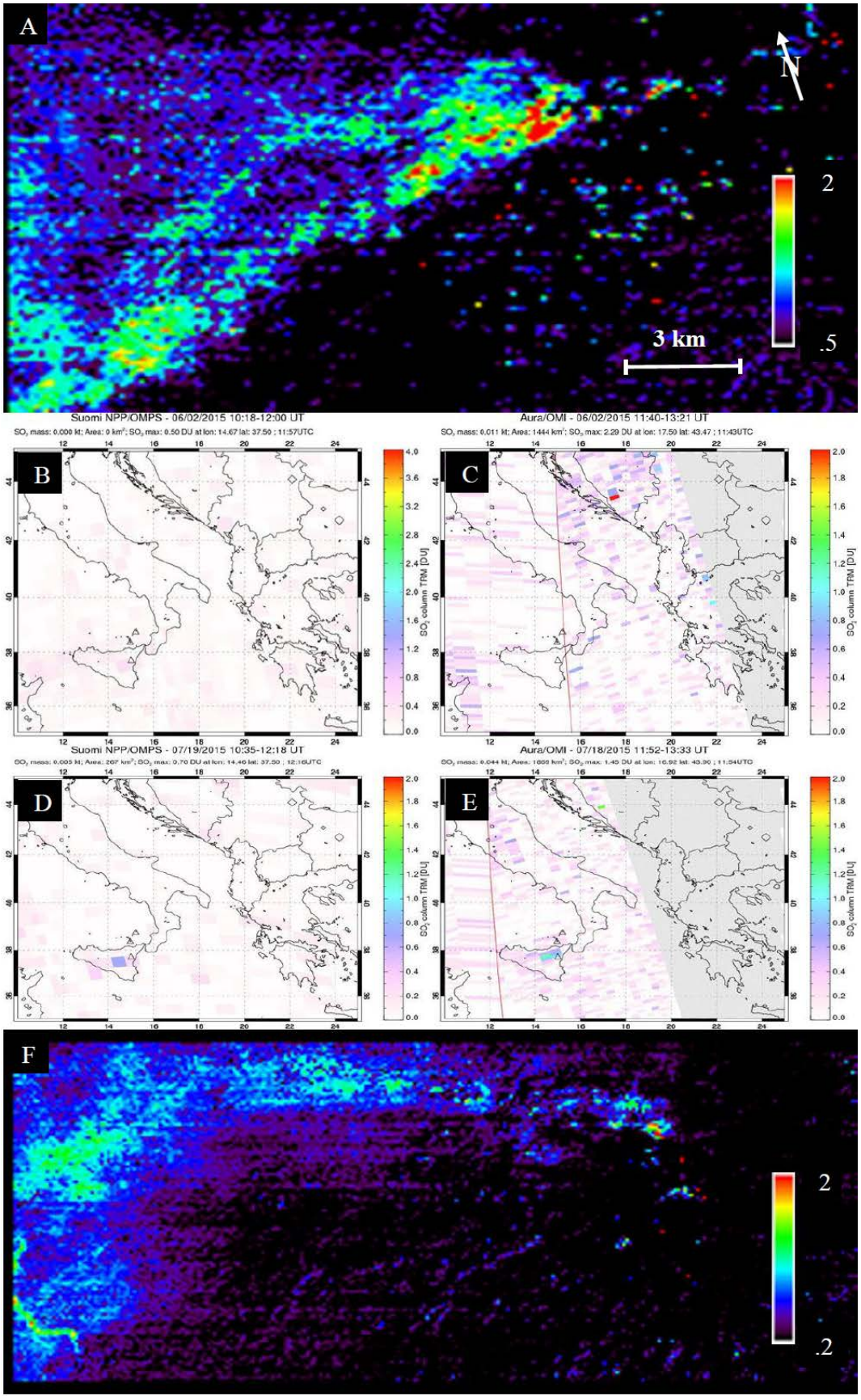
A
N
2
.5
3 km
Suomi NPP/OMPS - 06/02/2015 10:18-12:00 UT
Aura/OMI - 06/02/2015 11:40-13:21 UT
B
C
Suomi NPP/OMPS - 07/19/2015 10:35-12:18 UT
Aura/OMI - 07/18/2015 11:52-13:33 UT
D
E
F
2
.2

Figure 4-14: SO_2 concentrations from three different sensors, (A&F) ASTER, (B&D) OMPS, (C&E) OMI. ASTER images were captured over Mt Etna on (A) June 2, 2015 09:54 UTC and (F) June 20, 2015 09:54 UTC. Additionally, ASTER images are measuring concentration whereas OMPS and OMI images are measuring column thickness. Figures B-E were modified from NASA (2016).

4.4.2. Sources of error

4.4.2.1. Night and Winter Scenes

Numerous nighttime and winter scenes were analyzed, however a significant percentage of these failed to produce meaningful results. The sources of error for both of these acquisition states are related to the thermal contrast between the ground and the plume. Where this contrast is reduced, SO_2 emissions become much harder to detect. Typically, the height of the plume will produce temperatures much colder than the surface. Furthermore, snow accumulation in the winter at/near the summit, as seen in Figure 4-3 (Etna) and Figure 4-11 and Figure 4-12 (Kliuchevskoi), further lowers the surface temperature to near that of the plume and thus the sensitivity of PlumeTracker to detect SO_2. Many winter and nighttime ASTER scenes were of limited use for this study.

Etna is a well-documented emitter of a consistent passive SO_2 plume. However, as seen in Figure 4-5, no SO_2 is detected despite the clear resolution of many other surface features. In fact, in some cases at both Etna and Hawaii, a plume can be seen in the nighttime data but no SO_2 is detected (Figure 4-9). It is possible that this lack of detectable SO_2 is related to gas scrubbing from a groundwater source, which would reduce SO_2 emissions and produce a more water vapor rich plume (Symonds et al, 2001). However, this is not likely because SO_2 is detected in the daytime data acquired within the same time period. A more likely cause of this lack of

detection is the low thermal contrast. In some cases, however (e.g., Figure 4-5 and Figure 4-8), SO_2 plumes are detected in nighttime ASTER data with low thermal contrast (e.g., less than a 1°C difference between the plume and the surface). In each of these cases, the scene was either captured shortly before or during an eruption. During these periods the amount of SO_2 should generally be much larger than typical concentrations that arise during passive degassing phases. The SO_2 concentrations detected in these nighttime scenes are therefore at levels high enough to overcome the lack of thermal contrast.

4.4.2.2. Emissivity Artifacts

Emissivity artifacts can also cause the misidentification of SO_2 by PlumeTracker. This complication is present in both the Kilauea and Kliuchevskoi data. In a scene collected on May 26, 2009, a potential SO_2 cloud was identified south of Kliuchevskoi (Figure 4-15). However, further data analysis revealed this detection to be the result of a surface emissivity absorption. An emissivity artifact, in this case related to ground spectra, can produce absorption features at any wavelength, including B14 which is at a wavelength that does not contain the SO_2 absorption feature. This modeling misidentification (Figure 4-15) is likely caused by the presence of basalt surrounded by snow, which possesses a relatively flat spectrum. In contrast to the surrounding area, the basalt has a greater amount of adsorption in the 8.6μm and is therefore misidentified as being SO_2. A very similar problem occurs in every scene captured over Kilauea (Figure 4-7, Figure *4-8*, Figure *4-9*), where the most recent basaltic flows to the south of Halemuamua crater are misidentified as containing SO_2. These flows have a slightly deeper absorption feature at

9.1µm (B12) compared to the surrounding flows, which is misidentified as SO_2. However, this complication is easily identified by examining these regions in either the VNIR or TIR images following the PlumeTracker anaylsis.

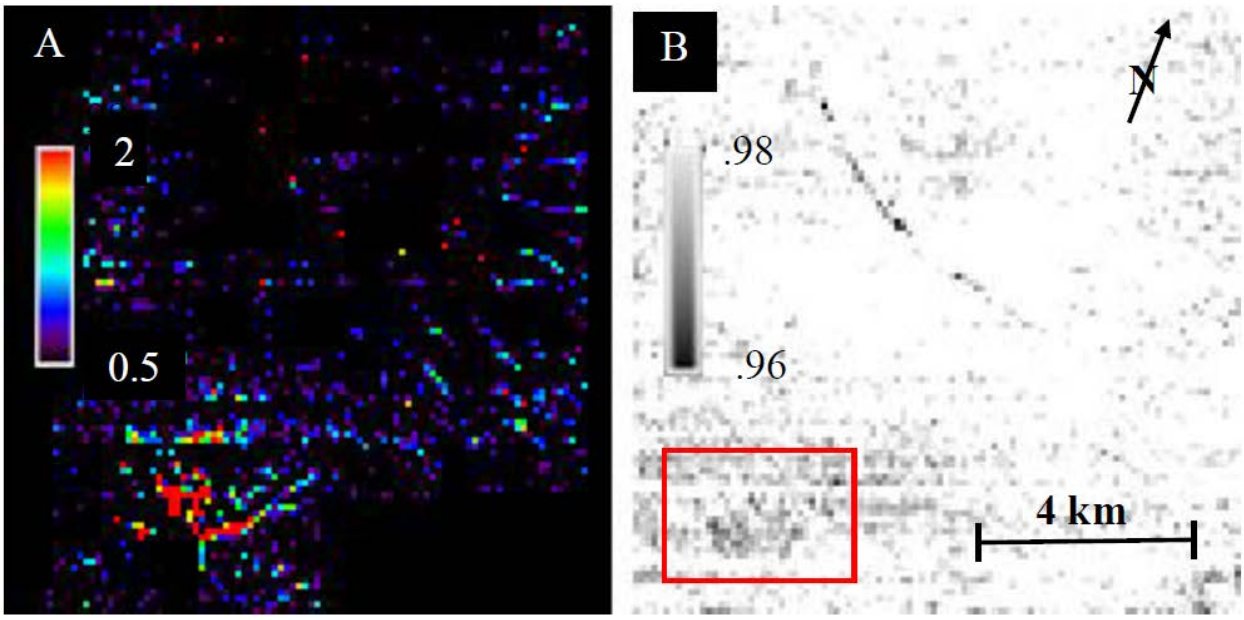

Figure 4-15: Image modified from the ASTER scene acquired May 26, 2009 00:32 UTC. (A) SO2 concentration map with values in g/m^2 and (B) emissivity values in B14 with a red box indicating the area with an emissivity anomaly corresponding to the area of high SO_2.

4.4.2.3. Shadows

Figure 4-11 and Figure *4-12* reveal shadowed areas where SO_2 is detected. These shadows, however, should have no effect on the pixel's derived emissivity. Shadows do produce a lower albedo in VNIR and cooler surface temperature in TIR. However, because SO_2 concentrations are modeled using the emissivity data, the presence of shadows would potentially only impact the model if they cause thermally-mixed pixels (e.g., shadowed plus non shadowed areas within one pixel). In such cases, an emissivity artifact can result that is commonly manifest as a lowering of

the emissivity at longer wavelengths (Rose et al, 2014). This source of error was considered as a possible cause of the SO_2 concentrations detected in the July 4, 2009 Kliuchevskoi scene (Figure 4-12). However, the pixels with high SO_2 model concentrations had no apparent spectral distortions due to thermal-mixing (Figure 4-16).

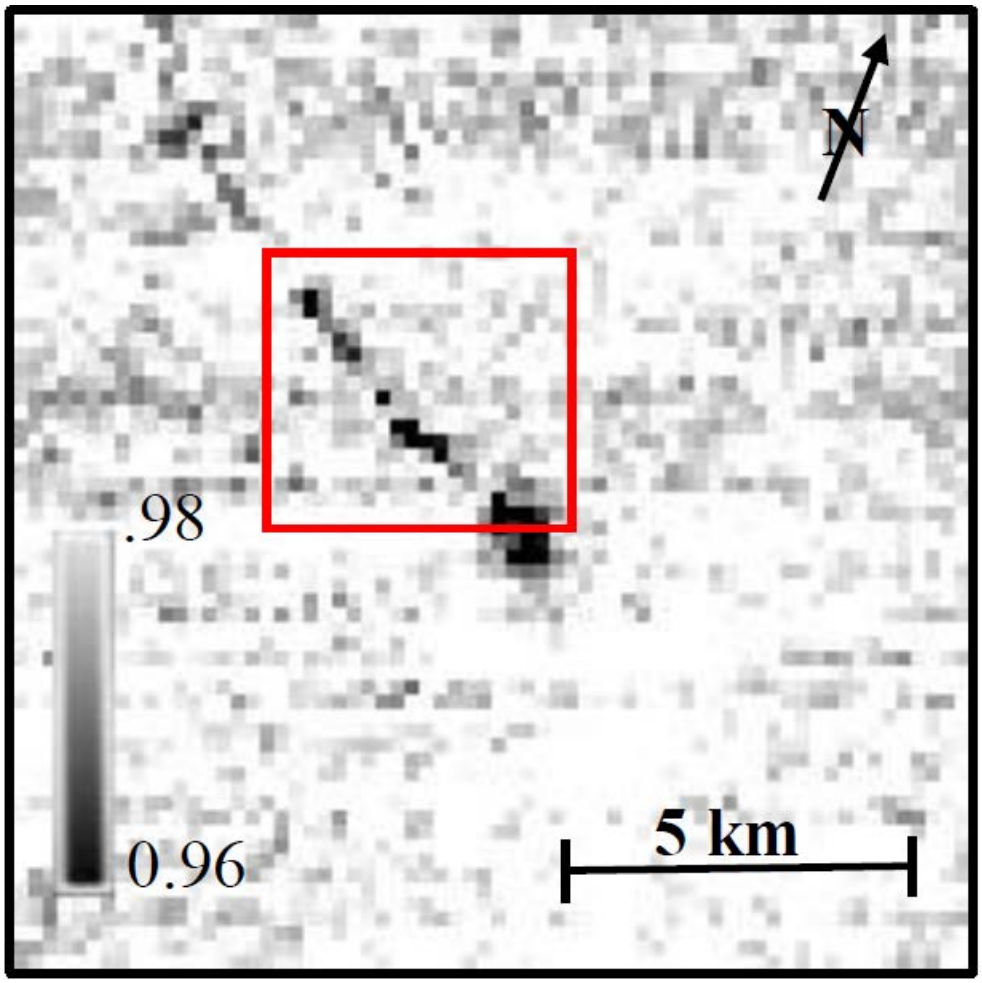

Figure 4-16: Image modified from the ASTER TIR scene acquired July 4, 2009 00:38 UTC (see Figure 4-12). Values are the emissivity in B14 with a red box indicating the area where SO_2 emissions were positively identified. No distinct absorption features are seen that correlate with the area rich SO_2 emissions in Figure 4-12D.

4.4.3. Etna Interpretations

No ASTER daytime data were acquired for approximately 4 months before the 2015 eruption of Etna, however interpretations can still be made from the entire ASTER dataset (Figure 4-4). The expected pre-eruption increase in SO_2 emissions was detected, to a limited extent, in nighttime data. Furthermore, an increase in SO_2 was positively identified before and during the series of strombolian eruptions reported in early May 2015. The combination of these two factors leads to the conclusion that if daytime ASTER data were collected within the 2 month period prior the eruption, an increase in SO_2 concentrations would have been observed. It may also be assumed that the increased sensitivity of ASTER data compared to the current low spatial resolution SO_2 monitoring sensors (Figure 4-14) would have allowed the first detections with the ASTER data. Therefore, when available, ASTER data processed using PlumeTracker should be able to identify early precursory SO_2 activity. Such a result would greatly increase the current monitoring and warning systems in place at Etna.

4.4.4. Kilauea Interpretations

Much like the period before the eruption of Etna, no daytime ASTER data were collected before the 2008 eruption. However, ground-based SO_2 flux was measured at Halemaumau crater by HVO and this increase was seen from early January until the eruption on March 19, 2008 (Figure 4-10). The SO_2 rate recorded using ground-based sensors can be related to the SO_2 detection limits of the approach presented here. Ground-based daily SO_2 data are not available until January 1, 2008. During this period, SO_2 plumes modeled using the PlumeTracker approach are difficult to distinguish from background noise, however an average of approximately 1.5kg of SO_2

emissions are detectable. On March 23, 2008 both daytime ASTER data and historic SO_2 concentration data collected downwind of Halemaumau crater are available (Pahala Vog, 2016). Ground data recorded concentrations of 0.182 g/m^3 on March 23rd and the PlumeTracker modeled ASTER data produced average concentrations of 2.727 g/m^2 within the plume. These two concentrations nearly agree for an assumed plume thickness of 15m. On April 17, 2008 a SO_2 plume was detected in ASTER night data and with ground based monitoring. On this occasion the ground station recorded concentrations of 0.536 g/m^3 whereas the ASTER result was 0.909 g/m^2. A plume with an average thickness of less than 2m would produce similar values. Such a thin plume is unlikely and therefore the modeled nighttime concentrations are underestimated. In the daytime data, the edges of the plume can be differentiated from background surface emissivity. In nighttime data, however, as concentrations decrease near the plume edges, they become undetectable. This, in conjunction with the lower thermal contrast at night, causes the plume to gradually disappear at its edges and makes it appear diffuse.

4.4.5. Kliuchevskoi Interpretations

Of the four scenes acquired in 2009 and analyzed for SO_2, three were acquired from April 6 to May 26, 2009 and showed little to no detectable SO_2 (Figure 4-13). These data could indicate that during this period, degassing rates were very low. Alternately, this could be the result of precursory volcanic activity. The thermal data from Reath et al., (2016, submitted) combined with these SO_2 data, have been interpreted to suggest that strombolian eruptions were the dominate volcanic activity during this phase. Iguchi et al, (2008) found that during a period of strombolian

eruptions, volcanic gas will coalesce within the conduit or magma chamber rather than passively degassing. These gases eventually reach the surface, causing a strombolian eruption. Generally, SO_2 emissions become quite sporadic and dependent on the occurrence rate of the strombolian eruptions. Worden et al (2014) demonstrate that a temporal resolution of at least 5 overpasses per day is needed in order to acquire an image within 1 minute on average of a strombolian eruption. This, coupled with the low temporal rate of ASTER scenes, means that capturing a specific SO_2 plume during (or soon after) a strombolian eruption would be extremely unlikely.

The ASTER scene captured on July 4 resulted in 71.2kg of total modeled instantaneous SO_2. This scene occurs during Phase III of the eruption where the manga column has been interpreted to have ascended in the conduit (Reath, et al., 2016, submitted). In this case, infusion of juvenile material into the magma plumbing system caused the magma to rise in the conduit, decreased the strombolian eruptions, and produced increased rates of SO_2 degassing. This degassing would account for the large amount of SO_2 found in this scene.

4.5. Conclusions

A quantitative value for SO_2 can be remotely detected in satellite TIR data using the tools available in PlumeTracker. These results can then be used to detect changes in gas flux over time, which commonly results from several types of precursory activity prior to an eruption. The limited temporal resolution of the ASTER sensor presents difficulties in interpreting these precursory time periods. In some cases, the infrequent revisit time combined with the presence of clouds prevents detection of an increase of SO_2 emissions commonly associated with the influx of new

magma. However, the increase in SO_2 detection sensitivity for ASTER TIR data compared to the sensors currently used for SO_2 monitoring (e.g., OMI, OMPS), allows the period of SO_2 detection to be greatly extended. Additionally, this increase in sensitivity allows comparison of SO_2 to other possible precursory datasets such as temperature.

In this study, SO_2 was directly compared to thermal flux at Kliuchevskoi. These data suggest that the different thermal phases as classified by Reath et al., (2016, submitted) correlate well with variations in SO_2 degassing rates. This also corresponds with degassing behavior observed in laboratory experiments performed by Jaupart and Vergniolle, (1998). In Phase II of the eruption where strombolian activity dominates, measured degassing rates are low as would be expected due to the gas coalescence into a slug. This behavior was observed at both Kliuchevskoi (this study) as well as in precursory activity documented at Etna by Caltabiano et al., (1994) and on Suwanosejima and Semeru by Iguchi et al., (2008). In the final phase of precursory activity (Phase III), an increase in both thermal flux and degassing are observed. This generally supports typical precursory activity collected from both Etna and Hawaii (e.g. Caltabiano et al., 1994; Daag et al., 1996; Edmonds et al., 2003; Werner et al., 2011).

The data presented in this study from these three volcanoes demonstrate the potential of high spatial resolution TIR data (like ASTER) to detect volcanic precursors and the volcanic processes that can be related to pre-eruptive activity. With the proposed next generation of high temporal/high spatial resolution sensors, these modeling and monitoring methods will improve in accuracy and possibly become as important as other real-time ground-based monitoring tools.

4.6. Acknowledgements

Funding for this research was made possible by NASA under the Science of Terra and Aqua Research Program (NNX11AL29G) and the ASTER Science Team. The research presented here would also not have been possible without software programs made available through NASA and JPL.

5. CLOSING REMARKS

As demonstrated in this research, the modeling and data analysis methods rely on accurate thermal infrared (TIR) orbital data to derive various precursory activities at active volcanoes around the world. High temporal/low spatial resolution TIR data (e.g., AVHRR and MODIS) are combined with low temporal/high spatial resolution data (e.g., ASTER) to improve time series analysis and provide points of comparison. It is clear, however, that a sensor like ASTER with high spatial resolution TIR data is most effective at detection of small-scale subtle activity, which is critical to understand in order to forecast future eruptions. ASTER has long outlived its intended life span by over a decade, creating concern about its future. Even with the inevitable end of life of ASTER, the methods presented here are no less significant and directly applicable to any future TIR sensor with similar designed parameters as ASTER. For example, the specifications for the proposed improvements upon ASTER by the HyspIRI sensor in spectral, spatial, and temporal resolution would make it superior for volcanic monitoring and eruption forecasting. This would increase the effectivity of each of these methods, which can be used to produce a greater understanding of the processes that occur before and during an eruption.

Whereas chapter 2 provided a method to remotely determine pyroclastic volumes, the methodology is time-intensive. In the future, an approach such as this could be easily streamlined and programmed in order to make it consistently reproducible at many volcanoes on a near-real time basis. For example, the cooling rate of a pyroclastic flow could be resolved as quickly as the time it takes for a minimum of three clear images are acquired. Deriving the composition of the flow from the TIR emissivity data could also be automated and then used to estimate the internal

stratigraphy, the percentage of the flow with isothermal cooling and uniform thickness, as well as the total area of the flow, which would then yield a modeled flow volume after each eruption.

Chapters 3 and 4 demonstrated the utility of using ASTER TIR data during the precursory period. In chapter 3, an approach to observe, analyze, and classify precursory thermal flux into the existing monitoring network was demonstrated. In chapter 4, a modeling-based approach of TIR data to estimate SO_2 concentration was shown. Currently, producing ASTER SO_2 concentration maps requires a large amount of pre-processing time and effort, relying on certain model-based assumptions. Similar to the approach in chapter 2, if data acquisition and preprocessing could be reduced and automated, these methods could then be integrated into existing monitoring networks around the world, including locations where lack of funds preclude ground-based SO_2 monitoring instruments.

In summary, the analysis approaches and results should be expanded to more volcanoes and eruptions in order to validate and expand the catalog of thermal and degassing precursory indicators. This would clarify how the classifications and patterns produced by this research can be universally applied to eruptions at other volcanoes. Additionally, these results should be compared with direct and in situ monitoring data such as seismic and deformation recorded during the precursory period. This multi-technique approach would provide a complete analysis of the volcanic activity occurring before an eruption and establish a quantitative baseline for forecasting future eruptions.

6. BIBLIOGRAPHY

Abrams, M., 2000. The Advanced Spaceborne Thermal Emission and Reflection Radiometer (ASTER): data products for the high spatial resolution imager on NASA's Terra platform. Int. J. Remote Sens. 21 (5), 847–859

Aiuppa, A., Inguaggiato, S., McGonigle, A. J. S., O'dwyer, M., Oppenheimer, C., Padgett, M. J., ... & Valenza, M. (2005). H 2 S fluxes from Mt. Etna, Stromboli, and Vulcano (Italy) and implications for the sulfur budget at volcanoes. Geochimica et Cosmochimica Acta, 69(7), 1861-1871.

Andres, R. J., Kyle, P. R., Stokes, J. B., & Rose, W. I. (1989). SO2 from episode 48A eruption, Hawaii: sulfur dioxide emissions from the episode 48A East Rift zone eruption of Kilauea Volcano, Hawaii. Bulletin of volcanology, 52(2), 113-117.

Andres, R. J., & Rose, W. I. (1995). Remote sensing spectroscopy of volcanic plumes and clouds. Monitoring active volcanoes: strategies, procedures and techniques, 301-314.

Arya, S. P. (1988). Introduction to MicrometeorologyAcademic Press. San Diego.

Bailey, J. E., Dean, K. G., Dehn, J., & Webley, P. W. (2010). Integrated satellite observations of the 2006 eruption of Augustine Volcano (No. 1769-20). US Geological Survey.

Beil, A., Daum, R., Harig, R., & Matz, G. (1998, October). Remote sensing of atmospheric pollution by passive FTIR spectrometry. In Remote Sensing (pp. 32-43). International Society for Optics and Photonics.

Belousov, A. B. (1995). The Shiveluch volcanic eruption of 12 November 1964—explosive eruption provoked by failure of the edifice. *Journal of Volcanology and Geothermal Research*, *66*(1), 357-365.

Belousov, A., Belousova, M., & Voight, B. (1999). Multiple edifice failures, debris avalanches and associated eruptions in the Holocene history of Shiveluch volcano, Kamchatka, Russia. *Bulletin of Volcanology*, *61*(5), 324-342.

Bernstein, M., Pavez, A., Varley, N., Whelley, P., & Calder, E. (2013). Rhyolite lava dome growth styles at Chaitén Volcano, Chile (2008-2009): Interpretation of thermal imagery. Andean Geology, 40(2), 295-309.

Berresheim, H., & Jaeschke, W. (1983). The contribution of volcanoes to the global atmospheric sulfur budget. Journal of Geophysical Research: Oceans, 88(C6), 3732-3740.

Blackburn EA, Wilson L, Sparks RSJ (1976) Mechanisms and dynamics of strombolian activity. J Geol Soc London 132:429–440

Bluth, G. J., Doiron, S. D., Schnetzler, C. C., Krueger, A. J., & Walter, L. S. (1992). Global tracking of the SO2 clouds from the June, 1991 Mount Pinatubo eruptions. *Geophysical Research Letters*, *19*(2), 151-154.

Bluth, G. J., Rose, W. I., Sprod, I. E., & Krueger, A. J. (1997). Stratospheric loading of sulfur from explosive volcanic eruptions. The Journal of Geology, 105(6), 671-684.

Booth B, Walker GPL (1973) Ash deposits from the new explosion crater, Etna 1971. Phil Trans R Soc London A274:147–161

Braitseva, O. A., Melekestsev, I. V., Ponomareva, V. V., & Sulerzhitsky, L. D. (1995). Ages of calderas, large explosive craters and active volcanoes in the Kuril-Kamchatka region, Russia. Bulletin of Volcanology, 57(6), 383-402.

Bruno, N., Caltabiano, T., & Romano, R. (1999). SO2 emissions at Mt. Etna with particular reference to the period 1993–1995. Bulletin of Volcanology, 60(6), 405-411.

Calder, E. S., Cole, P. D., Dade, W. B., Druitt, T. H., Hoblitt, R. P., Huppert, H. E., ... & Young, S. R. (1999). Mobility of pyroclastic flows and surges at the Soufriere Hills Volcano, Montserrat. Geophysical Research Letters, 26(5), 537-540.

Calder, E. S., Luckett, R., Sparks, R. S. J., & Voight, B. (2002). Mechanisms of lava dome instability and generation of rockfalls and pyroclastic flows at Soufriere Hills Volcano, Montserrat. Geological Society, London, Memoirs, 21(1), 173-190.

Caltabiano, T., Romano, R., & Budetta, G. (1994). SO2 flux measurements at Mount Etna (Sicily). Journal of Geophysical Research: Atmospheres (1984–2012), 99(D6), 12809-12819.

Calvari S, Pinkerton H (2004) Birth, growth and morphologic evolution of the “Laghetto” cinder cone during the 2001 Etna eruption. J Volcanol Geotherm Res 132:225–239

Campion, R., Salerno, G. G., Coheur, P. F., Hurtmans, D., Clarisse, L., Kazahaya, K., ... & Bernard, A. (2010). Measuring volcanic degassing of SO 2 in the lower troposphere with ASTER band ratios. Journal of volcanology and geothermal research, 194(1), 42-54.

Campion, R., Martinez-Cruz, M., Lecocq, T., Caudron, C., Pacheco, J., Pinardi, G., ... & Bernard, A. (2012). Space-and ground-based measurements of sulphur dioxide emissions from Turrialba Volcano (Costa Rica). Bulletin of volcanology, 74(7), 1757-1770.

Carn, S. A., Krotkov, N. A., Yang, K., Hoff, R. M., Prata, A. J., Krueger, A. J., ... & Levelt, P. F. (2007). Extended observations of volcanic SO 2 and sulfate aerosol in the stratosphere. *Atmospheric Chemistry and Physics Discussions*, *7*(1), 2857-2871.

Carn, S. A., Sutton, A. J., Elias, T., Patrick, M. R., Owen, R. C., & Wu, S. (2009, December). Satellite measurements of SO2 emission and dispersion during the 2008-2009 eruption of Halemaumau, Kilauea. In AGU Fall Meeting Abstracts (Vol. 1, p. 07).

Carter, A. J., Girina, O., Ramsey, M. S., & Demyanchuk, Y. V. (2008). ASTER and field observations of the 24 December 2006 eruption of Bezymianny Volcano, Russia. Remote Sensing of Environment, 112(5), 2569-2577.

Carter, A. J., & Ramsey, M. S. (2009). ASTER-and field-based observations at Bezymianny Volcano: Focus on the 11 May 2007 pyroclastic flow deposit. Remote Sensing of Environment, 113(10), 2142-2151.

Carter, A., & Ramsey, M. (2010). Long-term volcanic activity at Shiveluch Volcano: Nine years of ASTER spaceborne thermal infrared observations. Remote Sensing, 2(11), 2571-2583.

Casadevall, T. J. (1993). Volcanic ash and airports: discussion and recommendations from the workshop on impacts of volcanic ash on airport facilities. US Geological Survey Open-File Report, 93, 518.

Casadevall, T. J., Johnston, D. A., Harris, D. M., Rose, W. I., Malinconico, L. L., Stoiber, R. E., ... & Thompson, J. M. (1981). SO2 emission rates at Mount St. Helens from March 29 through December, 1980. US Geol Surv Prof Pap, 1250, 193-200.

Charbonnier, S. J., & Gertisser, R. (2008). Field observations and surface characteristics of pristine block-and-ash flow deposits from the 2006 eruption of Merapi Volcano, Java, Indonesia. Journal of Volcanology and Geothermal Research, 177(4), 971-982.

Chouet B, Hamisevicz N, McGetchin TR (1974) Photoballistics of volcanic jet activity at Stromboli, Italy. J Geophys Res 79:4961– 4976

Chouet B, Saccorotti G, Dawson P, Martini M, Scarpa R, De Luca G, Milana G, Cattaneo M (1999) Broadband measurements of the sources of explosions at Stromboli volcano. Geophys Res Lett 26:1937–1940

Clarisse, L., Hurtmans, D., Clerbaux, C., Hadji-Lazaro, J., Ngadi, Y., & Coheur, P. F. (2012). Retrieval of sulphur dioxide from the infrared atmospheric sounding interferometer (IASI). Atmospheric Measurement Techniques, 5(3), 581-594.

Clarke, A. B., Voight, B., Neri, A., & Macedonio, G. (2002). Transient dynamics of vulcanian explosions and column collapse. Nature, 415(6874), 897-901.

Cole, P. D., Calder, E. S., Druitt, T. H., Hoblitt, R., Robertson, R., Sparks, R. S. J., & Young, S. R. (1998). Pyroclastic flows generated by gravitational instability of the 1996–97 lava dome of Soufriere Hills Volcano, Montserrat. Geophysical Research Letters, 25(18), 3425-3428.

Cole, P. D., Calder, E. S., Sparks, R. S. J., Clarke, A. B., Druitt, T. H., Young, S. R., ... & Norton, G. E. (2002). Deposits from dome-collapse and fountain-collapse pyroclastic flows at Soufrière Hills Volcano, Montserrat. Geological Society, London, Memoirs, 21(1), 231-262.

Daag, A. S., Tubianosa, B. S., Newhall, C. G., Tungol, N. M., Javier, D., Dolan, M. T., ... & Regalado, T. M. (1996). Monitoring sulfur dioxide emission at Mount Pinatubo. Fire and Mud: eruptions and lahars of Mount Pinatubo, Philippines, 409-414.

Dean, K., Servilla, M., Roach, A., Foster, B., & Engle, K. (1998). Satellite monitoring of remote volcanoes improves study efforts in Alaska. Eos, Transactions American Geophysical Union, 79(35), 413-423.

Dehn J, Dean KG, Engle K (2000) Thermal monitoring of North Pacific volcanoes from space. Geology 28:755–758

Dehn, J., Dean, K. G., Engle, K., & Izbekov, P. (2002). Thermal precursors in satellite images of the 1999 eruption of Shishaldin Volcano. Bulletin of Volcanology, 64(8), 525-534.

Dehn, J., and Harris, A. J. L., 2015. Thermal anomalies at volcanoes, Chapter 3 in Volcanoes of the North Pacific: Observations from Space. eds. Ken Dean and Jonathan Dehn. In Press.

Delgado-Granados, H., González, L. C., & Sánchez, N. P. (2001). Sulfur dioxide emissions from Popocatépetl volcano (Mexico): case study of a high-emission rate, passively degassing erupting volcano. Journal of Volcanology and Geothermal Research, 108(1), 107-120.

Dirksen, O.; Humphreys, M.C.S.; Pletchov, P.; Melnik O.; Demyanchuk Y., Sparks, R.S.J.; Mahony S. (2006) The 2001–2004 dome-forming eruption of Shiveluch volcano, Kamchatka: Observation, petrological investigation and numerical modeling. J. Volcanol. Geotherm. Res., 155, 201-226.

Druitt, T. H. (1998). Pyroclastic density currents. Geological Society, London, Special Publications, 145(1), 145-182.

Duda, K. A., Ramsey, M., Wessels, R., & Dehn, J. (2009). Optical satellite volcano monitoring: A multi-sensor rapid response system.

Dzurisin, D., Lisowski, M., Poland, M. P., Sherrod, D. R., & LaHusen, R. G. (2008). Constraints and conundrums resulting from ground-deformation measurements made during the 2004-2005 dome-building eruption of Mount St. Helens, Washington. US Geological Survey professional paper, (1750), 281-300.

Edmonds M, Herd RA, Galle B, Oppenheimer CM (2003) Automated high time resolution measurements of SO2 flux at Soufriere Hills Volcano, Montserrat. Bull Volcanol 65:578–586

Edmonds, M., Sides, I. R., Swanson, D. A., Werner, C., Martin, R. S., Mather, T. A., ... & Roberts, T. J. (2013). Magma storage, transport and degassing during the 2008–10 summit eruption at Kīlauea Volcano, Hawai ‘i. Geochimica et Cosmochimica Acta, 123, 284-301.

Edwards, B., Belousov, A., Belousova, M., Volynets, A., Melnikov, D., Chirkov, S., Senyukov, S.& Demianchuk, Y. (2013). Another “Great Tolbachik” Eruption?. Eos, Transactions American Geophysical Union, 94(21), 189-191.

Fearnley, C. J., McGuire, W. J., Davies, G., & Twigg, J. (2012). Standardisation of the USGS Volcano Alert Level System (VALS): analysis and ramifications. Bulletin of volcanology, 74(9), 2023-2036.

Fedotov, S. A. (1984). The great Tolbachinsk fissure eruption-Kamchatka 1975-1976. Moscow Izdatel Nauka, 1.

Fedotov, S.A.; Masurenkov, Yu.P. (1991) Active Volcanoes of Kamchatka; Nauka: Moscow, Russia, Volume 1; pp. 168–197.

Fedotov, S.A., Khrenov, A.P., Zharinov, N.A., 1987. Klyuchevskoy Volcano, its activity in 1952–1986 and possible evolution. Volcanology and Seismology 6, 3–17 (in Russian).

Fisher, R. V. (1979). Models for pyroclastic surges and pyroclastic flows .*Journal of Volcanology and Geothermal Research*, *6*(3), 305-318.

Francis P (1993) Volcanoes—a planetary perspective. Oxford University Press, Oxford

Francis, P., Maciejewski, A., Oppenheimer, C., Chaffin, C., & Caltabiano, T. (1995). SO2: HCl ratios in the plumes from Mt. Etna and Vulcano determined by Fourier Transform Spectroscopy. Geophysical Research Letters, 22(13), 1717-1720.

Francis, P. W., & Rothery, D. A. (1987). Using the Landsat Thematic Mapper to detect and monitor active volcanoes: An example from Lascar volcano, northern Chile. Geology, 15(7), 614-617.

Freymueller, J. T., LaHusen, R. G., McGee, K. A., Poland, M. P., Power, J. A., Schmidt, D. A., ... & White, R. A. (2008). Instrumentation recommendations for volcano monitoring at US volcanoes under the National Volcano Early Warning System. US Geological Survey.

Gerlach, T. M., McGee, K. A., Sutton, A. J., & Elias, T. (1998). Rates of volcanic CO2 degassing from airborne determinations of SO2 Emission rates and plume CO2/SO2: test study at Pu' u' O' o Cone, Kilauea Volcano, Hawaii. Geophysical research letters, 25(14), 2675-2678.

Gillespie, A.R., 1985. Lithologic mapping of silicate rocks using TIMS. The TIMSData User's Workshop, June 18-19, 1985, JPL Pub. 86-38, pp. 29–44.

Gillespie, A. R., Kahle, A. B., & Walker, R. E. (1986). Color enhancement of highly correlated images. I. Decorrelation and HSI contrast stretches. Remote Sensing of Environment, 20(3), 209-235.

Gillespie, A., Rokugawa, S., Matsunaga, T., Cothern, J. S., Hook, S., & Kahle, A. B. (1998). A temperature and emissivity separation algorithm for Advanced Spaceborne Thermal Emission and Reflection Radiometer (ASTER) images. Geoscience and Remote Sensing, IEEE Transactions on, 36(4), 1113-1126.

Global Volcanism Program, 2008. Report on Kilauea (United States). In: Sennert, S K (ed.), Weekly Volcanic Activity Report, 2008. Smithsonian Institution and US Geological Survey.

Global Volcanism Program, 2010. Report on Kilauea (United States). In: Sennert, S K (ed.), Weekly Volcanic Activity Report,2008-2010. Smithsonian Institution and US Geological Survey.

Global Volcanism Program, 2013. Report on Klyuchevskoy (Russia). In: Sennert, S K (ed.), Weekly Volcanic Activity Report, 2013. Smithsonian Institution and US Geological Survey.

Global Volcanism Program, 2015. Report on Etna (Italy). In: Sennert, S K (ed.), Weekly Volcanic Activity Report, 2 December-8 December 2015. Smithsonian Institution and US Geological Survey.

Global Volcanism Program, 2009. Report on Sheveluch (Russia). In: Sennert, S K (ed.), Weekly Volcanic Activity Report, Smithsonian Institution and US Geological Survey.

Global Volcanism Program, 2011. Report on Sheveluch (Russia). In: Sennert, S K (ed.), Weekly Volcanic Activity Report, Smithsonian Institution and US Geological Survey.

Goita, K., & Royer, A. (1997). Surface temperature and emissivity separability over land surface from combined TIR and SWIR AVHRR data. Geoscience and Remote Sensing, IEEE Transactions on, 35(3), 718-733.

Gorshkov, G. S. (1959). Gigantic eruption of the volcano Bezymianny. Bulletin Volcanologique, 20(1), 77-109.

Greeley, R., & Iversen, J. D. (1987). Measurements of wind friction speeds over lava surfaces and assessment of sediment transport. Geophysical Research Letters, 14(9), 925-928.

Grishin, S. Y. (2009). Forest die-off under the impact of burning pyroclastic surge on the Shiveluch Volcano (Kamchatka, 2005). *Russian Journal of Ecology*, *40*(2), 146-148.

Grishin, S. Y. (2012). Colonizing plants on hot pyroclastic flow deposits (Shiveluch Volcano, Kamchatka). Russian Journal of Ecology, 43(2), 174-176.

Gushchenko, I.I., 1979. Eruptions of Volcanoes of the World: a Catalog. In: Academy of Science USSR Far Eastern Science Center. Nauka, Moscow, p. 474 (in Russian).

Guffanti, M., & Miller, T. P. (2013). A volcanic activity alert-level system for aviation: review of its development and application in Alaska. Natural hazards, 69(3), 1519-1533.

Kirchdorfen M (1999) Analysis and quasistatic FE modeling of long period impulsive events associated with explosions at Stromboli volcano (Italy). Ann Geophys 42:379–391

Koloskov, A. V., Gontovaya, L. I., & Popruzhenko, S. V. (2014). The upper mantle of Kamchatka in isotopic-geochemical and geophysical anomalies: The role of asthenospheric diapirism. Russian Journal of Pacific Geology, 8(3), 151-162.

Kugaenko, Y., Saltykov, V., & Titkov, N. (2014, May). Pre-eruption deformation and seismic anomalies in 2012 in Tolbachik volcanic zone, Kamchatka. In EGU General Assembly Conference Abstracts (Vol. 16, p. 4548).

Harris, A. J., Butterworth, A. L., Carlton, R. W., Downey, I., Miller, P., Navarro, P., & Rothery, D. A. (1997a). Low-cost volcano surveillance from space: case studies from Etna, Krafla, Cerro Negro, Fogo, Lascar and Erebus. Bulletin of Volcanology, 59(1), 49-64.

Harris, A. J. L., Blake, S., Rothery, D. A., & Stevens, N. F. (1997b). A chronology of the 1991 to 1993 Etna eruption using AVHRR data: implications for real time thermal volcano monitoring. J Geophys Res, 102(B4), 7985-8003.

Harris, A. J., Flynn, L. P., Keszthelyi, L., Mouginis-Mark, P. J., Rowland, S. K., & Resing, J. A. (1998). Calculation of lava effusion rates from Landsat TM data. Bulletin of Volcanology, 60(1), 52-71.

Harris, A. J. L., Flynn, L. P., Matıas, O., & Rose, W. I. (2002). The thermal stealth flows of Santiaguito dome, Guatemala: Implications for the cooling and emplacement of dacitic block-lava flows. Geological Society of America Bulletin.

Harris AJL, Wright R, Flynn LP (1999) Remote monitoring of Mount Erebus volcano, Antarctica, using polar orbiters: progress and prospects. Int J Rem Sens 20(15–16):3051–3071

Head, J. W., & Wilson, L. (1986). Volcanic processes and landforms on Venus: Theory, predictions, and observations. Journal of Geophysical Research: Solid Earth (1978–2012), 91(B9), 9407-9446.

Heiken, G. (1994). Volcanic ash: what it is and how it forms. In Volcanic Ash and Aviation Safety—Proceedings of the First International Symposium on Volcanic Ash and Aviation Safety (pp. 39-45).

Heiken, G., Casadevall, T.J., Newhall, C., 1992. First international symposium on volcanic ash and aviation safety. Bulletin of Volcanology 54 (3), 250–251.

Henney, L. A., & Watson, I. M. (2006, December). The Use of the Advanced Spacebourne Thermal Emission and Reflection Radiometer (ASTER) to Detect Sulphur Dioxide Emissions at Fuego and Pacaya Volcanoes, Guatemala. In AGU Fall Meeting Abstracts (Vol. 1, p. 1727).

Henney, L. A., Rodríguez, L. A., & Watson, I. M. (2012). A comparison of SO2 retrieval techniques using mini-UV spectrometers and ASTER imagery at Lascar volcano, Chile. Bulletin of volcanology, 74(2), 589-594.

Huggel, C., Schneider, D., Miranda, P. J., Granados, H. D., & Kääb, A. (2008). Evaluation of ASTER and SRTM DEM data for lahar modeling: a case study on lahars from Popocatépetl Volcano, Mexico. Journal of Volcanology and Geothermal Research, 170(1), 99-110

Huppert, H. E., Shepherd, J. B., Sigurdsson, R. H., & Sparks, S. J. (1982). On lava dome growth, with application to the 1979 lava extrusion of the Soufriere of St. Vincent. Journal of Volcanology and Geothermal Research, 14(3), 199-222.

IGBP, 1992, Improved Global Data for Land Applications, edited by J. R. G. Townshend. IGBP Global Change Report No. 20, InternationalGeosphere–Biosphere Programme, Stockholm, Sweden.

Iguchi, M., Yakiwara, H., Tameguri, T., Hendrasto, M., & Hirabayashi, J. I. (2008). Mechanism of explosive eruption revealed by geophysical observations at the Sakurajima, Suwanosejima and Semeru volcanoes. Journal of Volcanology and Geothermal Research, 178(1), 1-9.

Inguaggiato, S., Vita, F., Rouwet, D., Bobrowski, N., Morici, S., & Sollami, A. (2011). Geochemical evidence of the renewal of volcanic activity inferred from CO2 soil and SO2 plume fluxes: the 2007 Stromboli eruption (Italy). Bulletin of volcanology, 73(4), 443-456.

Jaupart, C., & Vergniolle, S. (1988). Laboratory models of Hawaiian and Strombolian eruptions. Nature, 331(6151), 58-60.

Jiang, G., Zhao, D., & Zhang, G. (2009). Seismic tomography of the Pacific slab edge under Kamchatka. Tectonophysics, 465(1), 190-203.

Justice, C. O., Townshend, J. R. G., Holben, B. N., & Tucker, E. C. (1985). Analysis of the phenology of global vegetation using meteorological satellite data. International Journal of Remote Sensing, 6(8), 1271-1318.

Kazahaya, K., Shinohara, H., Uto, K., Odai, M., Nakahori, Y., Mori, H., ... & Hirabayashi, J. (2004). Gigantic SO2 emission from Miyakejima volcano, Japan, caused by caldera collapse. Geology, 32(5), 425-428.

Kearney, C., Dehn, J., & Dean, K. (2004, December). Space-based TIR detection of volcanic SO2 in the North Pacific using ASTER and MODIS. In AGU Fall Meeting Abstracts (Vol. 1, p. 1477).

Krueger, A. J. (1983). Nimbus 7 total ozone mapping spectrometer (TOMS) data during the Gap, France, ozone intercomparisons of June 1981. Planetary and Space Science, 31(7), 773-777.

Krueger, A. J., Walter, L. S., Schnetzler, C. C., & Doiron, S. D. (1990). TOMS measurement of the sulfur dioxide emitted during the 1985 Nevado del Ruiz eruptions. Journal of Volcanology and Geothermal Research, 41(1), 7-15.

Kyle, P. R., Sybeldon, L. M., Mcintosh, W. C., Meeker, K., & Symonds, R. (1994). Sulfur dioxide emission rates from Mount Erebus, Antarctica. Volcanological and environmental studies of Mount Erebus, Antarctica, 69-82.

KVERT: Active Volcanoes of Kamchatka and Northern Kuriles, Shiveluch. (2009). 6/4/2015, http://www.kscnet.ru/ivs/kvert/volc.php?name=Sheveluch&lang=en

Lee, C. M., Cable, M. L., Hook, S. J., Green, R. O., Ustin, S. L., Mandl, D. J., & Middleton, E. M. (2015). An introduction to the NASA Hyperspectral InfraRed Imager (HyspIRI) mission and preparatory activities. Remote Sensing of Environment, 167, 6-19.

Macdonald GA (1972) Volcanoes. Prentice-Hall, Englewood Cliffs, NJ

Malinconico, L. L. (1979). Fluctuations in SO2 emission during recent eruptions of Etna. Nature, 278, 43-45.

Marchese, F., Falconieri, A., Pergola, N., & Tramutoli, V. (2014). A retrospective analysis of the Shinmoedake (Japan) eruption of 26–27 January 2011 by means of Japanese geostationary satellite data. Journal of Volcanology and Geothermal Research, 269, 1-13.

McGonigle, A. J. S., Oppenheimer, C., Galle, B., Mather, T. A., & Pyle, D. M. (2002). Walking traverse and scanning DOAS measurements of volcanic gas emission rates. Geophysical Research Letters, 29(20), 46-1.

McGonigle, A. J. S., Oppenheimer, C., Hayes, A. R., Galle, B., Edmonds, M., Caltabiano, T., ... & Mather, T. A. (2003). Sulphur dioxide fluxes from Mount Etna, Vulcano, and Stromboli measured with an automated scanning ultraviolet spectrometer. Journal of Geophysical Research: Solid Earth (1978–2012), 108(B9).

Menyailov, I. A. (1975). Prediction of eruptions using changes in composition of volcanic gases. Bulletin Volcanologique, 39(1), 112-125.

Miller, T. P., & Casadevall, T. J. (2000). Volcanic ash hazards to aviation. Encyclopedia of volcanoes, 915-930.

Moffat, A. J., and M. M. Millfin, (1971) The applications of optical correlation techniques to the remote sensing of SO2 plumes using sky light, Atmos. Environ., 5, 677-690

Moore, J. G., & Sisson, T. W. (1981). Deposits and effects of the May 18 pyroclastic surge. US Geol. Surv. Prof. Pap, 1250, 421-438.

Nakada, S., & Fujii, T. (1993). Preliminary report on the activity at Unzen Volcano (Japan), November 1990-November 1991: Dacite lava domes and pyroclastic flows. Journal of Volcanology and Geothermal Research, 54(3), 319-333.

National Aeronautics and Spae Administration (NASA) Goddard Space Flight Center (2016, March, 30), Global Sulfur Dioxide Monitoring Home Page, http://so2.gsfc.nasa.gov/

Neal, C., Girina, O., Senyukov, S., Rybin, A., Osiensky, J., Izbekov, P., & Ferguson, G. (2009). Russian eruption warning systems for aviation. Natural hazards, 51(2), 245-262.

Newcomb, G. S., & MillÁn, M. M. (1970). Theory, applications, and results of the long-line correlation spectrometer. Geoscience Electronics, IEEE Transactions on, 8(3), 149-157

Olmos, R., Barrancos, J., Rivera, C., Barahona, F., López, D. L., Henriquez, B., ... & Galle, B. (2007). Anomalous emissions of SO2 during the recent eruption of Santa Ana volcano, El Salvador, Central America. Pure and Applied Geophysics, 164(12), 2489-2506

Oppenheimer, C. (1991). Lava flow cooling estimated from Landsat Thematic Mapper infrared data: the Lonquimay eruption (Chile, 1989). Journal of Geophysical Research: Solid Earth (1978–2012), 96(B13), 21865-21878.

Oppenheimer, C., Francis, P. W., Rothery, D. A., Carlton, R. W., & Glaze, L. S. (1993). Infrared image analysis of volcanic thermal features: Lascar Volcano, Chile, 1984–1992. Journal of Geophysical Research: Solid Earth (1978–2012), 98(B3), 4269-4286.

Ozerov, A., Ariskin, A., Kyle, P., Bogoyavlenskaya, G., Karpenko, S., 1997. Petrological- geochemical model for genetic relationships between basaltic and andesitic magmatism of Klyuchevskoi and Bezymiannyi Volcanoes, Kamchatka. Petrology 5 (6), 550–569.

Pahala Vog, (2016, March, 30), Preliminary SO2 data – Pahala – March 2008, http://kauscience.k12.hi.us/~ted/SO2/CAB_SO2_Pahala_March_2008.pdf

Patrick, M. R., Harris, A. J., Ripepe, M., Dehn, J., Rothery, D. A., & Calvari, S. (2007). Strombolian explosive styles and source conditions: insights from thermal (FLIR) video. Bulletin of volcanology, 69(7), 769-784.

Parfitt EA (2004) A discussion of the mechanisms of explosive basaltic eruptions. J Volcanol Geotherm Res 134:77–107

Parfitt EA, Wilson L (1995) Explosive volcanic eruptions—IX. The transition between Hawaiian-style lava fountaining and Strombolian explosive activity. Geophys J Int 121:226–232

Pergola, N., D'Angelo, G., Lisi, M., Marchese, F., Mazzeo, G., & Tramutoli, V. (2009). Time domain analysis of robust satellite techniques (RST) for near real-time monitoring of active volcanoes and thermal precursor identification. Physics and Chemistry of the Earth, Parts A/B/C, 34(6), 380-385.

Pergola, N., Marchese, F., & Tramutoli, V. (2004). Automated detection of thermal features of active volcanoes by means of infrared AVHRR records. Remote Sensing of Environment, 93(3), 311-327.

Pieri, D., & Abrams, M. (2004). ASTER watches the world's volcanoes: a new paradigm for volcanological observations from orbit. Journal of Volcanology and Geothermal Research, 135(1), 13-28.

Pieri, D., & Abrams, M. (2005). ASTER observations of thermal anomalies preceding the April 2003 eruption of Chikurachki volcano, Kurile Islands, Russia. Remote Sensing of Environment, 99(1), 84-94.

Ponomareva V.V.; Pevzner M.M.; Melekestsev, I.V. (1998) Large debris avalanches and associated eruptions in the Holocene eruptive history of Shiveluch volcano, Kamchatka, Russia. Bull. Volcanol. 59, 490–505.

Porter, J. N., Horton, K. A., Mouginis-Mark, P. J., Lienert, B., Sharma, S. K., Lau, E., ... & Oppenheimer, C. (2002). Sun photometer and lidar measurements of the plume from the Hawaii Kilauea Volcano Pu'u O'o vent: Aerosol flux and SO2 lifetime. Geophysical Research Letters, 29(16).

Portnyagin, M., Hoernle, K., Avdeiko, G., Hauff, F., Werner, R., Bindeman, I., ... & Garbe-Schönberg, D. (2005). Transition from arc to oceanic magmatism at the Kamchatka-Aleutian junction. Geology, 33(1), 25-28

Piña-Gauthier, M., Lara, L. E., Bataille, K., Tassara, A., & Báez, J. C. (2013). Co-eruptive deformation and dome growth during the 2008-2009 Chaitén eruption, Southern Andes. Andean Geology, 40(2), 310-323.

Pugnaghi, S., Gangale, G., Corradini, S., & Buongiorno, M. F. (2006). Mt. Etna sulfur dioxide flux monitoring using ASTER-TIR data and atmospheric observations. Journal of Volcanology and Geothermal Research, 152(1), 74-90.

Pugnaghi, S., Guerrieri, L., Corradini, S., Merucci, L., & Arvani, B. (2013). A new simplified approach for simultaneous retrieval of SO2 and ash content of tropospheric volcanic clouds: an application to the Mt Etna volcano. Atmospheric Measurement Techniques.

Ramsey, M.S. (2015). Synergistic use of satellite thermal detection and science: A decadal perspective using ASTER, Detecting, Modelling and Responding to Effusive Eruptions, in: Harris, A., De Groeve, T., Garel, F. and Carn, S. A. (eds.), Detecting, Modelling and Responding to Effusive Eruptions, Geol. Soc.,

Ramsey, M., & Dehn, J. (2004). Spaceborne observations of the 2000 Bezymianny, Kamchatka eruption: the integration of high-resolution ASTER data into near real-time monitoring using AVHRR. Journal of Volcanology and Geothermal Research, 135(1), 127-146.

Ramsey, M., Dehn, J., Wessels, R., Byrnes, J., Duda, K., Maldonado, L., & Dwyer, J. (2004). The ASTER emergency scheduling system: a new project linking near-real-time satellite monitoring of disasters to the acquisition of high-resolution remote sensing data. In AGU Fall Meeting Abstracts (Vol. 1, p. 0026).

Ramsey, M. S., & Fink, J. H. (1999). Estimating silicic lava vesicularity with thermal remote sensing: A new technique for volcanic mapping and monitoring. Bulletin of Volcanology, 61(1-2), 32-39.

Ramsey, M.S., Reath, K.A. and Williams, D.B. (2013). Threshold considerations for future volcanic hotspot and ash detection using HyspIRI, 2013 HyspIRI Science Workshop, Pasadena, CA.

Ramsey, M. S., Wessels, R. L., & Anderson, S. W. (2012). Surface textures and dynamics of the 2005 lava dome at Shiveluch volcano, Kamchatka. Geological Society of America Bulletin, 124(5-6), 678-689.

Realmuto, V.J., (1990). Separating the effects of temperature and emissivity: emissivity spectrum normalization. Proceedings of the 2nd TIMS Workshop, 2, pp. 31–35

Realmuto, V.J. (1994). Plume Tracker V.4.2.3 User Guide, California Institute of Technology

Realmuto, V. J., Abrams, M. J., Buongiorno, M. F., & Pieri, D. C. (1994). The use of multispectral thermal infrared image data to estimate the sulfur dioxide flux from volcanoes: a case study from Mount Etna, Sicily, July 29, 1986. Journal of Geophysical Research: Solid Earth (1978–2012), 99(B1), 481-488.

Realmuto, V. J., Sutton, A. J., & Elias, T. (1997). Multispectral thermal infrared mapping of sulfur dioxide plumes: A case study from the East Rift Zone of Kilauea Volcano, Hawaii. Journal of Geophysical Research: Solid Earth (1978–2012), 102(B7), 15057-15072.

Realmuto, V. J. (2000). The potential use of earth observing system data to monitor the passive emission of sulfur dioxide from volcanoes (pp. 101-115). American Geophysical Union.

Realmuto, V. J., & Watson, M. I. (2001, December). Advances in Thermal Infrared Mapping of Volcanic Sulfur Dioxide Plumes. In AGU Fall Meeting Abstracts (Vol. 1, p. 09).

Realmuto, V. J., Baxter, S., & Webley, P. W. (2011, December). Plume Tracker: A New Toolkit for the Mapping of Volcanic Plumes with Multispectral Thermal Infrared Remote Sensing. In AGU Fall Meeting Abstracts (Vol. 1, p. 04).

Realmuto, V. J., Berk, A., & Guiang, C. (2014, December). An Overview of Plume Tracker: Mapping Volcanic Emissions with Interactive Radiative Transfer Modeling. In AGU Fall Meeting Abstracts (Vol. 1, p. 3595).

Reath, K. A., & Ramsey, M. S. (2013). Exploration of geothermal systems using hyperspectral thermal infrared remote sensing. Journal of Volcanology and Geothermal Research, 265, 27-38.

Reath, K.A., Ramsey, M.S., Dehn, J., Webley, P.W. (Submitted). Predicting Eruptions from Precursory Activity using Remote Sensing Data Hybridization, Journal of Volcanism and Geothermal Research

Ripepe M, Marchetti E (2002) Array tracking of infrasonic sources at Stromboli volcano. Geophys Res Lett 29:2076

Ripepe M, Rossi M, Saccorotti G (1993) Image processing of explosive activity at Stromboli. J Volcanol Geotherm Res 54:335–351

Roberts, D. A., Quattrochi, D. A., Hulley, G. C., Hook, S. J., & Green, R. O. (2012). Synergies between VSWIR and TIR data for the urban environment: An evaluation of the potential for the Hyperspectral Infrared Imager (HyspIRI) Decadal Survey mission. Remote Sensing of Environment, 117, 83-101

Rodríguez-Elizarrarás, S., Siebe, C., Komorowski, J. C., Espíndola, J. M., & Saucedo, R. (1991). Field observations of pristine block-and ash-flow deposits emplaced April 16–17, 1991 at Volcan de Colima, Mexico. Journal of volcanology and geothermal research, 48(3), 399-412.

Rose, S., & Ramsey, M. (2009). The 2005 eruption of Kliuchevskoi volcano: Chronology and processes derived from ASTER spaceborne and field-based data. Journal of Volcanology and Geothermal Research, 184(3), 367-380.

Rose, S. R., Watson, I. M., Ramsey, M. S., & Hughes, C. G. (2014). Thermal deconvolution: Accurate retrieval of multispectral infrared emissivity from thermally-mixed volcanic surfaces. Remote Sensing of Environment, 140, 690-703.

Rothery, D. A., Francis, P. W., & Wood, C. A. (1988). Volcano monitoring using short wavelength infrared data from satellites. Journal of Geophysical Research: Solid Earth (1978–2012), 93(B7), 7993-8008.

Roy, D. P., Wulder, M. A., Loveland, T. R., Woodcock, C. E., Allen, R. G., Anderson, M. C., ... & Zhu, Z. (2014). Landsat-8: Science and product vision for terrestrial global change research. Remote Sensing of Environment, 145, 154-172.

Rybicki, G. B., & Lightman, A. P. (1979). Radiative processes in astrophysics. New York: Wiley-Interscience, pp. 25-26

Rybicki, G. B., & Lightman, A. P. (2008). Radiative processes in astrophysics. John Wiley & Sons.

Saucedo, R., Macías, J. L., & Bursik, M. (2004). Pyroclastic flow deposits of the 1991 eruption of Volcán de Colima, Mexico. Bulletin of Volcanology, 66(4), 291-306.

Schneider, D. J., Dean, K., Dehn, J., Miller, T., & Kirianov, V. Y. (2000). Monitoring and analyses of volcanic activity using remote sensing data at the Alaska Volcano Observatory: case study for Kamchatka, Russia, December 1997. Remote Sensing of Active Volcanism, 65-85.

Schneider, D. J., Vallance, J. W., Wessels, R. L., Logan, M., & Ramsey, M. S. (2008). Use of thermal infrared imaging for monitoring renewed dome growth at Mount St. Helens, 2004. A volcano rekindled, 2004-2006.

Schwarzkopf, L. M., Schmincke, H. U., & Cronin, S. J. (2005). A conceptual model for block-and-ash flow basal avalanche transport and deposition, based on deposit architecture of 1998 and 1994 Merapi flows. Journal of Volcanology and Geothermal Research, 139(1), 117-134.

SEAN Bulletin, (1994). Kliuchevskoi, v. 19, no. 9, p. 2–3.

Self, S., Sparks, R. S. J., Booth, B., & Walker, G. P. L. (1974). The 1973 Heimaey strombolian scoria deposit, Iceland. Geological Magazine, 111(06), 539-548.

Smithsonian Institute, Kliuchevskoi Volcano Eruptive History, Global Volcanism Program, 12/5/2013, http://www.volcano.si.edu/volcano.cfm?vn=300270

Sparks, R. S. J. (2003). Forecasting volcanic eruptions. Earth and Planetary Science Letters, 210(1), 1-15.

Sparks, R. S. J., Wilson, L., & Hulme, G. (1978). Theoretical modeling of the generation, movement, and emplacement of pyroclastic flows by column collapse. Journal of Geophysical Research: Solid Earth (1978–2012), 83(B4), 1727-1739.

Sparks, R. S. J., & Young, S. R. (2002). The eruption of Soufrière Hills volcano, Montserrat (1995-1999): overview of scientific results. Geological Society, London, Memoirs, 21(1), 45-69.

Sobolevskaya, O. V., & Senyukov, S. L. (2008). RETROSPECTIVE ANALYSIS OF THE THERMAL ANOMALY TEMPERATURE CHANGE AT BEZYMIANNY VOLCANO 2002-2007, AS A PRECURSOR OF IT 'S ERUPTIONS, BY AVHRR NOAA 16 AND 17 SATELLITE DATA. Bulletin of Kamchatka Regional Association 'Educational-Scientific Center'. Earth Sciences, 11, 147-157.

Stevens, N. F., Garbeil, H., & Mouginis-Mark, P. J. (2004). NASA EOS Terra ASTER: Volcanic topographic mapping and capability. Remote Sensing of Environment, 90(3), 405-414.

Symonds, R. B., Gerlach, T. M., & Reed, M. H. (2001). Magmatic gas scrubbing: implications for volcano monitoring. Journal of Volcanology and Geothermal Research, 108(1), 303-341.

Symonds, R. B., W. I. Rose, G. J. S. Bluth, and T. M. Gerlach, (1994) Volcanic gas studies—Methods, results, and applications, in Volatiles in Magmas, Rev. Mineral., vol. 30, pp. 1–66

Sutton, A.J., McGee, K.A., Casadevall, T.J., Stokes, J.B. (1993) Fundamental Volcanic Gas Study Techniques: An Integrated Approach to Monitoring: Monitoring Volcanoes: Techniques and Strategies Used by the Staff of the Cascades Volcano Observatory, 1980–1990. USGS Bulletin No. 1966, p. 181

Sweeney, D., Kyle, P. R., & Oppenheimer, C. (2008). Sulfur dioxide emissions and degassing behavior of Erebus volcano, Antarctica. Journal of Volcanology and Geothermal Research, 177(3), 725-733.

Theys, N., Campion, R., Clarisse, L., Brenot, H., Van Gent, J., Dils, B., ... & Ferrucci, F. (2013). Volcanic SO2 fluxes derived from satellite data: a survey using OMI, GOME-2, IASI and MODIS. Atmos. Chem. Phys, 13(12), 5945-5968.

Thome, K., Arai, K., Hook, S., Kieffer, H., Lang, H., Matsunaga, T., ... & Takashima, T. (1998a). ASTER preflight and inflight calibration and the validation of level 2 products. Geoscience and Remote Sensing, IEEE Transactions on, 36(4), 1161-1172.

Thome, K., Palluconi, F., Takashima, T., & Masuda, K. (1998b). Atmospheric correction of ASTER. Geoscience and Remote Sensing, IEEE Transactions on, 36(4), 1199-1211.

Tilling, R. I. (1989). Volcanic hazards and their mitigation: progress and problems. Reviews of Geophysics, 27(2), 237-269.

Todesco, M., Neri, A., Ongaro, T. E., Papale, P., Macedonio, G., Santacroce, R., & Longo, A. (2002). Pyroclastic flow hazard assessment at Vesuvius (Italy) by using numerical modeling. I. Large-scale dynamics. *Bulletin of volcanology*,*64*(3-4), 155-177.

Urai, M. (2002, February). Sulfur dioxide flux estimation at Oyama volcano in Miyake-Jima, Japan, using advanced spaceborne thermal emission and reflection radiometer (ASTER). In International Symposium on Optical Science and Technology (pp. 14-19). International Society for Optics and Photonics.

van Manen, S. M., & Dehn, J. (2009). Satellite remote sensing of thermal activity at Bezymianny and Kliuchevskoi from 1993 to 1998. Geology, 37(11), 983-986.

van Manen, S. M., Dehn, J., & Blake, S. (2010). Satellite thermal observations of the Bezymianny lava dome 1993–2008: precursory activity, large explosions, and dome growth. Journal of Geophysical Research: Solid Earth (1978–2012), 115(B8).

van Manen, S. M., Blake, S., Dehn, J., & Valcic, L. (2013). Forecasting large explosions at Bezymianny Volcano using thermal satellite data. Geological Society, London, Special Publications, 380(1), 187-201.

Vaughan, R. G., Hook, S. J., Ramsey, M. S., Realmuto, V. J., & Schneider, D. J. (2005). Monitoring eruptive activity at Mount St. Helens with TIR image data. Geophysical Research Letters, 32(19).

Vergniolle S, Brandeis G (1996) Strombolian explosions. 1. A large bubble breaking at the surface of a lava column as a source of sound. J Geophys Res 101:20433–20447

Voight, B., & Davis, M. J. (2000). Emplacement temperatures of the November 22, 1994 nuée ardente deposits, Merapi Volcano, Java. Journal of Volcanology and Geothermal Research, 100(1), 371-377.

Voight, B., & Sousa, J. (1994). Lessons from Ontake-san: a comparative analysis of debris avalanche dynamics. Engineering Geology, 38(3), 261-297.

Waples, D. W., & Waples, J. S. (2004). A review and evaluation of specific heat capacities of rocks, minerals, and subsurface fluids. Part 1: Minerals and nonporous rocks. Natural resources research, 13(2), 97-122.

Watson, I. M., Realmuto, V. J., Rose, W. I., Prata, A. J., Bluth, G. J. S., Gu, Y., ... & Yu, T. (2004). Thermal infrared remote sensing of volcanic emissions using the moderate resolution imaging spectroradiometer. Journal of volcanology and geothermal research, 135(1), 75-89.

Werner, C. A., Doukas, M. P., & Kelly, P. J. (2011). Gas emissions from failed and actual eruptions from Cook Inlet Volcanoes, Alaska, 1989–2006. Bulletin of Volcanology, 73(2), 155-173.

Werner, C., Kelly, P. J., Doukas, M., Lopez, T., Pfeffer, M., McGimsey, R., & Neal, C. (2013). Degassing of CO 2, SO 2, and H 2 S associated with the 2009 eruption of Redoubt Volcano, Alaska. Journal of Volcanology and Geothermal Research, 259, 270-284.

Wilson, D., Elias, T., Orr, T., Patrick, M., Sutton, J., & Swanson, D. (2008). Small explosion from new vent at Kilauea's summit. EOS, Transactions American Geophysical Union, 89(22), 203-203.

Worden, A., Dehn, J., & Webley, P. (2014). Frequency based satellite monitoring of small scale explosive activity at remote North Pacific volcanoes. Journal of Volcanology and Geothermal Research, 286, 1-14

Wright, R., Flynn, L. P., Garbeil, H., Harris, A. J., & Pilger, E. (2004). MODVOLC: near-real-time thermal monitoring of global volcanism. Journal of Volcanology and Geothermal Research, 135(1), 29-49.

Wright, R., Rothery, D. A., Blake, S., & Pieri, D. C. (2000). Improved remote sensing estimates of lava flow cooling: a case study of the 1991–1993 Mount Etna eruption. Journal of Geophysical Research: Solid Earth (1978–2012), 105(B10), 23681-23694.

Wohletz, K., & Heiken, G. (1992). Volcanology and geothermal energy (p. 432). Berkeley^ eCalifornia California: University of California Press.

Yamaguchi, Y., Kahle, A. B., Tsu, H., Kawakami, T., & Pniel, M. (1998). Overview of advanced spaceborne thermal emission and reflection radiometer (ASTER). *Geoscience and Remote Sensing, IEEE Transactions on*, *36*(4), 1062-1071.

Yogodzinski, G. M., Lees, J. M., Churikova, T. G., Dorendorf, F., Wöerner, G., & Volynets, O. N. (2001). Geochemical evidence for the melting of subducting oceanic lithosphere at plate edges. Nature, 409(6819), 500-504.

Young, S. R., Francis, P. W., Barclay, J., Casadevall, T. J., Gardner, C. A., Darroux, B., ... & Watson, I. M. (1998). Monitoring SO2 emission at the Soufriere Hills volcano: implications for changes in eruptive conditions. Geophysical Research Letters, 25(19), 3681-3684.

Zharinov, N. A., & Demyanchuk, Y. V. (2008). The growth of an extrusive dome on Shiveluch Volcano, Kamchatka in 1980–2007: geodetic observations and video surveys. Journal of Volcanology and Seismology, 2(4), 217-227.